Emil Barić, mag. ing. mech.

Computational flow analysis for optimization of wire coating dies

DOCTORAL THESIS

to achieve the university degree of

Doktor der technischen Wissenschaften

submitted to

Graz University of Technology

Supervisor

Ao. Univ.-Prof. Dipl.-Ing. Dr. techn. Helfried Steiner

Institute of Fluid Mechanics and Heat Transfer

Graz, February 2016.

Deutsche Fassung:
Beschluss der Curricula-Kommission für Bachelor-, Master- und Diplomstudien vom 10.11.2008
Genehmigung des Senates am 1.12.2008

EIDESSTATTLICHE ERKLÄRUNG

Ich erkläre an Eides statt, dass ich die vorliegende Arbeit selbstständig verfasst, andere als die angegebenen Quellen/Hilfsmittel nicht benutzt, und die den benutzten Quellen wörtlich und inhaltlich entnommenen Stellen als solche kenntlich gemacht habe.

Graz, am..... .....
(Unterschrift)

Englische Fassung:

STATUTORY DECLARATION

I declare that I have authored this thesis independently, that I have not used other than the declared sources / resources, and that I have explicitly marked all material which has been quoted either literally or by content from the used sources.

…… ……
(date) (signature)

ACKNOWLEDGEMENTS

The present work on the computational flow analysis inside wire coating dies was conducted between February 2012 and December 2015 at the Institute of Fluid Mechanics and Heat Transfer at Graz University of Technology. Part of the research was funded by the Österreichische Forschungsförderungsgesellschaft mbh in the frame of the project No. 833754, and the industrial partner MAG Maschinen und Apparatebau AG.

I would like to express my deepest graditude to the supervisor of my work Ao. Univ.-Prof. Dipl.-Ing. Dr. techn. Helfried Steiner who enriched this research work with his extensive knowledge, ideas and suggestions, and was always available for help and discussions.

I would also like to thank the head of the Institute of Fluid Mechanics and Heat Transfer Univ.-Prof. Dr.-Ing. habil. Günter Brenn for the contribution to the work through his professional knowledge and continuous support.

Special thanks I would like to address to the head of the Research and Development department of the company MAG Maschinen und Apparatebau AG Dr. techn. Klaus Czaputa for his contribution to many discussions regarding the present work, and especially for the contribution in designing the required measuring device and supervising the conducted measurements.

I would also like to thank Ao. Univ.-Prof. Dipl.-Ing. Dr. techn. Herbert Steinrück for his reviews and comments which helped to elevate the quality of the work.

Furthermore, I would like to thank all of the members of the Institute of Fluid Mechanics and Heat Transfer for many fruitful discussions and for providing great working environment.

Finally, I would like to express my gratitude to all members of my family for their continuous support and encouragement throughout my studies, especially to my grandfather who guided me to choose mechanical engineering as a future career.

ABSTRACT

Coating of technical surfaces represents an important production step in many industrial applications for realizing certain surface properties. The coating process has in general to ensure continuous, complete, and high quality coverage of the surface with a defined layer of liquid finally providing the desired mechanical, chemical, or electrical properties. The present work computationally investigates in particular the generalized Couette flow evolving inside converging enameling dies which are typically used for the coating of magnet wires with electrical insulation. For this purpose an analytical computational model based on the lubrication theory approximation was developed accounting for non-Newtonian behavior of the working fluid, and including heat transfer as well. Due to the lack of experimental data available on the considered narrow gaps flow configuration the predictions of the developed model were validated against CFD results from numerical simulations showing in general very good agreement. In regions with a strong axial change in cross-section some deviations appeared in the predicted velocity fields, and more significantly in the predicted temperature fields for higher Prandtl numbers. These deficits essentially resulting from the neglect of advective transport in the lubrication theory approximation could be largely reduced for the Newtonian fluid case by introducing a first-order extension of the model accounting for the advective transfer of momentum and heat. The proposed first-order extension of the zeroth-order base model representing the lubrication theory approximation was proven to give markedly improved predictions for the local variations of velocity and temperature, which also translates into a very accurate description of the global balances of momentum and heat. Having to rely not solely on CFD data for validation a special measuring device was built by the industrial partner to measure the total drag force exerted on the wire when pulled through the die under real operating conditions. The measured data were in good agreement with the results obtained from the analytical zeroth-order model for the considered non-Newtonian enamel. The computational as well as experimental results made evident that the total drag forces are not sufficiently high to cause any large scale plastic deformation or breakage of the wire. The observed mechanical stresses may still trigger some undesired microstructural changes of the wire material, making it unusable for winding. Based on the computed flow fields the local variation of shear stress on the wire was analyzed to derive possible modifications of existing real die geometries as well as

variants of generic die shapes with an analytically prescribed cosine-type contraction, which finally lead to a notable reduction in drag force. This analysis helped to identify the geometrical key features of the die contour, which most effectively reduce the resulting total drag force. These findings obtained in the first place for the generic analytically prescribed die shapes were used to propose technically realizable geometrical modifications of real enameling dies. Producing markedly lower total drag forces the proposed novel die designs are well suited especially in the light of ongoing and future trends towards the application of more viscous enamels and higher production speeds leading both to strongly increased shear forces. A reliable computational description as provided by the present analytical model is a prerequisite for any further flow related optimization of the die shape expectedly needed to cope with these trends.

TABLE OF CONTENTS

LIST OF FIGURES

LIST OF TABLES

LIST OF SYMBOLS

Symbol	Description	Unit
A	Vogel model parameter	Pas
A_{wire}	cross-sectional area of the wire	mm^2
B	Vogel model parameter	K
C	Vogel model parameter	K
$\underline{D}$	Deformation rate tensor	1/s
$\underline{E}$	Unity tensor	-
c_p	specific heat capacity	J/kgK
d_w	diameter of the wire	m
F_d	drag force	N
h	deposition height	m
h_e	die exit gap height	m
H	total heat flow through die inlet/outlet	W
K_1	Carreau-Yasuda model parameter	s
L	axial length of the die	m
M	torque	Nm
$m_{1/2}$	Carreau-Yasuda model parameter	-
m	power law fluid model parameter	-
n	iteration step	-
n	power law fluid model exponent	-
n_{geo}	geometry parameter	-
P_η	produced viscous heat	W
p	pressure	Pa
Δp	pressure drop	Pa
Q	total heat flux	W
q_w	wall heat flux	W/m^2

r	radial coordinate (cylindrical)	m
r_w	radius of the wire	m
r_d	contour of the die	m
T	thermodynamic temperature	K
T_w	wire temperature	K
U_w	velocity of the wire	m/s
$\dot{V}$	volumetric flow rate	m^3/s
u	axial velocity component	m/s
x	axial coordinate (Cartesian)	m
y	radial coordinate (Cartesian)	m
v	radial velocity component	m/s
z	axial coordinate (cylindrical)	m
I_D	1^{st} invariant of deformation rate tensor	1/s
II_D	2^{nd} invariant of deformation rate tensor	$(1/s)^2$
III_D	3^{rd} invariant of deformation rate tensor	$(1/s)^3$
∇	vector differential operator	1/m

Greek symbols

Symbol	Description	Unit
α	angle of the die	°
$\dot{\gamma}$	shear rate	1/s
δ	difference in gap height between die inlet and outlet	m
ε	series expansion parameter (mom.)	-
ε_T	series expansion parameter (temp.)	-
Φ_{visc}	viscous heating source term	W/m^3

φ_0	Reiner-Rivlin fluid coefficient	Pa
φ_1	Reiner-Rivlin fluid coefficient	Pas
φ_2	Reiner-Rivlin fluid coefficient	$Pa(s)^2$
η	dynamic viscosity	Pas
Λ	relaxation time scale	s
λ	thermal conductivity	W/mK
ρ	density	kg/m^3
θ	angular coordinate	°
τ	viscous stress	N/m^2
$\underline{\tau}$	stress tensor	N/m^2

Dimensionless numbers

Symbol	Description
Ca	Capillary number
Ec	Eckert number
Pe	Pèclet number
Pr	Prandtl number
Re	Reynolds number
$\widetilde{\mathrm{Re}}$	reduced Reynolds number

Superscripts

Symbol	Description
*	dimensionless quantity
$\overrightarrow{(\ )}$	vector

Subscripts

Symbol	Description
0	zeroth order solution
1	first order solution
I	first Newtonian plateau
II	second Newtonian plateau
d	die
rz	shear stress component
w	wire

1. INTRODUCTION

1.1 Background and Motivation

Coating can be basically defined as the covering of the surface of some solid substrate with a layer of an adhering liquid. The main reason for applying such a surface coating can vary dependent of the application of the final product. It can range from purely decorative to purely functional, or the combination of both. Different types (techniques) of coating can result in a different coverage of the substrate which, regarding the covered area, can vary from partial coverage to full coverage of the substrate. The coating can be applied to a substrate using a variety of techniques. Most common processes can be divided into: chemical, mechanical, thermal and thermo-mechanical.

Functional coatings play a dominant role in the industrial application. They are applied in order to change the surface properties of the substrate making it more suitable for a specific application. The targeted properties of the substrate can be various, affecting adhesion, thermal, mechanical, or, chemical resistance, surface wetability, surface roughness etc. Since the thickness of the coating is often an important parameter, different techniques have been developed to obtain the desired coating thickness. These methods range from simple paint brushing layer per layer until a certain thickness is obtained, to fairly complex liquid deposition techniques applied in the production of components for electrical industry.

One representative example of a complex multi-step coating process is met in the production of enameled or magnet wire. Enameled wire in general represents a copper or aluminum wire covered with a thin layer of electrical insulation (see Figure 1). This type of wire is most commonly used in applications, where tight coils are required, such as the coil of stator and rotor of an electric motor, or the coil applied inside an electric transformer. A sufficient electrical insulation against shorts is in general a prerequisite for safe and reliable operation of these devices. For that reason wires are covered with multiple layers of coating ensuring a uniform continuous insulation. Especially, in high-voltage devices any imperfection in the coating would

most likely lead to strong spurious currents, which may finally result in a burn down of the whole device.

Different polymer solutions are generally used as enameling liquids. The type of polymer mostly depends on the technical application of the wire, ranging from polyurethane for less critical applications, where wires are subjected to low electrical loads, to combinations of polyester and polyamide for the more heavy duty applications.

Figure 1: Raw wire and enameled copper wire (source MAG)

The production process of enameled or magnet wire is carried out on special wire enameling machines. These machines usually involve multiple production steps which have to ensure a correct wire diameter and satisfactory quality of the surface of the end product. They can be designed as vertical and horizontal machines, but, regardless of the type, the principle of the process and the main components of the machine are essentially the same. The main components of both types of machines are shown in Figure 2.

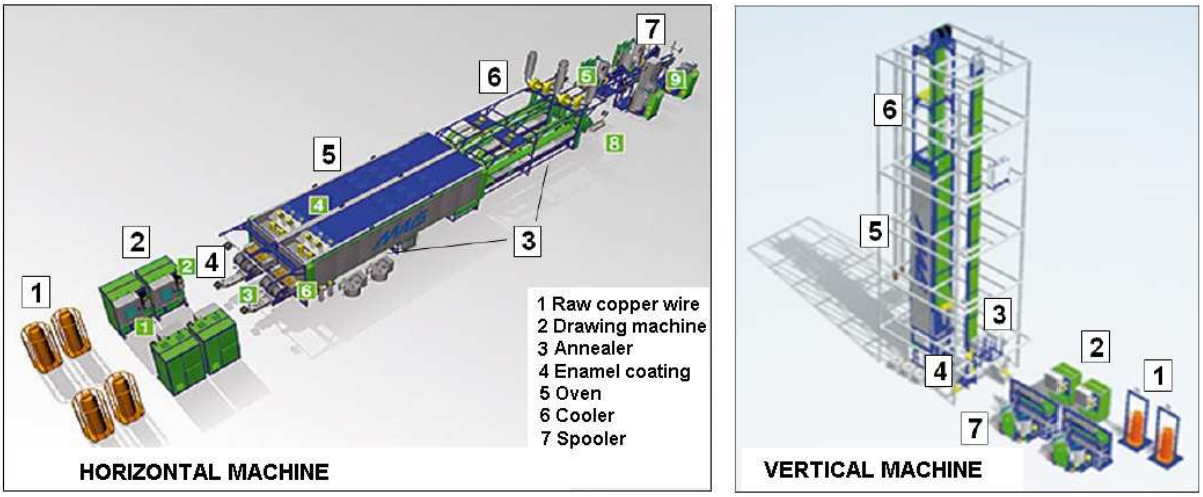

Figure 2: Main components of the wire enameling machines (source MAG)

Raw copper wire supplied at the entry of the device usually has a wire diameter that is a little bit higher than the desired diameter of the blank wire to be coated with enamel. It is therefore necessary to pull the wire first through a drawing machine to provide the correct diameter before entering the enameling process. Inside the drawing machine the wire is passed through multiple drawing dies, successively reducing the diameter. The high stresses imposed during the drawing process cause a hardening of the copper wire. In order to regain those material properties required for the further production, such as ductility, the wire is passed through an annealing zone, where the material is heated up to a certain annealing temperature and cooled down again to ambient temperature. In the next step the blank wire enters the enameling process, where its surface is successively coated with a certain layer of fresh liquid enamel. After each deposition of fresh enamel, the wire passes an oven, where the solvent evaporates, and the remaining solid polymer content is cured. Usually, temperatures inside the oven reach up to 700 °C. Such high temperatures are required due to the relatively short dwell time of the wire inside the oven, especially in the case of smaller wire diameters, to ensure a complete evaporation of the solvent and curing of the polymer. After each pass through the oven, the wire is cooled in a cross stream of air. A detailed study and optimization of the drying and curing process inside the oven was carried out by Czaputa 2009. Finally, the wire is directed to the spooler, where it is wound up

into large coils, appropriate for transport and storage. Some details of each component shown in Figure 2 can be seen in Figure 3.

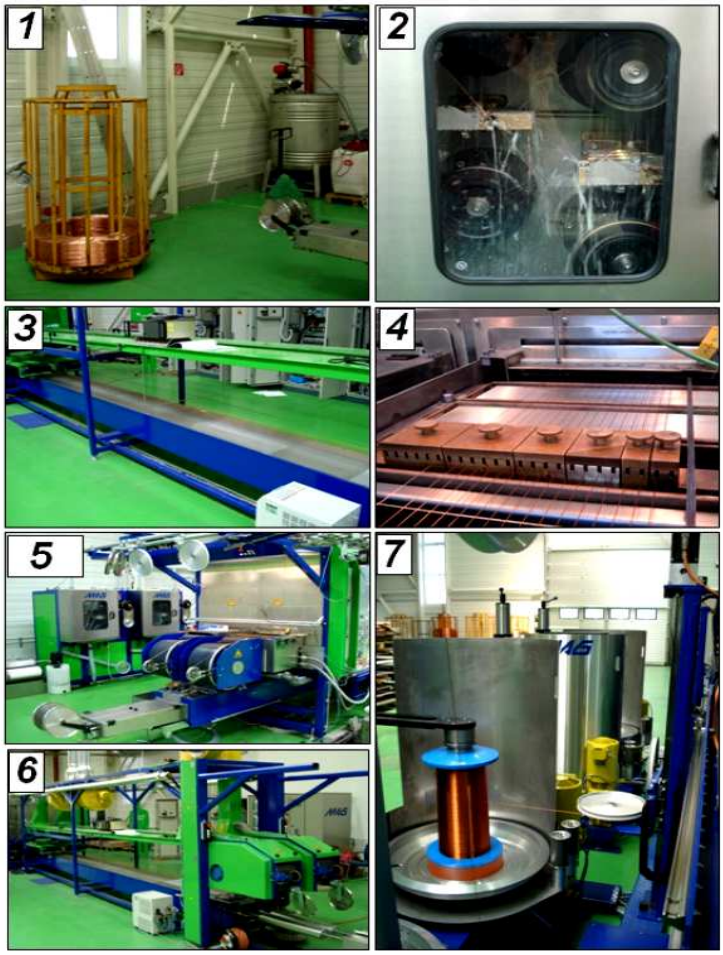

Figure 3: Details of enameling machine components (source MAG)

The focus of the present work is on the liquid enamel deposition step, where a defined layer of fresh enamel is deposited on the surface of the moving wire. The principle of this liquid coating process is shown in Figure 4. The process essentially involves two main steps. In the first step an initial layer of enamel is deposited on the wire based on the principle of dip coating, where the wire is pulled through a small bath of enamel which is fed from a bigger reservoir beneath. In the

second step the basically undefined thickness of the dip coating is reduced to the desired level by pulling the wire through an enameling die. Due to the converging geometry of the annular gap between the wire and the die contour the excess enamel is stripped off the surface, so that the wire exits the die with a defined deposition height of fresh enamel (see Figure 4 rhs). The excess enamel is ejected upstream at the inlet of the die. It is then passed through a filter and re-enters the enamel reservoir to be applied again for the coating process. The whole coating is applied in multiple deposition cycles, adding one further layer on top of the other until the final height is reached. Within each deposition cycle the deposited fresh enamel is dried and cured in the oven. Usually, the number of passes applied in the process varies between 10 and 25 depending on the wire thickness, required wire properties, type of enamel, etc.

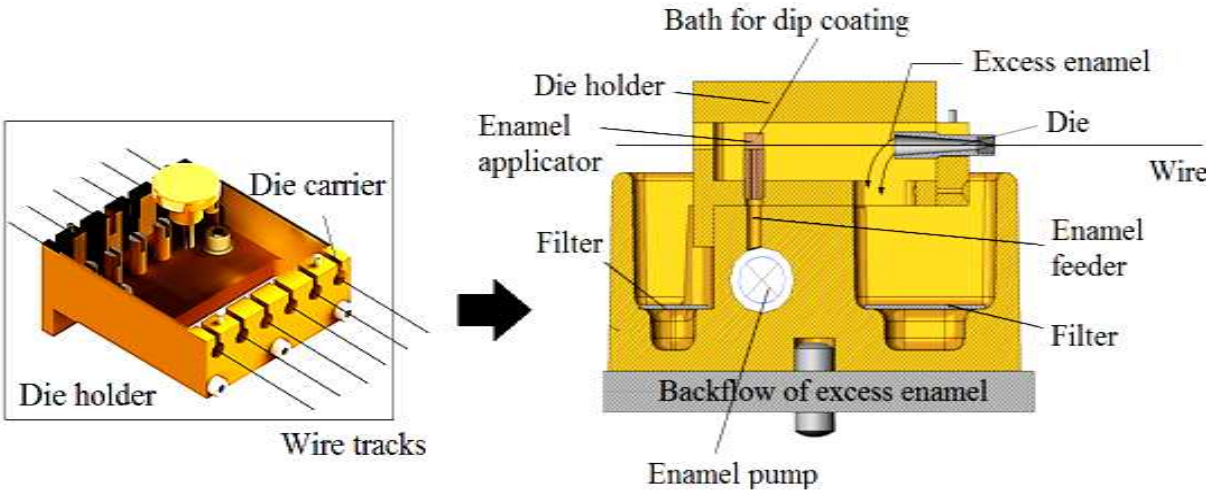

Figure 4: Principle of enamel application on the wire surface (source MAG)

1.2 Literature survey

The description of the flow evolving inside narrow gaps, or gaps with converging geometry, considering different rheological behavior of fluids is of high relevance in many different applications. Therefore, a significant number of studies related to this topic are available in the literature. The investigated flow evolving inside these narrow gap geometries is often Couette or generalized Couette flow, depending on the geometrical outline-contour.

The generalized Couette flow between two infinite parallel plates subject to a pressure gradient was studied in the work of Flumerfelt at al. 1969. Matsuhisa and Bird 1965 provided analytical and numerical solutions for a large variety of configurations including the flow between flat plates, in tubes, in films, and annuli, assuming a non-Newtonian Ellis fluid.

Couette type gap flow configurations are also met inside the bore holes in ground drilling applications, or inside journal bearings. A computational analysis of such a generalized Couette flow inside an annulus, where the flow is driven by the motion of the inner cylinder and additionally subjected to a pressure gradient, was presented by Lin and Hsu 1980. In follow-up studies Lin and Hsieh 1980, and Lin 1992 included heat transfer into their computations. Young and Chukwu 1995 analytically computed generalized Couette flow of a power-law fluid in a narrow eccentric annulus in order to investigate the effect of the eccentricity of the inner moving cylinder on the axial pressure gradient. Fitt and Please 2000 described an isothermal flow of a shear thinning fluid inside an annulus between the two concentric cylinders, where the inner one was set into a rotating motion, using an asymptotic analysis and comparing it to CFD results. Nessil et al. 2013 analyzed the lubrication of a non-Newtonian power-law fluid inside a journal bearing including heat transfer. A recent work describing axial flow of a non-Newtonian fluid in a concentric annulus using generalized flow parameters which enable implementation of different non-Newtonian flow models was presented by Haobo et al. 2014. Sheeja and Prabhu 1992 investigated the flow evolving in the annular gap of a journal bearing using both a computational and experimental approach, to study the performance characteristics of the bearing. Considering a more complex surface involving shallow dimples, a CFD based analysis of the lubrication behavior of a journal bearing was presented by Yong and Balendra 2009. He

2004 applied the variational principle to derive the Reynolds equations for describing the flow of a Rabinowitsch-type non-Newtonian fluid inside a planar slider bearing.

Apart from the technical application, the narrow gap flow of non-Newtonian fluids is also of high relevance in other fields such as biomedical flows, where the emphasis is put on analyzing the flow inside the cardiovascular system. In 1972 Oka investigated the evolution of the pressure along the axis of a tapered tube with fixed walls, using different types of non-Newtonian fluids. Based on the work on Oka a more recent study on the flow inside tapered pipes, considering different angles as well as different rheological models in order to obtain flow rate and pressure profiles was conducted by Kumar and Kumar 2003. The unsteady flow inside a tapered tube of a non-Newtonian fluid inside arteries with a stenosis was computationally analyzed by Mandal in 2004.

Hull and Pearson 1984 investigated the non-Couette type flow of non-Newtonian viscoelastic fluids through cones and wedges with stationary walls, which is of high relevance for the polymer processing technology.

The basic concepts for the computational analysis of the generalized Couette-type flow and heat transfer in converging gaps, specifically met in enameling dies can be found in the review of Mitsoulis 1986. Carley et al. 1979 computed the flow and temperature field inside the conical section of wire coating dies by solving numerically the simplified conservation equations with a semi-implicit finite-difference scheme. Tadmor and Bird 1974 investigated the magnitudes of the lateral forces which the fluid exerts on a wire eccentrically positioned inside the coating die, and their effect on the stability of the wire during the coating process.

Dijksman and Savenije 1985 presented an analytical solution of the converging flow through coating dies applying the lubrication approximation theory. They introduced a special toroidal coordinate system, which suitably fits to their considered conical geometry of the die, but admits only straight lines as outer radial contour of the die. In a recent work Shah et al. 2013 presented analytical solutions for Couette flow with zero pressure gradient assuming power-law fluids, ranging from strongly shear thinning to strongly shear thickening, imposing linearly varying wall temperatures.

Most of the computational studies performed on the narrow gap flow problem assume the approximation of the lubrication theory, which essentially neglects all advective transport. Appropriate extensions to the lubrication theory in order to account for the effect of advective transport have thus far been proposed only for narrow gap flow configurations different from the ones met in the wire coating process, like flow in planar journal bearings considered by Collins et al. 1986, or pressure-driven flow through narrow planar channels with axially varying channel height studied by Tavakol et al. 2014.

1.3 Objectives

Due to the extremely high shear rates occurring inside the converging gaps of the coating dies very high shear forces act on the surface of the moving wire resulting in large total drag forces exerted on the wire. The pressing need for drag force reduction mainly comes from some particular characteristics of the wire enameling process, which have in common that they all potentially strongly increase the shear forces. First, the solid mass fraction in the applied enamel should be very high to reduce the costs for the solvent, and to deposit a highest possible amount of solid coating mass per wire pass through the die. Secondly, the solid content should be mainly constituted by large polymers. Large polymers tend to be less volatile, so that the solid losses into the hot gaseous ambiance during the drying and curing of the deposited fresh layer can be kept low. Meeting both requirements implies more viscous enamels, which translates directly into an increase in the drag force on the wire drawn through the coating dies. Thirdly, the maximum allowable heat up of the wire, which occurs in the oven for the drying and curing of the coating, limits the residence time of the wire in the oven. Since the thinner wires inherently heat up faster they permit a shorter residence time in the oven to avoid overheating of the material, which implies a faster wire speed. In combination with the typically smaller die exit gap heights, this finally leads to much higher shear rates and shear stresses, and hence larger drag forces, particularly for the thin wires. Apart from these process-related aspects, the permanent economic demand for higher productivity and cost reduction keeps pushing for increased wire

velocities, which further fosters the need for most appropriate die shapes to keep the total drag forces within an acceptable range.

The main objective of the work is to computationally investigate the flow field inside wire enameling dies, which shall finally also help to identify the possible flow related reasons for the wire breakages appearing during production, as reported by the magnet wire producers, especially in the case of thin wires (for diameters ranging from 0.15 mm to 0.35 mm). The description of the flow field shall be obtained from a suitable computational model to be developed. The developed model shall provide an accurate prediction of the flow and temperature fields at low computational costs. It shall flexibly handle different die geometries as well as different fluid properties, so that it finally also serves as a computationally efficient and reliable tool for developing flow optimized die geometries.

1.4 Approach

The developed computational model for describing the momentum and heat transfer inside the wire enameling dies basically relies on the analytical approach assuming the lubrication theory approximation. For the case of Newtonian fluids the lubrication theory approximation is extended by a first-order perturbation to include the effect of inertia and convective heat transfer. The very confined geometry of the flow domain basically excludes any detailed measurements of the flow and temperature fields using today's available measurement techniques. Due to this lack of experimental data, a numerical model was used to provide data for a validation of the predictions obtained from the developed analytical model. Solving the full set of equations in a discretized formulation inherently makes the numerical simulations computationally more expensive than the analytical model. The numerical simulations are performed using the commercial CFD code Ansys FLUENT. Some experimental validation could be still carried out for the analytically predicted drag forces on the wire. The required experimental data were obtained using a drag force measuring device, which was specially designed and constructed by the industrial partner MAG. The drag force measurements were carried out on an enameling machine running under real production conditions.

1.5 Organization of the Thesis

Chapter 2 deals with the possible flow properties of the working fluid, discussing established models for describing the flow behavior of Newtonian and non-Newtonian fluids. It further surveys the coating liquids typically applied in the wire enameling process. The main measuring techniques for determining the dynamic viscosity of these liquids are described as well, including the measured flow curves for some representative enamels.

Chapter 3 describes the derivation of the analytical computational model using the assumptions of the lubrication theory, applying it first to a Newtonian fluid and then the non-Newtonian fluids. The extension of the analytical model to the heat transfer is also described. The results obtained from the analytical model for generic converging die geometries are discussed and validated against CFD results. For the case of Newtonian fluids, the analytical model is extended introducing the first-order perturbation to improve the accuracy of the analytical predictions.

Chapter 4 describes the application of the developed analytical computational model for describing the flow field inside real die geometries under real operating conditions. The results obtained by the analytical model for the hydrodynamic drag forces exerted on the wire are further validated against data from a specially designed measuring device. Possible reasons for frequently reported problems during the production process, such as breakage and plastic deformation of the wire, are discussed.

Chapter 5 deals with the application of the developed computational model to provide modified real die geometries, which generate significantly reduced drag forces exerted on the wire. Using such flow optimized geometries shall ensure a save and continuous production process and allow for further increase in productivity and reduction in process costs.

Chapter 6 gives a summary and the main conclusions coming from the presented computations and analysis of the results.

2. RHEOLOGY OF THE WORKING FLUID

Fluids exhibit different properties depending on their chemical composition, structure and size of the fluid molecules, etc. For any fluid type the most general form of momentum equation, neglecting body forces, reads

$$\rho \frac{D\vec{v}}{Dt} = -\nabla p + \nabla \cdot \underline{\tau}. \tag{1}$$

In order to provide closure for the system it is necessary to define the dependence of the stress tensor on the deformation rate tensor, $\underline{\tau} = \underline{\tau}(\underline{D})$, where the deformation rate tensor $\underline{D}$ is written as

$$\underline{D} = \frac{1}{2}\left[(\nabla \vec{v}) + (\nabla \vec{v})^T \right]. \tag{2}$$

In the most general case the shear stress depends on the history of this tensor. The particular dependency for the considered fluid is essentially determined by its microscopic structure. A highly complex molecular structure in general translates into a more complex relation between shear stress and deformation rate. Figure 5 exemplarily shows some modifications of the internal structure of the suspensions, containing larger particles or molecules, when subjected to deformation.

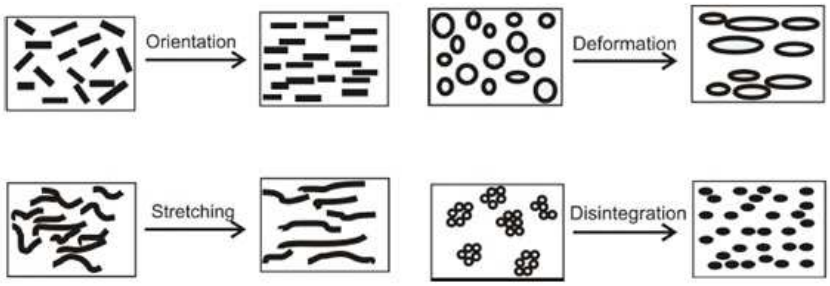

Figure 5: Behavior of suspensions subjected to deformation (adopted from Chhabra, 2010)

2.1 Purely viscous fluids

If the stress depends only on the instantaneous deformation rate tensor $\underline{D}$ and the material behaves isotropic, the fluid is termed a purely viscous or Reiner-Rivlin fluid. As stated in the book of Giesekus on phenomenological rheology 1994, the relation between the stress tensor and the instantaneous deformation rate tensor can be described by the following algebraic constitutive equation:

$$\underline{\tau} = \varphi_0 \underline{E} + \varphi_1 \underline{D} + \varphi_2 \underline{D}^2. \tag{3}$$

Therein, $\underline{E}$ is the unity tensor and the coefficients φ_i depend on the density and three invariants of the deformation rate tensor:

$$\varphi_i = \varphi_i \left(\rho; I_D, II_D, III_D \right), \qquad i = 0, 1, 2, \tag{4}$$

with

$$\varphi_0 \left(\rho; 0, 0, 0 \right) = 0. \tag{5}$$

Liquids of practical relevance considered in this work are incompressible, implying that their density ρ does not vary, such that the coefficient φ_0 can be set to zero. Moreover, the other coefficients are independent ρ of and I_D, due to $I_D = \nabla \cdot \vec{v} = 0$, and hence, Eq. (3) can be rewritten as

$$\underline{\tau} = \varphi_1 \left(II_D, III_D \right) \underline{D} + \varphi_2 \left(II_D, III_D \right) \underline{D}^2 . \tag{6}$$

The coefficients φ_1 and φ_2 can be generally rewritten as $\varphi_1 = 2\eta$ and $\varphi_2 = 4\xi$, where η denotes the apparent shear viscosity and ξ denotes the so called cross-viscosity. The ratio between the two coefficients φ_2 and φ_1 has the unit of time, which can be interpreted as a material specific time scale. This is, however not consistent with the constitutive algebraic Eq. (6), which does not involve any dependence on time. Discussing this inconsistency Giesekus 1994 stated that no purely viscous fluid has thus far been observed exhibiting any time dependent flow behavior in unsteady configurations. Giesekus, therefore, argued that the cross viscosity represented by φ_2 should be set to zero, i.e., $\varphi_2 = 0$, for the description of purely viscous liquids. Accordingly, Eq. (6) reduces to

$$\underline{\tau} = \varphi_1 \left(II_D, III_D \right) \underline{D} = 2\eta \left(II_D, III_D \right) \tag{7}$$

where η represents an apparent viscosity depending on the second and third invariants of the deformation rate tensor. The most relevant type of flow considered in this work is a simple shear flow, where the deformation rate tensor can be written as

$$\underline{D} = \frac{\dot{\gamma}}{2} \begin{pmatrix} 0 & 1 & 0 \\ 1 & 0 & 0 \\ 0 & 0 & 0 \end{pmatrix} \tag{8}$$

with $\dot{\gamma}$ denoting the shear rate du_1/dx_2 . The invariants of the deformation rate tensor read

$$I_D = 0, \quad II_D = \frac{-\dot{\gamma}^2}{4}, \quad III_D = 0. \tag{9}$$

Assuming incompressible fluid with zero cross viscosity the stress components read

$$\tau_{11} = \tau_{22} = 0, \tag{10}$$

$$\tau_{11} = \tau_{22} = 0, \tag{11}$$

$$\tau_{12} = \tau_{21} = \frac{1}{2}\varphi_1\left(\dot{\gamma}^2\right)\dot{\gamma}, \tag{12}$$

$$\tau_{13} = \tau_{23} = 0, \tag{13}$$

which implies that the apparent shear viscosity is written as

$$\eta\left(\dot{\gamma}^2\right) = \frac{1}{2}\varphi_1\left(\dot{\gamma}^2\right). \tag{14}$$

Guided by the work of Chhabra 2010, it is possible to distinguish between several types of fluids based on the way viscosity depends on the shear rate:

- Shear thinning fluids
- Shear thickening fluids
- Bingham plastics

Different shear rate dependent behaviors of the fluid are illustrated in Figure 6.

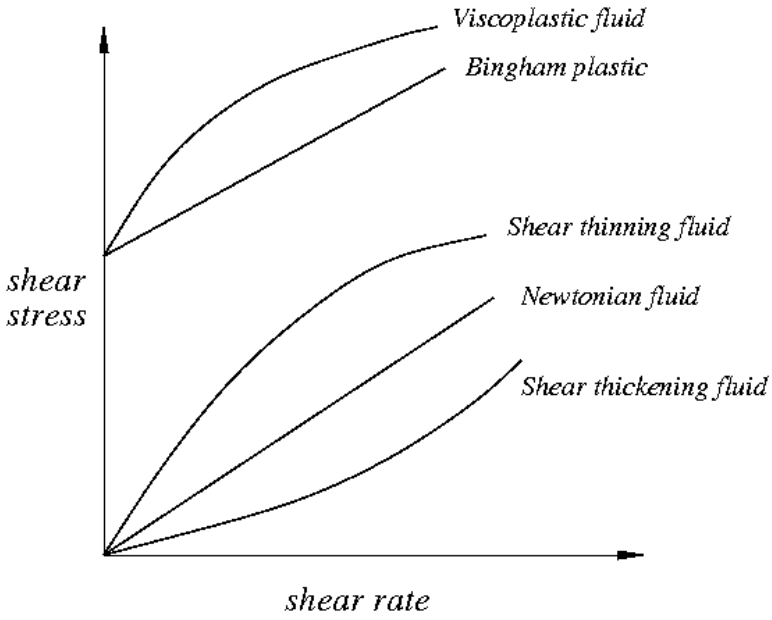

Figure 6: Shear rate dependent fluid behavior

2.1.1 Shear thinning fluids

This type of rheological behavior of the fluid can be observed as the most common type of non-Newtonian fluid behavior in various engineering applications. Its apparent viscosity written as

$$\eta = \frac{\tau_{12}}{\dot{\gamma}} \tag{15}$$

is not a fixed material property, but gradually decreases with increasing shear rate. In general the apparent viscosity approaches asymptotically constant levels for vanishing and infinite shear rates termed Newtonian plateaus. The so called first Newtonian plateau defined as

$$\lim_{\dot{\gamma}\to 0} \frac{\tau_{12}}{\dot{\gamma}} = \eta_I \tag{16}$$

is reached for vanishingly small shear rates, while the so called second Newtonian plateau written as

$$\lim_{\dot{\gamma}\to\infty} \frac{\tau_{12}}{\dot{\gamma}} = \eta_{II} \tag{17}$$

is approached for very high shear rates. Such a shear thinning trend between two Newtonian plateaus is typically observed with polymer solutions, where the second Newtonian plateau is usually close to the value of the molecular viscosity of the pure solvent.

2.1.2 Shear thickening fluids

In shear thickening liquids the apparent viscosity of the fluid increases with increasing shear rate. This type of behavior can usually be observed in concentrated suspensions. The variation of the apparent viscosity illustrated in Figure 7 exemplarily shows a possible mechanism of shear thickening depending on the applied shear. At very low shear rates or shear stresses the particles remain in an equilibrium state, where only the random collisions between them generate a certain resistance against the motion of the fluid. For further increased shear rates or shear stresses the particles are redistributed in such a way that their mobility is increased, resulting in a reduction of the apparent viscosity. Exceeding a certain limit in shear rate or shear stress finally leads to the formation of larger agglomerates of particles impeding the motion, such that the apparent viscosity increases.

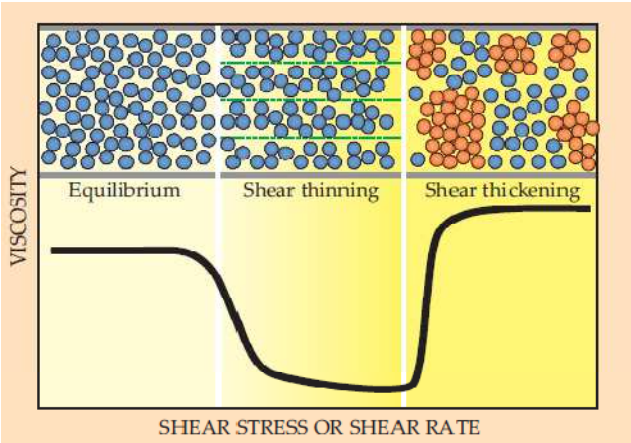

Figure 7: Shear thickening phenomena (adopted from Wagner et al. 2009)

These particular types of fluids were rarely investigated in the past. Due to the rising application of highly concentrated suspensions in various industrial applications, they are becoming an increasingly interesting topic for basic and applied research.

2.1.3 Bingham plastics

A Bingham plastic is defined as a viscoplastic material that behaves as an elastic solid as long as the shear stress applied on it is lower than the critical value (yield stress). When the yield stress is exceeded, the material behaves like a Newtonian or also non-Newtonian shear thinning/thickening fluid. Figure 8 exemplarily shows the respective flow curves. Tooth paste, mud, or slurries are typical representatives of these fluids.

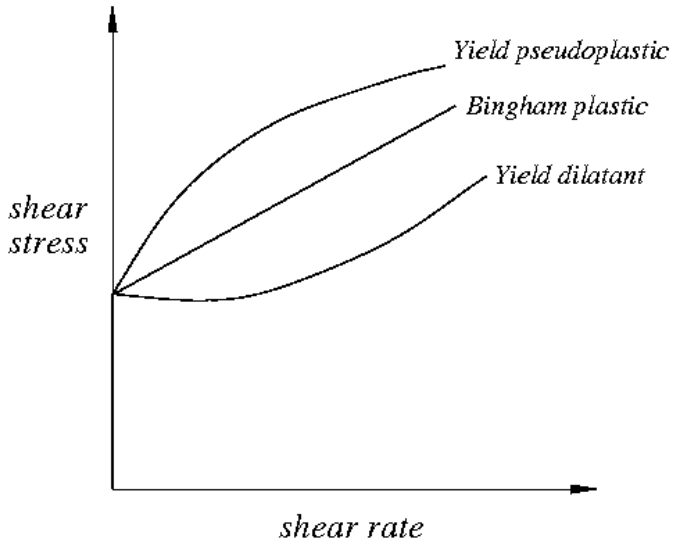

Figure 8: Flow curve of viscoplastic fluids

2.1.4 Newtonian fluids

In a case of simple linear dependence of the stress tensor on the deformation rate tensor which is associated with the coefficients

$$\varphi_0 = 0,\ \varphi_1 = 2\eta,\ \varphi_2 = 0, \tag{18}$$

Eq. (6) becomes

$$\underline{\tau} = 2\eta \underline{D}. \tag{19}$$

These types of fluids are so called Newtonian fluids. Their apparent viscosity, denoted by η in Eq. (19), does not depend on the deformation rate and is termed dynamic shear viscosity.
Examples of fluids which exhibit Newtonian behavior are water, alcohols, low molecular weight organic or inorganic solutions, molten metals etc., and all gases. In Newtonian fluids the

viscosity represents a pure material property which may only change with pressure and temperature. The viscosity of the liquids generally decreases with temperature and increases with pressure. Table 1 shows viscosities of different Newtonian fluids ranging from the low values for gases to high values met in oils.

Table 1: Viscosities of different Newtonian fluids at 20 °C

Fluid	Shear dynamic viscosity [Pas]
Air	1.8×10^{-4}
Water	1.0×10^{-3}
Mercury	1.6×10^{-3}
Automotive engine oil (SAE 10W30)	1.3×10^{-1}

A typical flow behavior of a Newtonian fluid can be shown in an example of a simple shear flow configuration, as met in a Couette flow between two parallel plates, where the upper one is moving at the fixed velocity U_w, shown in Figure 9.

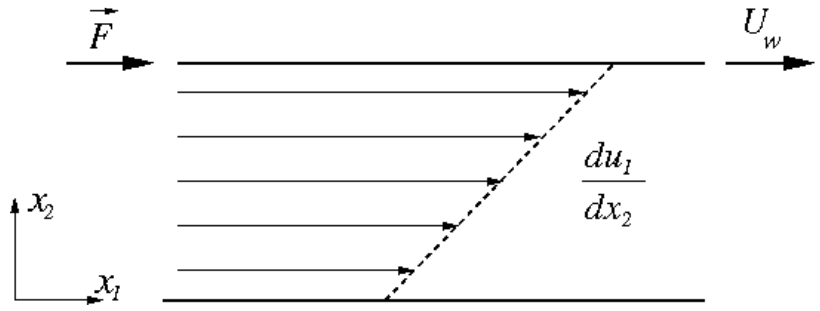

Figure 9: Couette flow between two parallel plates

The movement of the top plate due to the applied force in the *x*-direction drives the motion of the fluid layers beneath down to the bottom wall. The moving plate leads to a continuous angular deformation (shear) of the fluid, which is determined by the velocity gradient in the *y*-direction,

termed shear rate $\dot{\gamma} = du_1 / dx_2$. The applied tangential force per unit area τ_{12} (shear stress) is directly related to the angular deformation rate $\dot{\gamma}$(shear rate) through

$$\tau_{12} = \eta \frac{du_1}{dx_2}, \tag{20}$$

In the Newtonian case a linear velocity profile can be observed, due to the shear rate independent viscosity of the fluid, as shown in Figure 9.

2.2 Fluids with time dependent stress-strain relation

If the apparent shear viscosity η, as specified in Eq.(7), does not only depend on the instantaneous invariants of the deformation rate tensor but also on their histories, two types of fluids can be distinguished:

- Thixotropic fluids
- Rheopectic fluids

If some part of the deformation of the fluid is not permanent, as in the case of purely viscous fluids, but vanishes after a stress relaxation, similar to the case of an elastic body, the fluid is in general termed visco-elastic. The constitutive equation for the dependence of the shear stress on the deformation rate includes a temporal derivative involving a relaxation time specific for the considered visco-elastic fluid, as will be shown below.

2.2.1 Thixotropic fluids

If the viscosity decreases with time when shearing the fluid, it is called thixotropic. In principle, all liquids feature thixotropic behavior depending on the difference in the dynamics of internal structure breakage due to the shear applied and build-up due to the free motion of particles (Brownian motion). An example of a typical flow curve of a thixotropic fluid is shown in Figure 9. When subjected to a gradually increasing deformation the fluid reaches point denoted A. Keeping the constant deformation rate over a certain period of time results in a decrease of the

fluids viscosity, such that the shear stress decreases (point B). If the deformation rate would be kept constant for an infinite period of time, this would result in a further decrease of viscosity towards a theoretically minimal apparent viscosity, associated with point $B_{t\to\infty}$.

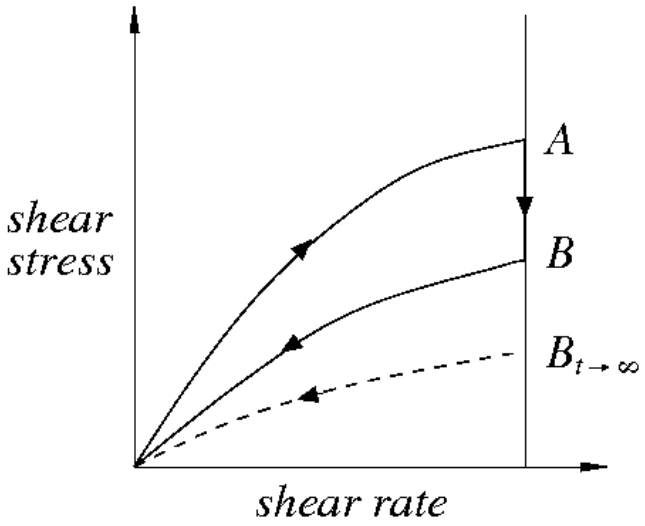

Figure 10: Flow curve of thixotropic fluids

2.2.2 Rheopectic fluids

Rheopectic behavior represents the inverse behavior of the previously described thixotropic behavior. This means that the apparent viscosity of the rheopectic fluid increases with the duration time of shearing, resulting from a build-up of a flow impeding internal structures inside the fluid under the influence of an external shear. Rheopectic behavior is not as common in the technical application as thixotropic behavior. Examples are gypsum pastes and printer inks.

The phenomenon of rheopexy can be illustrated analogously to thixotropic behavior, as shown in Figure 10. When a certain deformation rate is applied the fluid reaches state A. A constant deformation rate applied over a certain period of time results in an increase in the viscosity leading to an increase in shear stress towards point B. $B_{t\to\infty}$ is associated with the maximum possible value of apparent viscosity which would be reached, if a certain shear rate is applied over an infinite period of time.

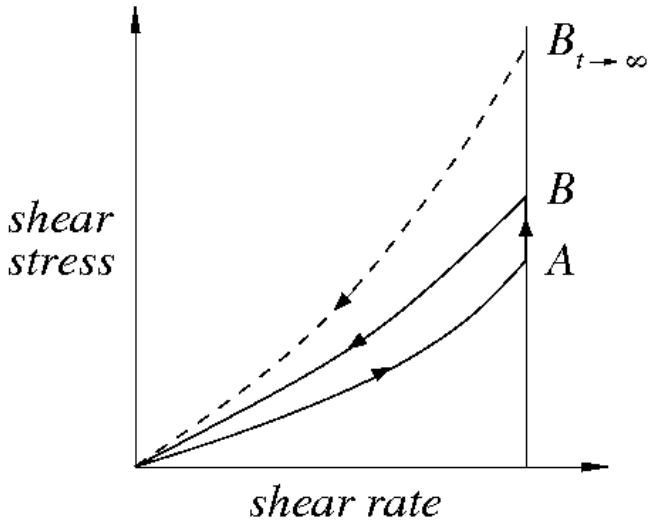

Figure 11: Flow curve of rheopectic fluids

2.2.3 Visco-elastic fluids

Visco-elastic fluids basically feature material properties of elastic solids and viscous liquids when subject to mechanical stress. A widely used constitutive equation for the dependence of the stress on the deformation is written as

$$\underline{\tau} + \underbrace{\Lambda\left(II_D\right)\frac{\mathcal{D}\underline{\tau}}{\mathcal{D}t}}_{elastic} = \underbrace{2\eta\left(II_D\right)\underline{D}}_{viscous}. \tag{21}$$

This equation, generally termed White-Metzner model, covers the most important flow properties of many viscoelastic fluids. The unsteady term on the lhs involves a relaxation time scale $\Lambda=\Lambda(II_D)$ and the so called Oldroyd derivative written as

$$\frac{\mathcal{D}\underline{\tau}}{\mathcal{D}t} = \frac{\partial\underline{\tau}}{\partial t} + \vec{v}\cdot\nabla\underline{\tau} - \left[\left(\nabla\vec{v}\right)^T\cdot\underline{\tau} + \underline{\tau}\cdot\left(\nabla\vec{v}\right)\right]$$

In the viscous contribution on the rhs η denotes the apparent viscosity, also dependent on the second invariant of the deformation rate tensor. Many materials in the industrial application today show visco-elastic properties, for example, polymer melts, concentrated polymer solutions, gels, foams, etc.

2.3 Flow models for purely viscous non-Newtonian fluids

Generally speaking all fluids which do not exhibit the simple linear shear stress dependence on the deformation rate as given in Eq. (19) are termed non-Newtonian fluids. Since we consider only shear thinning and, possibly, shear thickening non-Newtonian fluids, as described in subsections 2.1.1 and 2.1.2, well established flow models for only these fluids shall be discussed here. A very popular model assumes a simple power-law dependence of the apparent viscosity on the shear rate, written as

$$\eta = m\left(\dot{\gamma}\right)^{n-1}. \tag{22}$$

For exponents $n<1$ Eq. (22) describes shear thinning, for $n>1$ shear thickening, and $n=1$ Newtonian fluid behavior. The main drawback of this simple model is its inability to capture the appearance of the asymptotic transition to Newtonian plateaus at low and high shear rates. Additionally, the shear thinning formulation associated with $n<1$ produces a singularity for vanishing shear rate $\dot{\gamma}\rightarrow 0$. As such the model cannot cover the full range of possible shear rates. The Ellis model was developed to eliminate this shortcoming of the shear thinning power-law model at vanishingly low shear rates. The Ellis model expresses the apparent viscosity as a function of shear stress (see Chhabra and Richardson 2008) written as

$$\eta = \frac{\eta_I}{1+\left(\tau/\tau_{1/2}\right)^{\alpha-1}}. \tag{23}$$

Therein, η_I represents the zero shear rate viscosity associated with the first Newtonian plateau, which is approached for vanishing shear stress $\tau \rightarrow 0$. The coefficients α and $\tau_{1/2}$ are determined from a best-fit to measured flow curves. It is evident that Eq. (23) describes Newtonian fluid behavior, when the denominator is unity, which is achieved by setting the α =1, or $\tau_{1/2}$ to infinity. Setting the exponent greater than unity the expression describes shear thinning behavior. The models proposed by Cross 1965, Bird and Carreau 1968, and Carreau and Yasuda (see Barnes et al. 1989), essentially provide a formulation which correctly describes the asymptotic behavior for very low and high shear rates as well as transitional regime in terms of a smooth S-shaped function of $\dot{\gamma}$. The Cross model reads

$$\frac{\eta - \eta_{II}}{\eta_I - \eta_{II}} = \frac{1}{1 + m\left(\dot{\gamma}\right)^n}, \tag{24}$$

where η_I and η_{II} represent the viscosities of the first and second Newtonian plateaus approached for $\dot{\gamma} \rightarrow 0$ and $\dot{\gamma} \rightarrow \infty$, respectively. The parameter *m* basically determines the length of the first Newtonian plateau and *n* determines how fast η varies with $\dot{\gamma}$ in the transition to the second Newtonian plateau. The Carreau-Yasuda model uses a very similar formulation written as

$$\frac{\eta - \eta_{II}}{\eta_I - \eta_{II}} = \frac{1}{\left[1 + \left(K_1 \dot{\gamma}\right)^2\right]^{m_{1/2}}}. \tag{25}$$

Alike the parameters *m* and *n* in Eq. (24) the coefficient K_1 determines the length of the first Newtonian plateau, allowing to adjust the point of transition towards the second Newtonian plateau as observed in the measured data, and $m_{1/2}$ determines the steepness of the flow curve in the transition between the two plateaus. A flow curve generated using the Carreau-Yasuda model is exemplarily shown in Figure 11.

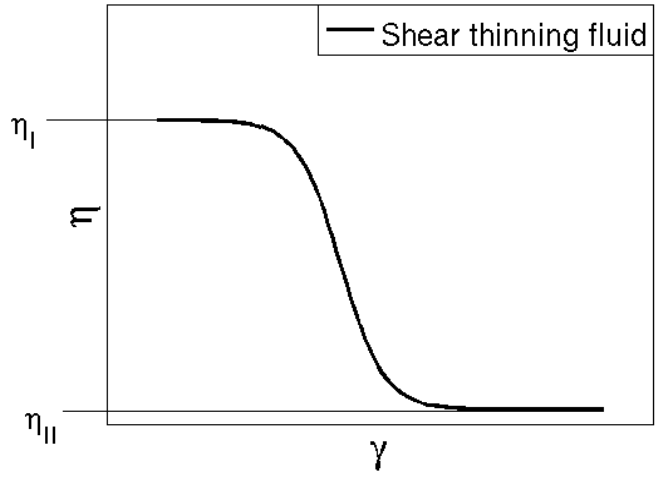

Figure 12: Shear thinning behavior described by the Carreau-Yasuda model

2.4 Materials for wire enameling

The main task of the wire enameling solid component is to provide a continuous insulation which avoids a possible occurrence of a short circuit between adjacent windings of the wire. For the accomplishment of this task the wire enamel has to fulfill some specific requirements, such as high chemical and thermal resistance, good adhesion to copper and a sufficient mechanical resistance. The quality of the final product is commonly assessed in measurements of special enameled wire properties and a comparison of these data against certain standards which are, for example, prescribed by the IEC (International Electrical Commission). The solid material which meets the imposed requirements to a high degree is polyester-imide. It is therefore nowadays most commonly applied in wire enameling, and its global production was increased to the level of tens of thousands of tons per year.

2.4.1 Polyester-imide

Before the application of polyester-imide, polyethylene teraphthalate (PET) based polyesters were applied for coating copper wires, even though the excellent properties of polyamides were

already known. Despite the positive properties of polyimides, they were not applied due to the difficulty in handling these types of materials. On the other hand polyesters exhibited good flexibility, processability, and stability when stored. In order to get good properties from both of the groups of materials, they were combined, and polyester-imide was created. The formation reaction of polyester-imide is illustrated in Figure 13. The imide part of the compound enabled an improvement in mechanical and thermal properties as well as thermal endurance, but it lowered the level of adhesion on the copper and reduced the softening temperature of the polymer film. The softening temperature was regained and elevated by the addition of tris-(2-hydroxyethyl)-isocyanurate (THEIC).

The group of polyester-imides can be further subdivided into two large categories: saturated and unsaturated polyester-imides. Saturated polyester-imides can be produced by modifying polyesters with structures that contain imide.

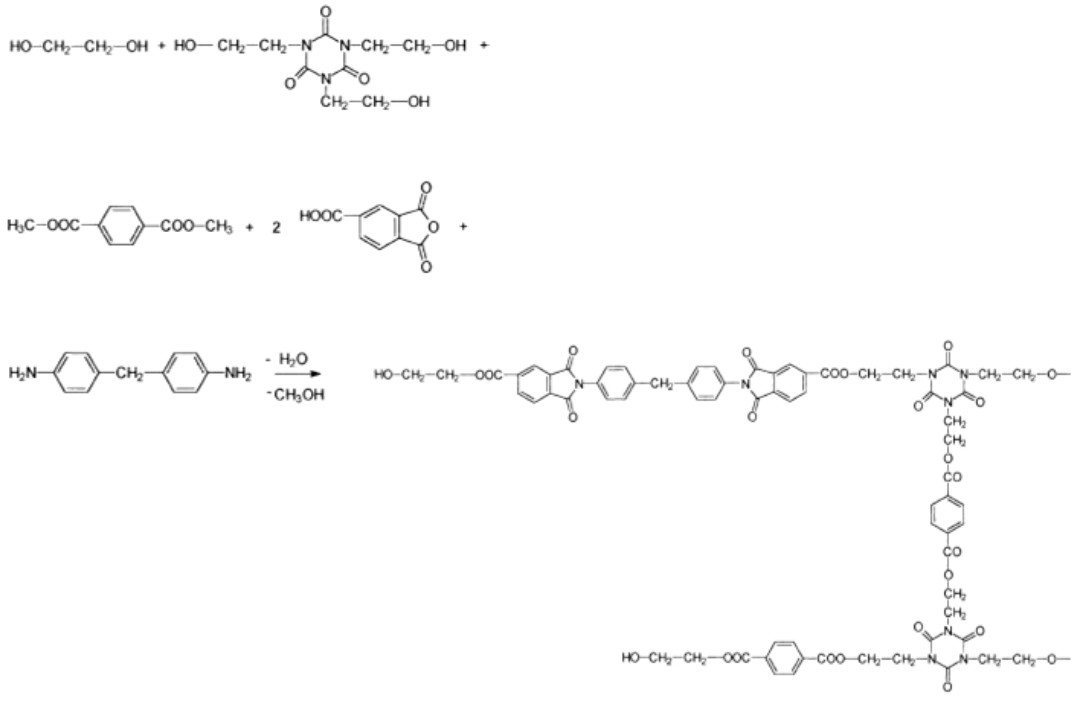

Figure 13: Polyester-imide formation reaction (adopted from Linert, 1999)

The polyester-imide resins are produced from ethylene glycol, THEIC, dimethyleterephtalate, trimellitic anhydride and 4,4-diaminodiphenylmethane. The production process involves esterification reactions between diols, triols and acids, and cycle forming reactions between diamine and anhydride. The esterification requires certain amount of catalysts in order to intensify the reaction. Different types of catalysts can be applied. The contemporary production processes of polyester-imide resins are usually realized as one step processes. For the application on the wire surface the resin has to be dissolved. The solvent generally applied in the case of wire enamels is cresol. Cresol is widely accepted due to its affordable price and convenient properties. For example, it can be adjusted to a certain boiling range, as required by the wire enameling process. Furthermore, the addition of different additives does not cause a significant reduction in dissolving power. It further has a high specific reaction enthalpy of combustion of 34200 kJ/kg, which is used for heating the hot drying and curing sections of the enameling machines. The specific reaction enthalpy is catalytically released burning the evaporated solvent. The disadvantages of cresol are its toxicity and its very intensive smell, which requires handling of the enamels with special care. There were several attempts to replace cresol by an alternative solvent, which would be less toxic and easier to handle. Tests performed with cresol-free polyester-imide wire enamels showed that the all of the proposed alternatives had lower dissolving power which resulted in less hydrocarbons blended in the structure and in the end lower specific reaction enthalpy, which is not favorable in the modern wire enameling machines. Apart from the resins and solvent, other additives may be added to the formulation of the wire enamel. Among these are catalysts, which support the transesterification reactions during the curing process.

The second large group of polyester-imides are the unsaturated polyester-imides. Their usual area of application is the impregnation of the electrical coils. The impregnation has the task of protecting the coil against water or some corrosive chemicals that can be present in the environment, where a certain device is applied. Additionally, these types of coatings enable better thermal conductivity. An important practical application is the insulation of the coils of electric motors. Applying unsaturated polyester-imides allows for the reduction in size of an

electric motor without losing power. The solution is deposited on the coils by dip coating and cured at temperatures between 130°C and 160°C. The resin copolymerizes very rapidly.

In the magnet wire production process, after exiting the enameling dies with a defined fresh coating the wire enters the oven, where the deposited enamel is dried and cured. During this process the solvent and the resins are cured. The temperatures in the oven rise to 700°C. When the content of the solvent is reduced to about 60% of the initial value the curing process starts. In order to achieve a high final quality of the coating, the thickness of the deposited fresh enamel layers should be sufficiently small. In case of a too thick layer, imperfections like blisters can appear after the curing, which would make the enameled wire unusable. For this reason, the coating is applied in multiple deposition steps by passing the wire successively through the dies, gradually increasing the thickness of the coating in each pass. The evaporated solvents have to be kept inside the wire enameling machines to become finally burned catalytically with a very high level of efficiency resulting in very low emission of waste gases. The high temperatures of the exhaust gasses are used in heat exchangers to preheat the drying air entering the system.

2.5 Viscosity measurements

The commonly used experimental techniques are generally based on the measurement of the forces which are required to deform the fluid in a defined and controlled manner. The desired rate of deformation can be produced in different ways, for example by dragging the fluid with a moving (sliding or rotating) solid, by forcing the fluid through a geometry imposing a pressure gradient or using gravitational force, by sinking a body submersed in the fluid, etc. Depending on the way how the flow, and hence the deformation, is induced, viscometers can be divided in certain classes, as listed in Table 2 following Macosko, 1994.

Table 2: Viscometer classification (adopted from Macosko, 1994)

Drag Flow Types: Flow set by motion of instrument boundary/surface using external or gravity force.	
Type/Geometry	Basic characteristics/Comments
Rotating concentric cylinders (Couette)	Good for low viscosity, high shear rates; for $R_2/R_1 \cong 1$, see Figure 30.3; hard to clean thick fluids
Rotating cone and plate	Homogeneous shear, best for non-Newtonian fluids and normal stresses; need good alignment, problems with loading and evaporation
Rotating parallel disks	Similar to cone-and-plate, but inhomogeneous shear; shear varies with gap height, easy sample loading
Sliding parallel plates	Homogeneous shear, simple design, good for high viscosity; difficult loading and gap control
Falling body (ball, cylinder)	Very simple, good for high temperature and pressure; need density and special sensors for opaque fluids, not good for viscoelastic fluids
Rising bubble	Similar to falling body viscometer; for transparent fluids
Oscillating body	Needs instrument constant, good for low viscous liquid metals
Pressure Flow Types: Fluid set in motion in fixed instrument geometry by external or gravity pressure	
Type/Geometry	Basic characteristics/Comments
Long capillary (Poiseuille flow)	Simple, very high shears and range, but very inhomogeneous shear, bad for time dependency, and is time consuming
Orifice/Cup (short capillary)	Very simple, reliable, but not for absolute viscosity and non-Newtonian fluids
Slit (parallel plates) pressure flow	Similar to capillary, but difficult to clean
Axial annulus pressure flow	Similar to capillary, better shear uniformity, but more complex, eccentricity problem and difficult to clean
Others/Miscellaneous:	
Type/geometry	Basic characteristics/Comments
Ultrasonic	Good for high viscosity fluids, small sample volume, gives shear and volume viscosity, and elastic property data; problems with surface finish and alignment, complicated data reduction

Since the measurement principles in general assume perfect flow conditions, such as fully developed flow, an infinitely extended domain, negligible viscous heating, laminar flow, etc., any possible deviations from these ideal conditions result in errors, exemplarily listed in Table 3.

Table 3: Viscometer errors (adopted from Macosko, 1994)

Error/Effect	Cause/Comment
End/edge effect	Energy losses at the fluid entrance and exit of main test geometry
Kinetic energy losses	Loss of pressure to kinetic energy
Secondary flow	Energy loss due to unwanted secondary flow, vortices, etc.; increases with Reynolds number
Nonideal geometry	Deviations from ideal shape, alignment, and finish
Shear rate non-uniformity	Important for non-Newtonian fluids
Temperature variation and viscous heating	Variation in temperature, in time and space, influences the measured viscosity
Turbulence	Partial and/or local turbulence often develops even at low Reynolds numbers
Surface tension	Difference in interfacial tensions
Elastic effects	Structural and fluid elastic effects
Miscellaneous effects	Depends on test specimen, melt fracture, thixotropy, rheopexy

2.5.1 Drag flow type viscometers

According to the classification in Table 2, drag flow type viscometers are the ones where the motion of the examined fluid is induced by the motion of a solid surface. The most well known representatives of this group are so called rotational viscometers. Among these, the concentric cylinder type viscometer shall be described in more detail here, because this measuring technique was mostly applied in this work. Other alternative measuring techniques will just be briefly addressed.

The rotational viscometer is essentially designed to apply a defined constant shear rate on the fluid for the longer period of time. This feature allows for steady state measurements of the fluid's viscosity for a given range of shear rates, but also for the experimental investigation of a possible time dependent flow behavior of the fluid. Furthermore, it is possible to measure the effect of the temperature on the viscosity, if the temperature of the fluid can be controlled.

As shown in Figure 14 the experimental device usually consists of an outer cylinder and a concentric inner cylinder. The gap between two cylinders is filled with the investigated fluid. Usually, the measurements consist in measuring the torque exerted on the stationary cylinder and the rotational speed of the moving cylinder.

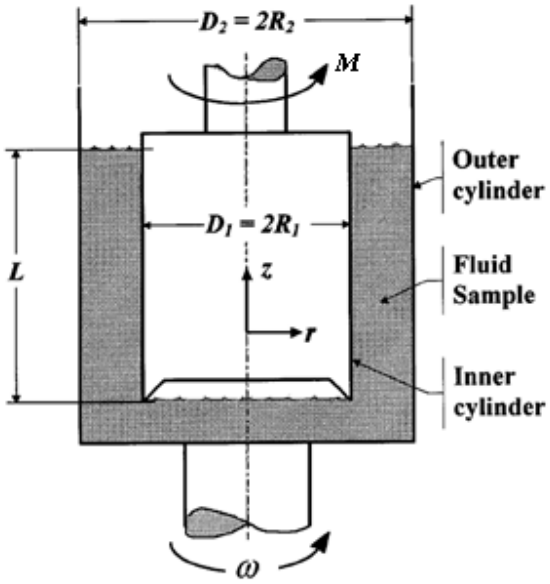

Figure 14: Concentric cylinders viscometer (adopted from Macosko, 1994)

From the known torque on the inner cylinder and the geometry it is possible to determine the shear stress at any given radius inside the gap between the two cylinders from the expression

$$\tau_{r\theta}(r) = \frac{M}{2\pi r^2 L_e}. \tag{26}$$

The effective length $L_e = L + L_c$ represents the real length of the cylinder L modified by a so called end-effect correction L_c. Accounting for the fact that the torque is constant at all radial positions it is possible to write

$$\frac{M}{2\pi L_e} = \tau_1 R_1^2 = \tau_2 R_2^2 = \tau_m R_m^2, \tag{27}$$

where τ_m denotes a representative shear rate exerted at a certain representative radius R_m. This radius is computed from Eq. (27) as

$$R_m = R_1\left(\frac{2\beta^2}{1+\beta^2}\right)^{1/2} = R_2\left(\frac{2}{1+\beta^2}\right)^{1/2}, \tag{28}$$

where β denotes the ratio between the radii of the two cylinders written as

$$\beta = \frac{R_2}{R_1}. \tag{29}$$

Since the gap between the two cylinders is very small ($\beta \approx 1$), it is possible to assume a planar Couette type flow associated with a linear velocity profile between the inner and the outer cylinder, regardless of the fluid type being measured. Due to this assumption the angular velocity at any radial position, induced by the motion of the outer cylinder rotating with the angular speed ω, reads

$$v_\theta(r) = R_2\,\omega\frac{r-R_1}{R_2-R_1}, \tag{30}$$

which implies a uniform shear rate inside the gap written as

$$\dot{\gamma}_m = \frac{\partial v_\theta}{\partial r} = \frac{\omega}{\beta-1}\beta. \tag{31}$$

Expressing the representative shear stress in terms of the representative radius according to Eq. (27), and using the Eqs. (28) and (31) the apparent viscosity is determined as

$$\eta = \eta_m = \frac{\tau_m}{\dot{\gamma}_m} = \left[\frac{\left(\beta^2 + 1\right)(\beta - 1)}{4\pi R_2^2 L_e \beta} \right] \frac{M}{\omega}. \tag{32}$$

It was shown in the work of Jimenez and Kostic 1993, that the present model, which is independent of the fluid's rheology, covers very well a large variety of fluid behaviors. For example, considering non-Newtonian power-law fluids, the present concept provides values for the viscosity with an accuracy of ±1% for the range of the power-law exponent *n* between 0.35 and 3.5 and concentric cylinder radii ratios β between 1 and 1.2.

One further effect that should be taken into account is the appearance of possible secondary flow structures in form of the vortices which can affect the measurement results. Even though in the Couette type viscometers there are no vortex structures to be expected inside the narrow gap between the cylinders, they may appear near the bottom end of the inner cylinder. The transition to turbulent flow can become an additional issue, if the Reynolds number defined as

$$\mathrm{Re} = \frac{\rho \omega R_1^2}{2\eta}\left(\beta^2 - 1\right) \tag{33}$$

reaches values between 10^3 and 10^4.

2.5.2 Pressure flow type viscometers

As already outlined above, in this type of technique the motion of the fluid is induced by pressure or gravitational forces. A popular representative of this technique is the capillary viscometer, as illustrated in Figure 15. This technique was used in the present work as well and will therefore be discussed here in more detail.

The main assumption regarding the flow inside these types of viscometers is a fully developed laminar pipe flow. The geometry of these devices is designed in such a way that the length of the capillary tube is much larger than the diameter of the tube. The quantities which are measured in

this type of viscometer are the flow rate of the fluid and the axial pressure difference between the two measuring points.

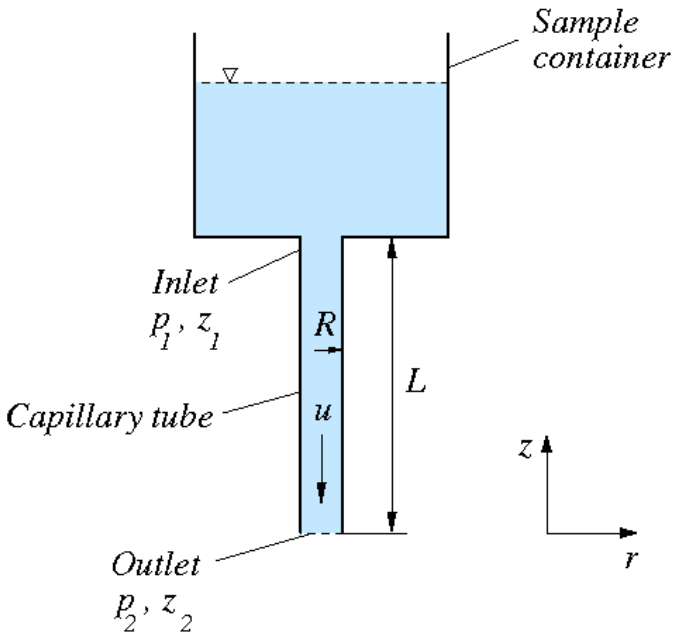

Figure 15: Capillary viscometer

In general the viscosity of a fluid can be obtained from the ratio between the shear stress and shear rate at the wall

$$\eta = \frac{\tau_w}{\dot{\gamma}_w}. \tag{34}$$

A simple momentum balance applied to a control volume of axial length L provides the wall shear stress in terms of the measured axial pressure difference written as

$$\tau_w = \left(\frac{R}{2L} \right) \Delta p. \tag{35}$$

The shear rate at the wall, which is obtained as

$$\dot{\gamma}_w = -\left.\frac{du}{dr}\right|_{r=R} \tag{36}$$

basically requires the knowledge of the radial profile of the axial velocity $u(r)$. For a Newtonian fluid this can be easily computed yielding the well-known parabolic Hagen-Poiseuille profile, which finally gives the following linear relation between the wall shear rate and the measured volumetric flow rate:

$$\dot{\gamma}_{w,N} = \left(\frac{4}{\pi R^3}\right)\dot{V} \tag{37}$$

For non-Newtonian fluids the dependence of the viscosity on the shear rate excludes an a priori computation of the velocity profile, which is required to evaluate the wall shear rate from the derivative (36) producing finally a relation to the volumetric flow rate similar to Eq. (37). In the non-Newtonian case the wall shear rate is therefore computed in an alternative way. The starting point is the general expression for the volumetric flow rate written as

$$\dot{V} = \int_0^R 2\pi r u(r)\, dr. \tag{38}$$

Integration of this equation by parts yields

$$\dot{V} = \underbrace{\pi r^2 u(r)\Big|_0^R}_{=0} - \int_0^R \pi r^2 \frac{du}{dr}\, dr. \tag{39}$$

For fully developed pipe flow the shear stress always varies linearly with the radial coordinate as

$$\frac{\tau}{\tau_w} = \frac{r}{R}, \tag{40}$$

regardless of the rheological flow behavior. Using Eq. (40) the radial coordinate r can be substituted by the shear stress τ, such that the Eq. (39) can be rewritten as

$$\dot{V} = \pi \frac{R^3}{\tau_w^3} \int_0^{\tau_w} \tau^2 \dot{\gamma} d\tau, \tag{41}$$

where $\dot{\gamma}$ denotes the shear rate at position r given as

$$\dot{\gamma} = -\frac{du}{dr}. \tag{42}$$

Equating the volumetric flow rates obtained in the case of Newtonian, given by Eq. (37), with the Eq. (41) obtained for non-Newtonian fluids yields

$$\frac{\pi R^3 \tilde{\dot{\gamma}}_{w,N}}{4} = \pi \frac{R^3}{\tau_w^3} \int_0^{\tau_w} \tau^2 \dot{\gamma} d\tau, \tag{43}$$

where $\tilde{\dot{\gamma}}_{w,N}$ represents an "equivalent Newtonian wall shear rate". Taking the derivative of Eq. (41), with respect to τ_w gives

$$\dot{\gamma}_w = \frac{3}{4}\tilde{\dot{\gamma}}_{w,N} + \frac{1}{4}\tau_w \frac{d\tilde{\dot{\gamma}}_{w,N}}{d\tau_w}, \tag{44}$$

which can be transformed into

$$\dot{\gamma}_w = \frac{\tilde{\dot{\gamma}}_{w,N}}{4}\left(3 + \underbrace{\frac{d\ln\tilde{\dot{\gamma}}_{w,N}}{d\ln\tau_w}}_{s}\right), \tag{45}$$

The correction parameter s is obtained by measuring different operating points associated with different flow rates $\dot{V}$ and pressure differences Δp. The variations in $\dot{V}$ and Δp translate via Eqs. (37) and (35) into corresponding variations in $\tilde{\dot{\gamma}}_{w,N}$ and τ_w, which are used to estimate s. Using $\dot{\gamma}_w$ from (45) and τ_w from (35) finally gives the apparent viscosity η, according to Eq. (34).

2.5.3 Other viscometer types

There are multiple other techniques using different phenomena to determine the viscosity of a fluid, but since they were not relevant for this work, they shall be only briefly addressed in the following lines.

One of these alternative techniques, which is also based on the principle of drag flow viscometers, is the so called oscillating method. This method is particularly applied for measuring fluids with low expected values of viscosity ranging between 10^{-5} Pas and 10^{-2} Pas.

A further group of measuring techniques is based on the ultrasonic method. It relies on the fact that the dissipation of energy of an acoustic wave passing through the fluid is dependent on the viscosity of the fluid.

2.6 Viscosity measurements of wire coating enamels

One of the main prerequisites for a correct computational prediction of the drag force on the wire is a reliable description of the flow field inside the die, which is only possible with a correct modeling of the fluid behavior when subjected to shear. Two sets of measurements have been conducted in order to determine the shear rate dependent flow behavior of the wire enamels applied in the enameling process. The first set of measurements used a capillary viscometer to reach highest possible shear rates which are expected to appear inside the dies. These measurements were performed by the company BASF. The second set of measurements was conducted at the Research Centre for Pharmaceutical Engineering (RCPE) at the Graz University of Technology, using a concentric cylinders viscometer. Both sets of measurements were carried out for both basecoat and overcoat enamels supplied by the enamel producer company Elantas. As stated in the introductory part, enamels are polymer solutions, which differ within each group (basecoat and overcoat) dependent of the fraction of solid mass content contained by each solution. For the considered enamels the solid content of the solutions varied between 25% and 45%.

2.6.1 Capillary viscometer measurements

The high shear rate measurements were performed for the basecoats Terebec MT-533-25, Terebec MT-533-34, Terebec MT-533-41, Terebec MT-533-45, and the overcoats Sivamid 595-25, Sivamid 595-34, Sivamid 595-38. They were measured for shear rates ranging between $1x10^5$ and $2x10^6 s^{-1}$, at the constant temperature of 60°C. This temperature was selected according to the temperature of the enamel in the enamel tank during real application. The results shown in Figure 16 were repeatedly obtained in two consecutive sets of measurements in order to check the reproducibility of the results.

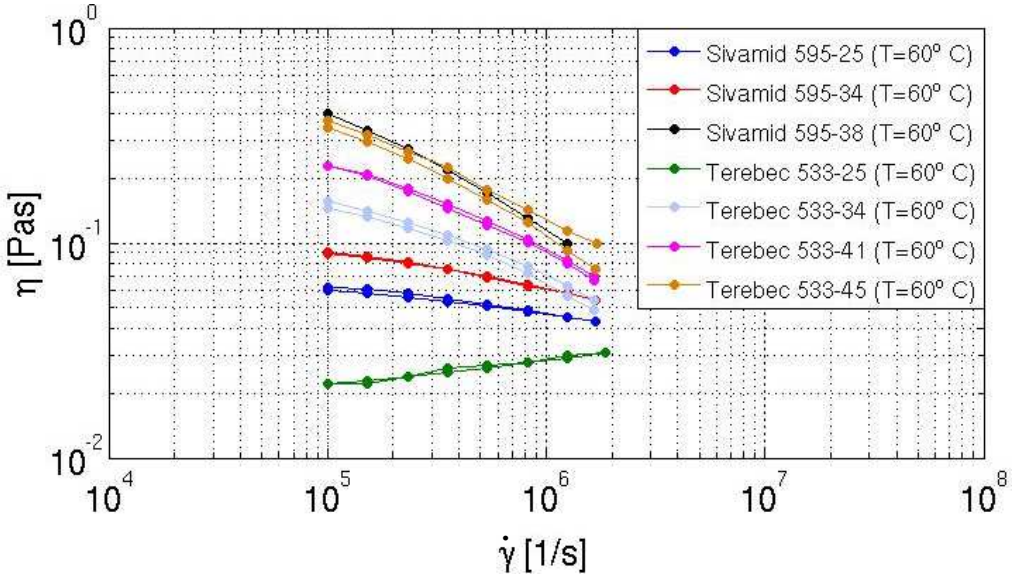

Figure 16: Viscosity measurements results – capillary viscometer

As seen from Figure 16 all enamels exhibit shear thinning behavior except Terebec 533-25, which shows a shear thickening tendency occurring on a very low level of viscosity though. Since the measurements do not cover the low shear rate range down to zero, they were redone using a concentric cylinders viscometer. The results obtained in this second set of measurements are shown in the following subsection.

2.6.2 Concentric cylinders viscometer measurements

The second set of measurements considered the same seven fluid samples of both basecoat and overcoat enamels as considered in the capillary viscometer measurements. The measurements were also conducted at the temperature of 60°C varying the shear rates from 1 s^{-1} to 7000 s^{-1}. The measurements were conducted three times for each fluid type in order to provide consistent reproducible results. Figure 17 shows the averaged viscosities as obtained from the three measurement cycles for each enamel.

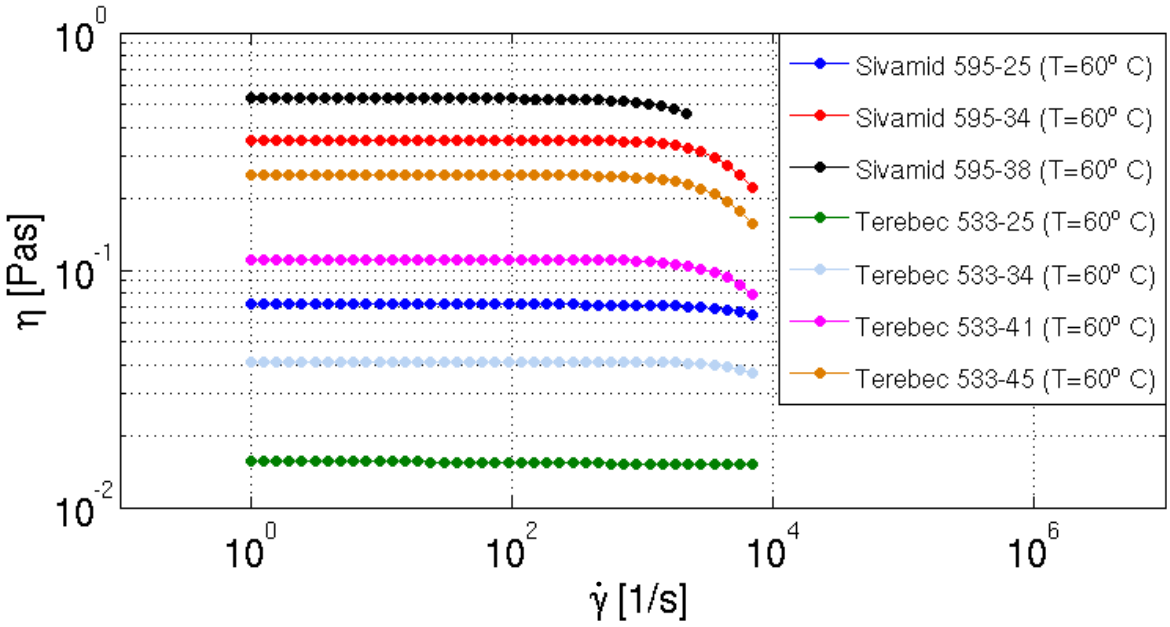

Figure 17: Viscosity measurements results - concentric cylinders viscometer

As seen from Figure 17 all enamels exhibit shear thinning properties. The measured range in the second set covers the range of the first Newtonian plateau, and the start of the transition towards the second Newtonian plateau for all fluids. When comparing the results obtained from the capillary viscometer measurements against those obtained from the concentric cylinders viscometer, a certain offset in the values can be observed. A possible reason for this offset may reside in the estimation of the parameter *s* appearing in the Eq. (45) for determining the wall shear rate as required in the estimation of the viscosity of non-Newtonian fluids in the capillary viscometry. Even small inaccuracies in this correction factor can significantly change the results leading to the observed discrepancies. Due to this uncertainty associated with the results of the capillary viscometer, the measurements obtained from the concentric cylinder viscometer appeared to be more reliable. Therefore, only these data were further used for modeling the flow behavior in the computations of the flow field evolving inside wire enameling dies.

3. ANALYTICAL MODEL

The present analytical model relies on lubrication theory approximation, whose most essential features are the neglect of inertial forces and the thin-layer approximation. This neglect appears to be justified due to the typically very small height of the gap between the moving wire and the radial outer contour of the die. The analytical model shall provide a reliable and computationally efficient approach for the analysis of the flow inside coating dies, which basically allows for a large variety of die shapes as well as non-Newtonian flow models. The computational analysis carried out with this approach focuses in particular on the effect of the non-Newtonian shear-thinning, or shear-thickening, behavior, and on the influence of the die geometry on the resulting total drag force. The effect of heat transfer is included as well. The considered material properties and operating conditions are selected based on real-life enameling applications. The results of the computational analysis shall help to determine die shapes which generate lowest possible drag total forces on the wire. Figure 18 shows the basic schematic of the generalized Couette flow met in coating dies. The flow is driven by a fast moving wire of velocity U_w. Due to the converging die geometry only a small portion of the enamel, which is entrained by the wire, finally forms the defined deposition layer.

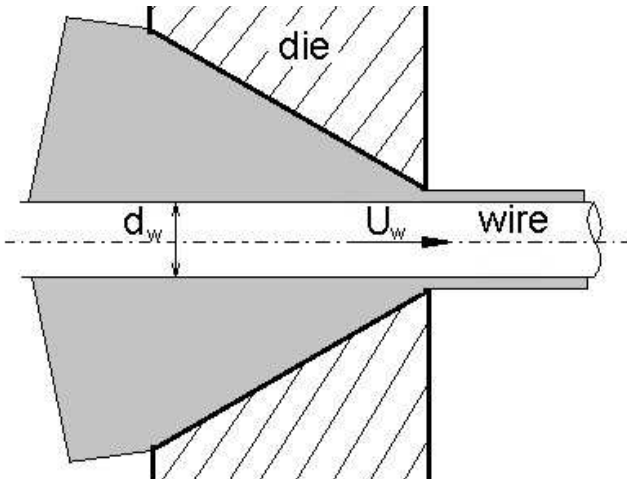

Figure 18: Flow configuration inside a coating die

3.1 Governing equations

The converging flow through the coating die is described in cylindrical coordinates, where the *z*-direction (axial direction) is aligned with the axis of the moving wire, as seen in Figure 19. The radial (cross-stream) direction r varies between the radius of the wire, $r=r_w$, and the outer contour of the die, $r=r_d\ (z)$. L denotes the axial length of the die. The flow is assumed as axisymmetric and steady.

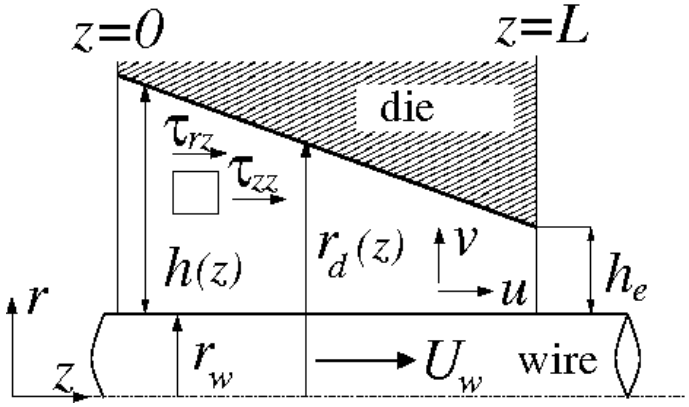

Figure 19: Schematic sketch of the computational domain

The governing conservation equations of axial momentum, radial momentum, and thermal energy read in dimensional form

$$\rho\left(u\frac{\partial u}{\partial z}+v\frac{\partial u}{\partial r}\right)=-\frac{\partial p}{\partial z}+\frac{1}{r}\frac{\partial\left(r\tau_{rz}\right)}{\partial r}+\frac{\partial\tau_{zz}}{\partial z}, \tag{46}$$

$$\rho\left(u\frac{\partial v}{\partial z}+v\frac{\partial v}{\partial r}\right)=-\frac{\partial p}{\partial r}+\frac{\partial\tau_{zr}}{\partial z}+\frac{1}{r}\frac{\partial\left(r\tau_{rr}\right)}{\partial r}-\frac{\tau_{\theta\theta}}{r}, \tag{47}$$

$$\rho c_p\left(u\frac{\partial T}{\partial z}+v\frac{\partial T}{\partial r}\right)=\lambda\frac{1}{r}\frac{\partial}{\partial r}\left(r\frac{\partial T}{\partial r}\right)+\tau_{rz}\left(\frac{\partial u}{\partial r}+\frac{\partial v}{\partial z}\right)+\tau_{rr}\frac{\partial v}{\partial r}+\tau_{\theta\theta}\frac{v}{r}+\tau_{zz}\frac{\partial u}{\partial z}, \tag{48}$$

with the normal and shear stresses written as

$$\tau_{rr} = 2\eta \frac{\partial u}{\partial r}, \quad \tau_{\theta\theta} = 2\eta \frac{v}{r}, \quad \tau_{zz} = 2\eta \frac{\partial u}{\partial z}, \quad \tau_{zr} = \tau_{rz} = \eta \left(\frac{\partial u}{\partial r} + \frac{\partial v}{\partial z} \right), \tag{49}$$

respectively. The conservation of mass is enforced by imposing a constant flow rate at each cross sectional position inside the die, which closes the governing set of equations:

$$\dot{V} = \int_{r_w}^{r_d} 2\pi r u dr = const. \tag{50}$$

The order of magnitude of the individual terms occurring in the formulation shall be estimated by non-dimensionalizing the equations, introducing the following normalized variables:

$$\begin{aligned} z^* &= \frac{z}{L}, \quad r^* = \frac{r}{h_e}, \quad u^* = \frac{u}{U_w}, \quad v^* = \frac{vL}{h_e U_w} \\ p^* &= \frac{p h_e^2}{\eta_I U_w L}, \quad \dot{V}^* = \frac{\dot{V}}{2\pi h_e^2 U_w}, \quad T^* = \frac{T}{T_w}, \quad \eta^* = \frac{\eta}{\eta_I}. \end{aligned} \tag{51}$$

The non-dimensionalized representation of the momentum equation in the axial direction, radial direction, energy equation, and the continuity equation read

$$\begin{aligned} &\varepsilon \left(u^* \frac{\partial u^*}{\partial z^*} + v^* \frac{\partial u^*}{\partial r^*} \right) = -\frac{\partial p^*}{\partial z^*} + \frac{1}{r^*} \frac{\partial}{\partial r^*} \left(r^* \eta^* \left(\frac{\partial u^*}{\partial r^*} + \left(\frac{h_e}{L} \right)^2 \frac{\partial v^*}{\partial z^*} \right) \right) + \\ &2 \left(\frac{h_e}{L} \right)^2 \frac{\partial}{\partial z^*} \left(\eta^* \frac{\partial u^*}{\partial z^*} \right), \end{aligned} \tag{52}$$

$$\varepsilon\left(\frac{h_e}{L}\right)^2\left(u^*\frac{\partial v^*}{\partial z^*}+v^*\frac{\partial v^*}{\partial r^*}\right)=-\frac{\partial p^*}{\partial r^*}+2\left(\frac{h_e}{L}\right)^2\frac{1}{r^*}\frac{\partial}{\partial r^*}\left(r^*\eta^*\frac{\partial v^*}{\partial r^*}+\right)-2\left(\frac{h_e}{L}\right)^2\eta^*\frac{v^*}{r^{*2}}+$$
$$\left(\frac{h_e}{L}\right)^2\frac{\partial}{\partial z^*}\left(\eta^*\frac{\partial u^*}{\partial r^*}+\left(\frac{h_e}{L}\right)^2\eta^*\frac{\partial v^*}{\partial z^*}\right), \tag{53}$$

$$\varepsilon\,\mathrm{Pr}\left(u^*\frac{\partial T^*}{\partial z^*}+v^*\frac{\partial T^*}{\partial r^*}\right)=\frac{1}{r^*}\frac{\partial}{\partial r^*}\left(r^*\frac{\partial T^*}{\partial r^*}\right)+2\,\mathrm{Ec}\,\mathrm{Pr}\left(\frac{h_e}{L}\right)^2\eta^*\left[\left(\frac{\partial u^*}{\partial z^*}\right)^2+\left(\frac{\partial v^*}{\partial r^*}\right)^2+\left(\frac{v^*}{r^*}\right)^2\right]$$
$$\mathrm{Ec}\,\mathrm{Pr}\,\eta^*\left[\frac{\partial u^*}{\partial r^*}+\frac{\partial v^*}{\partial z^*}\left(\frac{h_e}{L}\right)^2\right]^2, \tag{54}$$

$$\dot{V}^*=\int_{r_w^*}^{r_d^*} r^*u^*dr^*=const., \tag{55}$$

respectively. In this rescaled representation the relative magnitudes of the individual non-dimensional terms are determined by the prefactors occurring in front of them. The non-dimensional parameter occurring as prefactor of the advective transport terms on the lhs represents the so called reduced Reynolds number

$$\varepsilon=\mathrm{Re}_L\left(\frac{h_e}{L}\right)^2=\frac{\rho U_w L}{\eta_I}\left(\frac{h_e}{L}\right)^2. \tag{56}$$

Due to the very small aspect ratio $h_e/L<<1$ and the fact the Reynolds number based on the axial length of the die in general strongly exceeds unity (typical values are in the range $\mathrm{Re}_L\approx O(10^3)$, the definition (56) implies

$$\left(\frac{h_e}{L}\right)^2 << \varepsilon. \tag{57}$$

The advective and viscous dissipation terms in the energy equation (54) involve the Prandtl and the Eckert numbers defined as

$$\mathrm{Pr} = \frac{c_p \eta_I}{\lambda}, \tag{58}$$

$$\mathrm{Ec} = \frac{U_w^2}{c_p T_w}, \tag{59}$$

respectively. Analogously to the momentum transport a non-dimensional scaling parameter appears as prefactor of the advective term on the lhs of the thermal energy equation. It is defined as

$$\varepsilon_T = \varepsilon\,\mathrm{Pr} = \mathrm{Pr}\,\mathrm{Re}_L \left(\frac{h_e}{L}\right)^2, \tag{60}$$

and basically represents a reduced Pèclet number.

Due to Ec << Re_L, it follows

$$\mathrm{Ec}\,\mathrm{Pr}\left(\frac{h_e}{L}\right)^2 \ll \varepsilon_T. \tag{61}$$

Considering the relations (56) and (60) it becomes evident that the terms which are scaling with $(h_e/L)^2$, are much smaller than the terms scaling with ε or ε_T, respectively.
The solutions of the non-dimensionalized set of equations shall be assumed as series expansions written as

$$u^* = u_0^* + \varepsilon u_1^* + \varepsilon^2 u_2^* + \ldots, \tag{62}$$

$$v^* = v_0^* + \varepsilon v_1^* + \varepsilon^2 v_2^* + \ldots, \tag{63}$$

$$p^* = p_0^* + \varepsilon p_1^* + \varepsilon^2 p_2^* + \ldots, \tag{64}$$

$$T^* = T_0^* + \varepsilon_T T_1^* + \varepsilon_T^2 T_2^* + \ldots, \tag{65}$$

$$\eta^* = \eta_0^* + \varepsilon \eta_1^* + \varepsilon^2 \eta_2^* + \ldots \ . \tag{66}$$

Introducing these expressions into the non-dimensional form of the balance equations (52)-(55) it is possible to derive the constitutive equations for each individual order by equating all terms of the respective same order. Truncating the solutions at ε^2 and ε_T^2 the present work computes the zeroth-order solution and its first-order extension for Newtonian fluids.

3.2 Zeroth-order solution

The governing equations for the zeroth-order are derived by equating all terms of the order ε^0 and ε_T^0 in Eqs. (52)-(55). It can be seen that the zeroth-order formulation represents the approximation based on the lubrication theory assumption, where the convective and axial diffusive transports are neglected. The zeroth-order balance equations for momentum and heat read

$$\frac{\partial p_0^*}{\partial z^*} = \frac{1}{r^*} \frac{\partial}{\partial r^*} \left(\eta_0^* r^* \frac{\partial u_0^*}{\partial r^*} \right), \tag{67}$$

$$\frac{\partial p_0^*}{\partial r^*} = 0, \tag{68}$$

$$\frac{1}{r^*}\frac{\partial}{\partial r^*}\left(r^* \frac{\partial T_0^*}{\partial r^*} \right) = \mathrm{Ec}\,\mathrm{Pr}\,\eta_0^* \left(\frac{\partial u_0^*}{\partial r^*} \right)^2, \tag{69}$$

$$\dot{V}_0^* = \int_{r_w^*}^{r_d^*} r^* u_0^* \, dr^* = const. \tag{70}$$

At the radial inner and outer walls no-slip boundary conditions are imposed, while constant temperature and adiabatic wall conditions are prescribed for the energy, i.e.,

$$r^* = r^*_w : \quad u_0^* = 1, \; T_0^* = 1, \tag{71}$$

$$r^* = r^*_d : \quad u_0^* = 0, \; \frac{dT_0^*}{dr^*} = 0. \tag{72}$$

Ambient pressure is prescribed at the inlet of the die, such that

$$z^* = 0 : \quad p_0^* = 0. \tag{73}$$

Solving the continuity equation (70) for the unknown flow rate $\dot{V}_0^*$ requires an appropriate boundary condition for the pressure at the exit as well. This necessitates a closer look at the local flow conditions next to the exit, as schematically shown in Figure 20. In this exit region the flow shall be assumed as Couette flow, which is subject to a certain axial pressure gradient arising from the capillary pressure inside the curved liquid meniscus $p_\sigma \sim \sigma / R_c$.

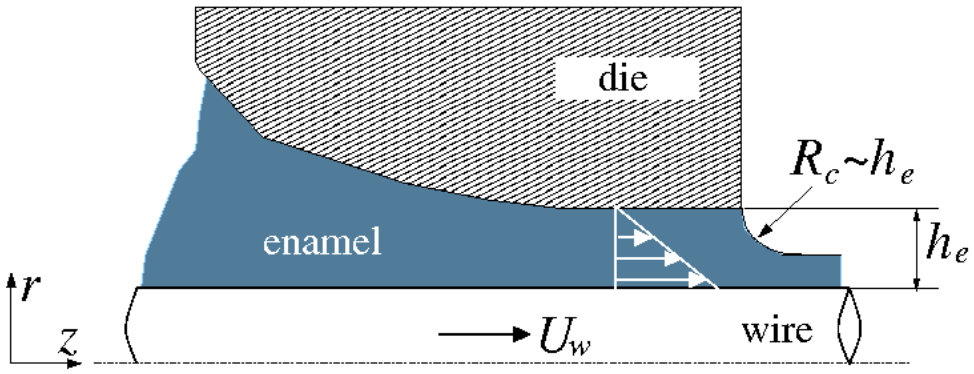

Figure 20: Flow condition at the die exit

Assuming for simplicity planar flow, the flow rate at the die exit can be computed as

$$\dot{V} = U_w \frac{h_e}{2} - \left.\frac{dp}{dz}\right|_e \frac{h_e^3}{12\eta}. \tag{74}$$

Assuming the exit gap height as length scale h_e for the surface curvature radius R_c as well as for the local streamwise pressure variation the pressure gradient can be estimated as

$$\left.\frac{dp}{dz}\right|_e = \frac{\sigma}{h_e^2}. \tag{75}$$

Introducing this estimate for the pressure gradient into the Eq. (74) yields

$$\dot{V} = U_w \frac{h_e}{2}\left(1 - \frac{1}{6\,Ca}\right). \tag{76}$$

Eq. (76) involves the capillary number, which basically represents the ratio between the viscous forces and surface tension and is defined as

$$Ca = \frac{U_w \eta}{\sigma}, \tag{77}$$

where σ denotes the surface tension and η denotes the local value of viscosity. The contribution of the capillary pressure at the exit is evidently determined by the magnitude of the capillary number. As will be shown in the discussion of the computationally investigated flow cases in section 3.2.3, the relevant capillary number is always sufficiently large, so that the effect of the capillary pressure can be neglected. Thus, the ambient pressure can be imposed at the exit boundary as well, i.e.,

$$z^* = 1: \quad p_0{}^* = 0. \tag{78}$$

The radial integration of the non-dimensional form of the axial momentum equation yields the following expression for the axial velocity

$$u_0{}^* = \frac{dp_0{}^*}{dz^*}\left[I\left(z^*, r^*\right) - \frac{I\left(z^*, r_d{}^*\right)}{II\left(z^*, r_d{}^*\right)} II\left(z^*, r^*\right) \right] - \frac{II\left(z^*, r^*\right)}{II\left(z^*, r_d{}^*\right)} + 1, \tag{79}$$

where *I* and *II* represent the definite integrals

$$I\left(z^*, r^*\right) = \int_{r_w{}^*}^{r^*} \frac{\zeta^*}{2\eta^*} d\zeta^*, \; II\left(z^*, r^*\right) = \int_{r_w{}^*}^{r^*} \frac{d\zeta^*}{\zeta^* \eta^*}, \tag{80}$$

respectively. The expression for the velocity given by Eq. (79) still contains the yet unknown axial pressure gradient. The axial pressure gradient is obtained by substituting the axial velocity (79) into the equation of continuity (70), which yields

$$\frac{dp_0^*}{dz^*} = \frac{\dot{V}_0^* + \int_{r_w^*}^{r_d^*} r^* \left[\frac{II\left(z^*, r^*\right)}{II\left(z^*, r_d^*\right)} - 1 \right] dr^*}{\int_{r_w^*}^{r_d^*} r^* \left[I\left(z^*, r^*\right) - \frac{I\left(z^*, r_d^*\right)}{II\left(z^*, r_d^*\right)} II\left(z^*, r^*\right) \right] dr^*}. \tag{81}$$

The flow rate $\dot{V}_0^*$ is iteratively obtained by integrating (81) into the axial direction until the pressure boundary conditions at the inlet and the exit are satisfied.

Analogously to the solution of the momentum equation, the radial integration of the energy equation given by Eq. (69) yields the following non-dimensional expression for the temperature:

$$T_0^* = -IV\left(r^*\right) + IV\left(r_d^*\right) \frac{\ln r^*}{\ln r_w^*} + 1. \tag{82}$$

Therein, *IV* represents the integral

$$IV\left(r^*\right) = \int_{r_w^*}^{r^*} \frac{III\left(\varphi^*\right)}{\varphi^*} d\varphi^* \quad \text{with} \quad III\left(\varphi^*\right) = \mathrm{Ec}\,\mathrm{Pr} \int_{r_w^*}^{\varphi^*} \dot{\gamma}^{*2} \eta^* \zeta^* d\zeta^*, \quad r_w^* \le \varphi^* \le r^*. \tag{83}$$

For non-Newtonian fluids the dependence of the viscosity on the shear rate impedes an analytical evaluation of the integrals occurring in (80) and (83). This is only possible for Newtonian fluids, as will be shown in the following subsection.

3.2.1 Newtonian fluid model

Considering Newtonian flow behavior implies that the viscosity of the fluid does not vary with the shear rate, such that $\eta = \eta_I = const.$ Furthermore, excluding any dependence of the viscosity on

the temperature as well, its non-dimensional representation becomes $\eta_0^*=1$. Assuming unity for non-dimensional viscosity, the integrals occurring in Eqs. (80) and (83) can be evaluated analytically. Which finally yields an analytical expression for the velocity written as

$$u_0^* = \frac{\ln\left(r_d^*/r^*\right)+\frac{1}{4}\frac{dp_0^*}{dz^*}\left[r^{*2}\ln\left(r_d^*/r_w^*\right)+r_d^{*2}\ln\left(r_w^*/r^*\right)+r_w^{*2}\ln\left(r^*/r_d^*\right)\right]}{\ln\left(r_d^*/r_w^*\right)}, \tag{84}$$

where the axial pressure gradient, obtained from Eq. (81), is rewritten as

$$\frac{dp_0^*}{dz^*} = \frac{\frac{1}{2}\left(\frac{r_d^{*2}-r_w^{*2}}{2\ln\left(r_d^*/r_w^*\right)}\right)-\dot{V}_0^*}{\frac{1}{16}\left(r_d^{*4}-r_w^{*4}+\frac{\left(r_d^{*2}-r_w^{*2}\right)^2}{\ln\left(r_d^*/r_w^*\right)}\right)}. \tag{85}$$

Upon substitution of the upper radial contour $r=r_d^*(z^*)$ of the considered die shape this expression is successively integrated in an iterative procedure to obtain the flow rate $\dot{V}_0^*$, for which the pressure boundary conditions (73) and (78) are satisfied. Using the analytically obtained expressions for the integrals *III* and *IV* occurring in Eq. (82) the temperature is rewritten as

$$T_0^* = \frac{\mathrm{Br}\left(\frac{dp_0^*}{dz^*}\right)^2\left(r_w^{*4}-r^{*4}\right)}{64} - \frac{\mathrm{Br}\left[4+\frac{dp_0^*}{dz^*}\left(r_w^{*4}-r^{*4}\right)\right]^2 \ln\left(r_d^*/r_w^*\right)^2}{32\ln\left(r_d^*/r_w^*\right)^2} -$$
$$- \frac{\mathrm{Br}\frac{dp_0^*}{dz^*}\left(r^{*2}-r_w^{*2}\right)\left[-4+\frac{dp_0^*}{dz^*}\left(r_w^{*2}-r_d^{*2}\right)\right]}{16\ln\left(r_d^*/r_w^*\right)} + \frac{r_d^{*4}\mathrm{Br}\left(\frac{dp_0^*}{dz^*}\right)^2 \ln\left(r_d^*/r_w^*\right)}{16} + \tag{86}$$
$$\frac{2r_d^*\mathrm{Br}\frac{dp_0^*}{dz^*}r_d^*\ln\left(r_d^*/r_w^*\right)\left\{\left[-4+\frac{dp_0^*}{dz^*}\left(r_w^{*2}-r_d^{*2}\right)\right]+\left[-4+\frac{dp_0^*}{dz^*}\left(r_w^{*2}-r_d^{*2}\right)\right]\right\}}{16\ln\left(r_d^*/r_w^*\right)} + 1.$$

3.2.2 Non-Newtonian fluid model

Since the presently derived computational model shall be applicable to real-life wire coating conditions, non-Newtonian flow behavior typically met with most enamels has to be considered. A non-Newtonian fluid model has therefore been introduced into the zeroth-order solution. As already presented in the section 2.2.1.1, there exists a large variety of models that describe the shear rate dependent behavior of non-Newtonian fluids. For the considered enamel, which is a polymer solution the Carreau-Yasuda model, as given in Barnes et al. 1989, appears as a very convenient approach. It is written as

$$\eta^* = \frac{\eta(\dot{\gamma})}{\eta_I} = \left(1-\frac{\eta_{II}}{\eta_I}\right)\left[1+\left(K_1\,\dot{\gamma}\frac{h_e}{U_w}\right)^2\right]^{-m_{1/2}} + \frac{\eta_{II}}{\eta_I}. \tag{87}$$

The model parameters K_1 and $m_{1/2}$ determine the transition between the first and the second Newtonian plateau, which are reached in the limits of zero shear rate, $\dot{\gamma} \to 0$, $\eta \to \eta_I$, and infinite shear rate, $\dot{\gamma} \to \infty$, $\eta \to \eta_{II}$, respectively. A typical flow curve for a shear thinning fluid is exemplarily shown in Figure 21. The model parameters have been set to K_1 =1.74x10^{-5} s and

$m_{1/2}$ =0.4, such that the flow curve fits best the available experimental data which are denoted by the symbols. The experimental data were measured for the enamel "Terebec 533-45" with a solid polymer mass fraction 45%, which corresponds to a volume fraction 39%, using a rotational viscosimeter. It is noted that the region of very high shear rates, where the flow curve is plotted as dashed line, is not accessible to available standard rheometers. The level of the second Newtonian plateau had therefore to be assumed due to the lack of experimental data.

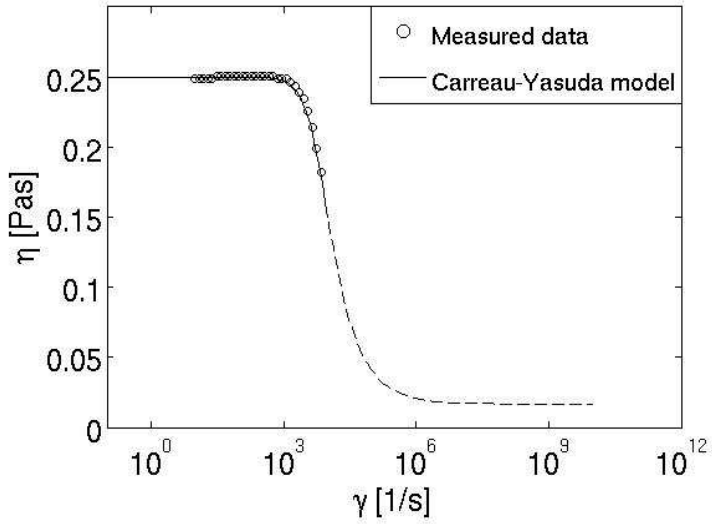

Figure 21: Flow curve of a typical wire enamel (Terebec 533-45)

The dependence of the viscosity of the shear rate, $\eta^* = \eta^*(\dot{\gamma}^*)$ with $\dot{\gamma}^* = \dot{\gamma}^*(z^*, r^*)$, allows only for a numerical evaluation of the integrals defined in Eqs. (80) and (83). As a consequence, the governing set of equations has to be solved iteratively with the local shear rate $\dot{\gamma}^*$as the basic unknown. The iterative solution procedure is briefly outlined below:

1) An initial solution is computed assuming a Newtonian fluid with $\eta = \eta_I = const.$ setting η^*=1
2) Based on the actually obtained flow field at iteration step (*n*) the shear rate at the new level (*n+1*), i.e., $\dot{\gamma}^*_{(n+1)}$, is computed from the implicit equation

$$\tau_{rz}^{*}=\eta^{*}\left(\dot{\gamma}_{(n+1)}^{*}\right)\ \dot{\gamma}_{(n+1)}^{*}=\left\{\frac{dp^{*}/dz^{*}\left[r^{*2}/2\ II\left(z^{*},r_{d}^{\ *}\right)-I\left(z^{*},r_{d}^{\ *}\right)\right]-1}{r^{*}II\left(z^{*},r_{d}^{\ *}\right)}\right\}_{(n)},$$

where $\eta^{*}\left(\dot{\gamma}_{(n+1)}^{*}\right)$ is substituted as defined in the flow model Eq. (87).

3) The flow field at the new level (n+1) is recomputed using the updated shear rate $\dot{\gamma}_{(n+1)}^{*}$ for the viscosity $\eta^{*}\left(\dot{\gamma}_{(n+1)}^{*}\right)$
4) Steps 2) and 3) are repeated until the solution for the whole $\dot{\gamma}^{*}$- field has converged, i.e., $\dot{\gamma}_{(n+1)}^{*}$-$\dot{\gamma}_{(n)}^{*}$<0.001
5) The velocity field is evaluated from Eq. (79) using the converged viscosity $\eta^{*}(\dot{\gamma}^{*})$ in the integrals *I* and *II*.

Apart from the shear rate dependent behavior of the viscosity of the fluid, the computational model was additionally extended to account for a possible dependence of the viscosity on the temperature. The temperature dependence was incorporated by reducing the values of the viscosity for the first Newtonian plateau (zero shear viscosity) to lower levels for increasing temperature. The dependence of the zero shear viscosity of the temperature was assumed as Vogel equation written as

$$\eta_{I}\left(T\right)=A\exp\left(\frac{B}{T-C}\right) \tag{88}$$

involving the model parameters A, B and C.

3.2.3 Test cases

The test case conditions considered in the present computations of the zeroth-order solution were specified very close to real enameling conditions of thin copper wires. Accordingly, the diameter of the wire was set to d_0=0.15 mm, and the velocity of the wire was set to a typically high value for thin wires U_w=22.3 m/s. The length of the die is L=25 mm, and the gap height at the exit is h_e=5 μm. The difference in gap height between the die inlet and exit was assumed δ=2.5 mm. Based on this parameter setting the local value of the reduced Reynolds number, analogously to Eq. (40) defined as $\widetilde{\mathrm{Re}} = \frac{\rho U_w L}{\eta_I}\left(\frac{h}{L}\right)^2$, varies between $\widetilde{\mathrm{Re}}$ = 8.9 at the die inlet, where $h = h_0 + \delta$, and $\widetilde{\mathrm{Re}} = \varepsilon = 8.91\text{x}10^{-5}$ at the outlet, where $h = h_e$. Although this value exceeds unity near the inlet, the assumption of the lubrication theory approximation still provides reasonable predictions for the velocity field even in the entrance region, as it will be shown below in the discussion of the results.

The effect of the shape of the die was examined by varying the axial contraction assuming a cosine-type variation of the radially outer contour generally written as

$$r_d^* = \frac{r_d}{h_e} = \frac{r_w}{h_e} + 1 + \frac{\delta}{2h_e}\left[1 + \cos\left(\pi\left(\frac{z}{L}\right)^{n_{geo}}\right)\right]. \qquad (89)$$

As shown in Figure 22 the prescription of the geometrical parameter n_{geo} determines the shape of contour. For the low values of the parameter, the geometrical outline becomes purely convex, while by increasing its value it changes towards concave shapes, finally ending in step like change in the geometry as the values of the geometrical parameter tend to infinity. The functional dependence (89) provides by definition a zero gradient at the exit, i.e., dr_d^*/dz^*=0, which follows from a specific requirement of the real enameling process.

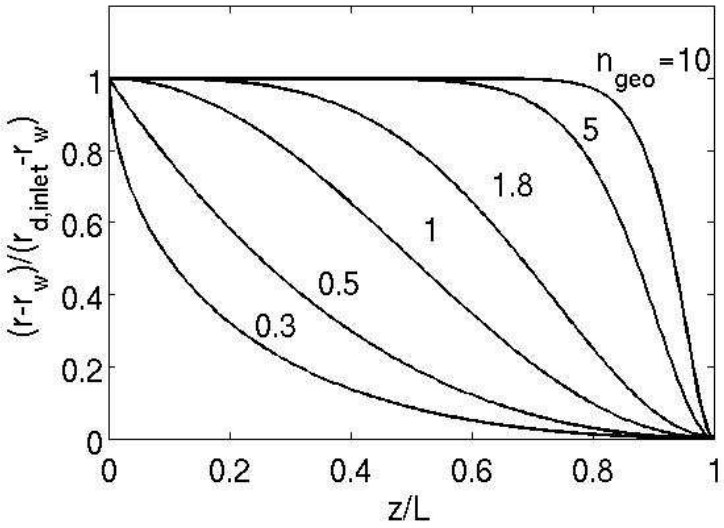

Figure 22: Die contours for different values of exponent n_{geo}

The presently computed cases are essentially distinguished by the flow behavior of the fluid. They are all listed in Table 4.

Table 4: Computational cases; parameters for non-Newtonian fluids according to Eq. (87)

Case								
1	Newtonian		Isothermal		η [Pas] = η_I = 0.25 = *const.*			
					η_I [Pas]	η_{II} [Pas]	K_1x10^5 [s]	$m_{1/2}$ [-]
2	Non-Newtonian	Shear thinning	Isothermal		0.25	0.0167	1.74	0.3
3	Non-Newtonian	Shear thinning	Non-isothermal	at T_{ref} = 333.15 K	0.25	0.0167	1.74	0.3
4	Non-Newtonian	Shear thickening	Isothermal		0.25	3.75	1.74	0.3

Case 1 represents a reference base case considering Newtonian fluid behavior with constant dynamic viscosity independent of both shear rate and temperature. The dynamic viscosity of this base case is assumed as η=0.25 Pas, which corresponds to the measured first Newtonian plateau

of the enamel “Terebec 533-45” with 45% solid mass fraction. This value is also assumed as the zero-shear rate viscosity η_I for all non-Newtonian cases. The viscosities of the first and second Newtonian plateau always differ by roughly one order of magnitude.

Case 3 essentially considers the same shear thinning fluid as Case 2, but it additionally assumes a dependence of the viscosity on the temperature described by the Vogel equation (89) with the model parameters set to A=0.003906 Pas, B=414 K, and C=234 K. The thermal conductivity and heat capacity required for the solution of the heat transfer equation were set to λ=0.5 W/mK and c_p =10 J/kgK, respectively. Using the value of the first Newtonian plateau η_I as reference viscosity this translates into Prandtl and Eckert numbers Pr=5, and Ec=0.14, respectively.

The surface tension is assumed as σ=0.06 N/m, which represents a typical value for wire enamels. Based on this setting and the viscosity of the second Newtonian plateau the capillary number defined in Eq. (77) is at minimum in the shear thinning cases 2 and 3, being Ca=6.21. As seen from Eq. (76), this value is still sufficiently high to justify the neglect of the capillary pressure at the exit of the die.

3.2.4 Results

A wide range of the geometrical parameter n_{geo} was considered to evaluate the accuracy of the zeroth-order solution obtained for very different geometrical outlines, as well as to investigate the influence of the change in die shape on the flow and temperature fields. The computed range extends from n_{geo}=0.3, describing a fully convex geometrical outline, to n_{geo}=50, describing a fully concave geometry of the die.

Detailed zeroth-order results of the flow field and heat transfer are discussed in the following only for the geometrical parameter n_{geo}=1.8, because this case is well representative for the geometries commonly met in the application. Moreover, the basic structure of the flow and temperature fields showed qualitatively no substantial differences for the other considered values of n_{geo}, which would require any particular analysis.

3.2.4.1 Flow field

Figure 23 gives a qualitative insight into the structure of flow field showing the contours of the streamwise velocity component obtained for the Newtonian fluid. The flow field can be evidently split into two sub-regions. The radially inner sub-region near the wire is associated with a positive axial velocity, where the flow is driven by the viscous entrainment of liquid due the motion of the wire. The radially outer sub-region is characterized by reverse flow, carrying excess enamel out of the die. The resulting considerable ejection of excess enamel from the inlet is typically observed in the real application as well.

The rheological behavior of the fluid notably affects the shape of the velocity profile, as seen from Figure 24 showing the radial variations of the streamwise velocity component at different axial positions. The results at the inlet, $z/L=0$, and half-way downstream, $z/L=0.5$, shown in Figures 24 (a) and (b), respectively, indicate that the shear thinning behavior of the fluid leads to a certain flattening of the velocity profile in the backflow region. This effect is most significant in the shear thinning non-isothermal case 3, where the viscosity is additionally reduced as the temperature is increased by viscous heating. An opposite effect on the velocity can be observed in the case of the shear thickening fluid, where the profile is steeper as compared to the Newtonian reference case. At the exit cross-section shown in Figure 24 (c) the profile of the shear-thinning isothermal case somewhat exceeds the others, which implies a higher volumetric flow rate exiting the die at the outlet cross-section. The differences observed in Figure 24 (c) give also insight into the interaction between the pressure and the viscous forces governing the generalized Couette-flow. For the shear-thinning isothermal case the favorable pressure gradient occurring at the exit evidently increases most effectively the flow rate relative to the purely shear-driven contribution entrained by the moving wire. Accordingly, case 2 exhibits the bulkiest profile at $z/L=1$.

The differences in the shape of the velocity profiles observed in Figures 24 (a) and (b) also translate into different radial extensions of the backflow regions. Figure 25 shows the contour lines of zero axial velocity $u^*=0$, which separate the regions of forward and reverse flow. It is clearly seen that shear thinning leads to a broader while shear thickening leads to a narrower

backflow region. The axial extensions of the backflow region do not differ significantly, as indicated by the intersection of the contour lines with the upper wall contour shown in the zoomed detail in Figure 25.

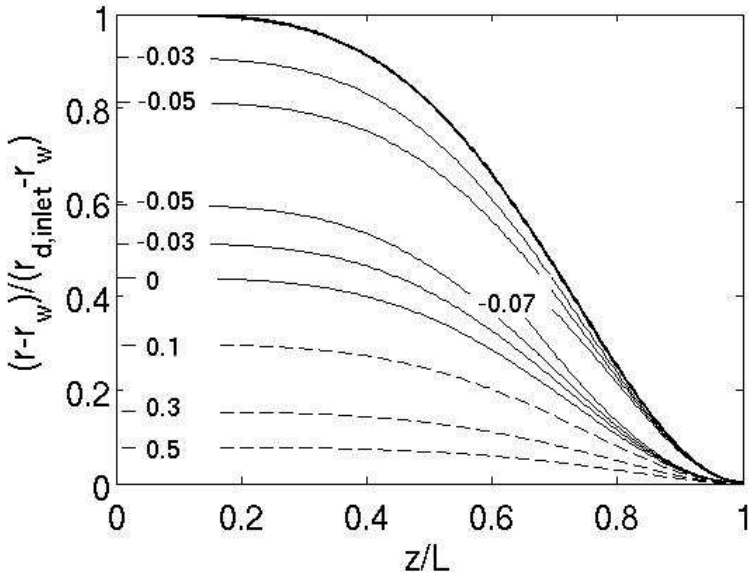

Figure 23: Contours of the streamwise velocity component u^* for Newtonian fluid (Case 1); n_{geo}=1.8; solid contours denote $u^* \leq 0$, dashed contours denote $u^* > 0$

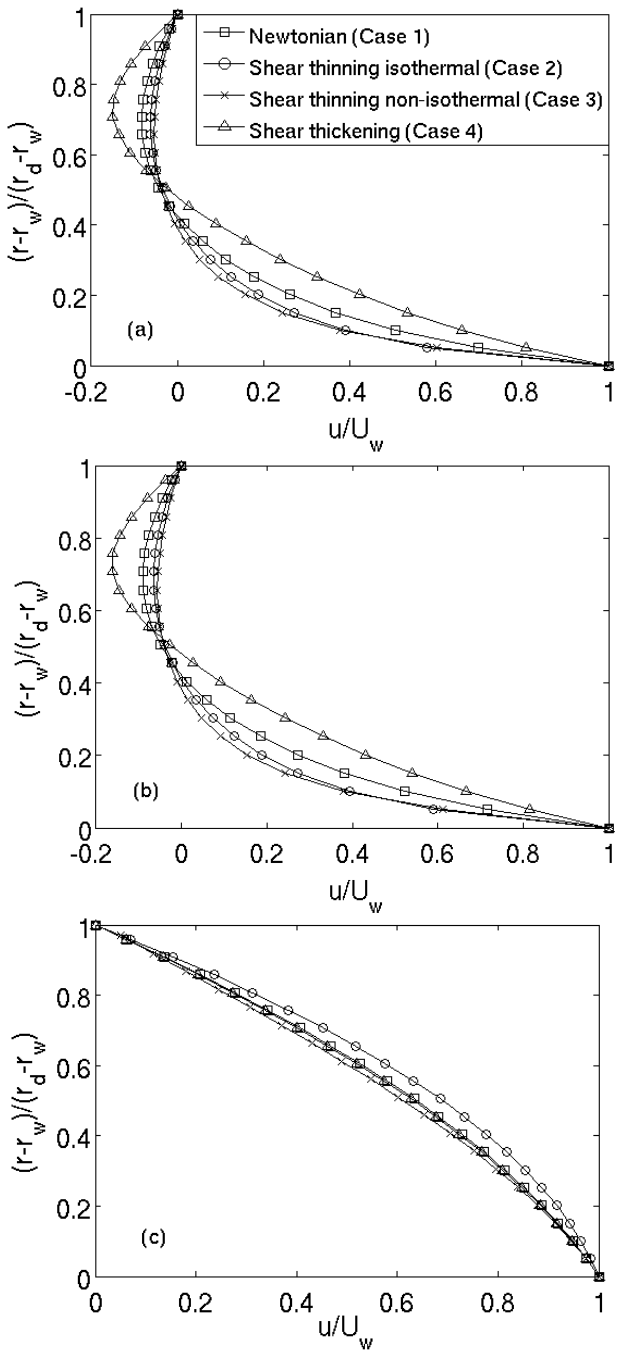

Figure 24: Velocity profiles at different streamwise positions for n_{geo}=1.8: (a) *z/L*=0, (b) *z/L*=0.5, (c) *z/L*=1

Table 5 lists the volumetric flow rates exiting the die at the outlet cross-section $\dot{V}^*_{out}$ together with volumetric flow rates exiting the die with the backflow at the inlet $\dot{V}^*_{backflow}$. As already indicated by the close velocity profiles at the outlet, the differences in the flow rates at the outlet are fairly small. In contrast, the amount of enamel which is ejected upstream at the inlet cross-section is considerably decreased for the shear thinning fluids and significantly increased for the shear thickening fluid as compared to the Newtonian reference case. Due to the very small exit gap height it is conceivable that only a very small fraction of the fluid, which is entrained at the inlet, passes the outlet coating the wire. Most part of the entrained liquid is redirected and leaves the die as backflow at the inlet. This reverse motion gets evidently enhanced for the shear thickening fluid.

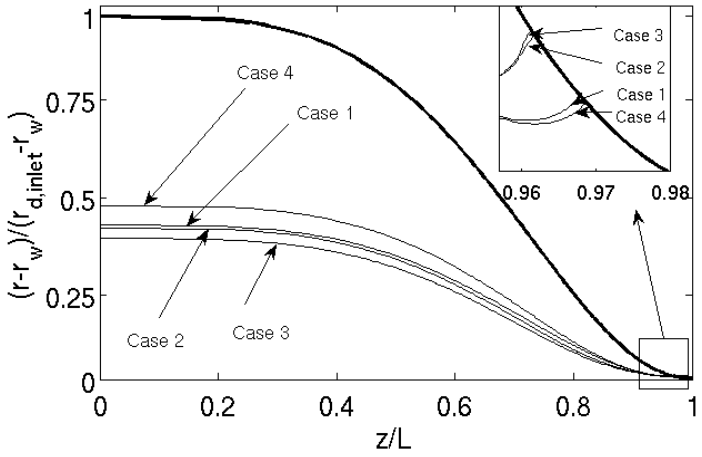

Figure 25: Contours of zero velocity u^*=0 separating forward flow and backflow regions

Table 5: Flow rates at die outlet and backflow flow rates

	Newtonian (Case 1)	Shear thinning isothermal (Case 2)	Shear thinning non-isothermal (Case 3)	Shear thickening (Case 4)
$\dot{V}^*_{out}$	0.0410	0.0434	0.0395	0.0407
$\dot{V}^*_{backflow}$	4.6239	3.4865	3.1224	7.5124
$\dot{V}^*_{out} / \dot{V}^*_{backflow}$ [%]	0.87	1.24	1.27	0.54

A most significant influence of the rheological flow behavior can be observed in the variation of the wall shear stress along the wire displayed in Figure 26. Since the shear rate at the wall is always below zero, the wall shear stress is always negative as well. It is plotted with negative sign, which implies the higher the shown ordinate value the more it contributes to the total drag force F_d obtained as

$$F_d = -2\pi L U_w \eta_I \int_0^1 \tau_w^* dz^* \ . \tag{90}$$

Relating this quantity to then cross-sectional area of the wire A_w yields the corresponding tensile stress exerted on the wire written as

$$\sigma_{wire} = \frac{F_d}{A_{wire}}. \tag{91}$$

All curves exhibit a characteristic peak closely upstream of the axial end of the backflow region shown in the zoomed detail of Figure 26. As expected the increase in viscosity due to shear thickening leads to the highest peak level, while the decrease in viscosity due to shear thinning and the raise in temperature (shear thinning non-isothermal case 3) leads to the lowest level for $-\tau_w^*$. Since the momentum balance is basically governed by the pressure and the viscous forces, the streamwise variation of the wall shear stress is reflected in the variation of pressure, as depicted in Figure 27. The peak is highest for shear thickening and lowest for the shear thinning non-isothermal case. The axial position of the peak is close to the exit, and it does not differ notably for the considered cases, very similar the shear stress. The peak in the pressure also denotes the position, where the curvature of the axial velocity profile changes from positive near the inlet to negative near the exit. The different curvature can also be seen in the profiles already shown in Figures 24 (a)-(c).

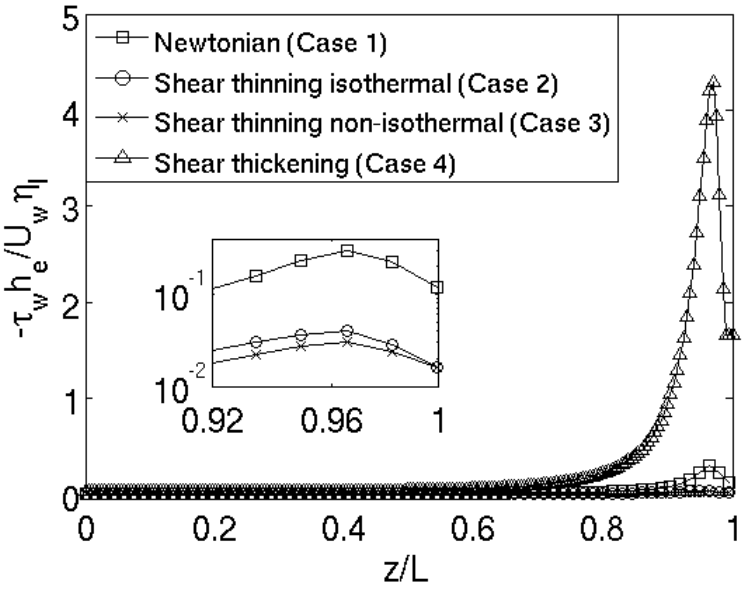

Figure 26: Variation of wall shear stress along the wire; n_{geo}=1.8

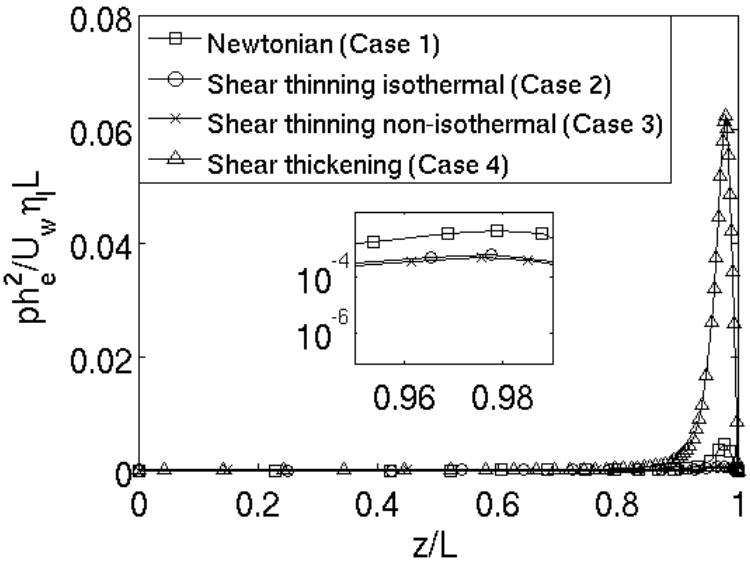

Figure 27: Variation of the pressure along the wire; n_{geo}=1.8

3.2.4.2 Heat transfer

In the shear thinning non-isothermal case 3 heat transfer is included by solving the energy equation as given by Eq. (69). Figure 28 shows radial variations of the temperature at three selected axial positions, analogously to the velocity profiles presented in Figure 24. The solution for the Newtonian case 1 computed from Eq. (86) is displayed as well, representing a reference case with constant material properties. The increase in temperature caused by the viscous heating is well visible, but it is markedly less pronounced for the non-Newtonian fluid. The decrease in viscosity with both increasing shear rate and temperature effectively reduces the generation of viscous heat appearing as source term $\phi^*_{visc,0} = \mathrm{Ec}\,\mathrm{Pr}\,\eta_0^*\left(\partial u_0^*/\partial r^*\right)^2$ on rhs of Eq. (69).

Figure 29 shows the streamwise variation of the heat flux at the moving wire. It is always negative in sign for the Newtonian case as well as for the non-isothermal shear thinning case which simply follows from a global balance of internal energy. Due to the neglect of convective transport and the adiabatic outer radial boundary condition the viscous heat generated inside the enamel is completely transferred into the wire. This heat flux into the wire is markedly smaller for the shear thinning case due to the already mentioned lower production of viscous heat. The curves obtained for the heat flux essentially follow the trend of the momentum flux represented by the wall shear stress shown in Figure 26. As such they remain on an almost constant level for a large section near the inlet, and they exhibit an extremum near the exit.

Despite the intense local heat flux into the wire induced by the strong viscous dissipation (the non-dimensional peak value shown in Figure 29 corresponds to more than q_w=2x10^7 W/m^2), its potential to heat up of the wire is still very small. Table 6 shows the total heat transferred into the wire, written as

$$Q_w = \int_0^L q_w d_w \pi \, dz \tag{92}$$

and the corresponding potential increase in the temperature of the wire on its way through the die computed as

$$\Delta T_w = \frac{Q_w}{c_{p,w}\rho_w U_w d_w^2 \pi / 4}, \tag{93}$$

assuming for $c_{p,w}$ and ρ_w material properties of copper. The very small heated surface combined with the very short residence time evidently allow only for an insignificant increase in wire temperature. Therefore despite the very intense generation of viscous heat no particular previsions are required in order to impede a possible undesirable heat up of the enamel as well as the surrounding material. This holds true for the Newtonian as well as the non-Newtonian fluids.

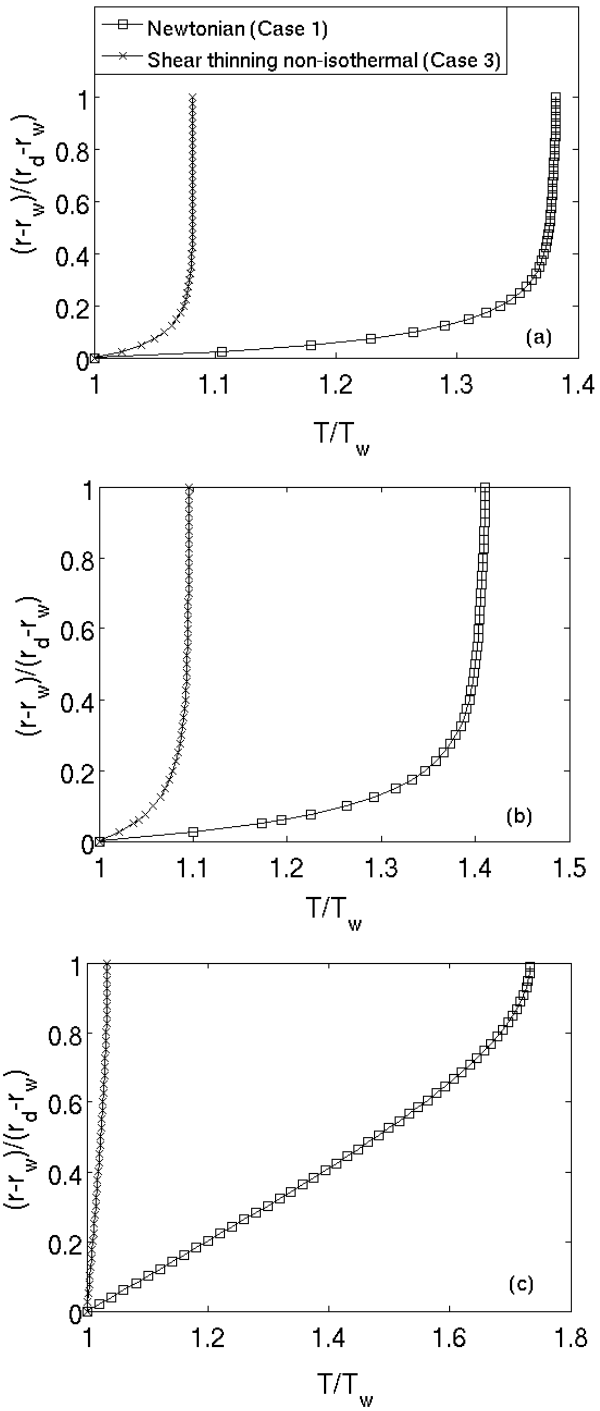

Figure 28: Temperature profiles at different streamwise positions for n_{geo}=1.8: (a) z/L=0, (b) z/L=0.5, (c) z/L=1

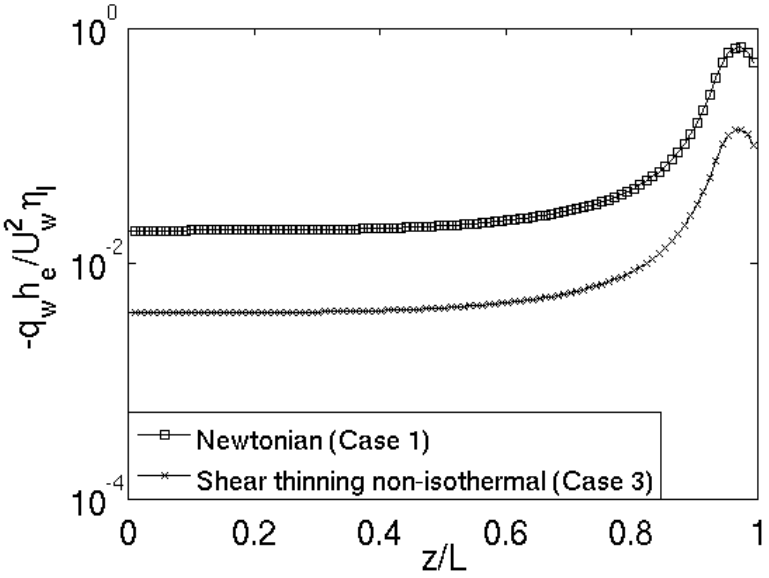

Figure 29: Heat flux along the wire; n_{geo}=1.8

Table 6: Total heat flux into the wire and corresponding potential change in wire temperature; n_{geo}=1.8

	Newtonian (Case 1)	Shear thinning non-isothermal (Case 3)
Q_w [W]	2.64	1.94
ΔT_w [K]	1.76	1.44

3.2.5 Evaluation against numerical results

The numerical approach generally termed “Computational Fluid Dynamics” (CFD) solves numerically the discretized representation of the full set of transport equations. As such it is in general computationally far more expensive than the analytical approach. Since there are practically no experimental data available on the flow field inside enameling dies, CFD simulations basically represent the only reliable approach to provide comprehensive data for validation. The used CFD setup will be explained in detail in the following section.

3.2.5.1 CFD setup

The problem of wire coating basically represents a two phase problem involving gas-liquid interfaces between the ambient air and the initial dip coat deposited upstream of the die, and the thin final coat exiting the die. Considering nonetheless the flow inside the die as purely single-phase requires some justification for excluding a possible two-phase flow situation as schematically shown in Figure 30.

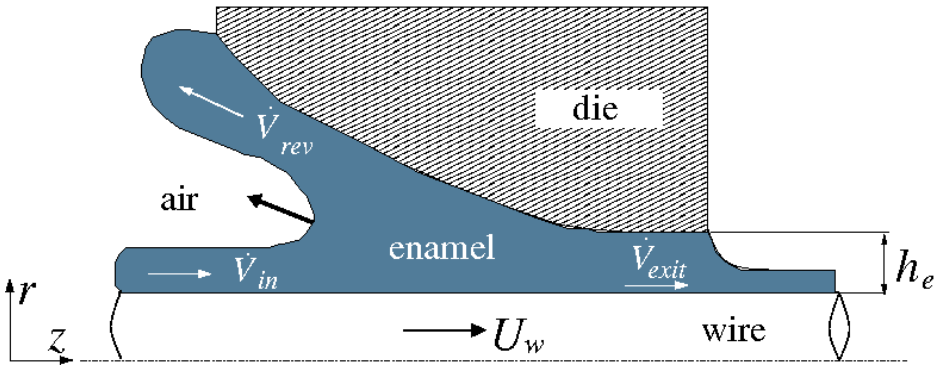

Figure 30: Possible two-phase flow situation inside the die

Therein, $\dot{V}_{in}$ represents the incoming volumetric flow of enamel which has been deposited on the wire in the dip coating step. Inside the die this incoming amount of enamel per time unit is split into two branches. $\dot{V}_{exit}$ represents the amount of enamel which exits the die at the outlet with a very small deposition height determined by the exit gap height of the die. $\dot{V}_{rev} >> \dot{V}_{exit}$ represents

the much larger amount of enamel directed back towards the die inlet due to the axially converging geometry of the gap. Sustaining the conditions shown in Figure 30 would require a stable balance of forces on the liquid and the air side of the meniscus inside the die. Introducing estimates for the capillary and viscous pressure forces on the liquid side, and for the dynamic pressure on the air side this balance would require

$$\frac{\sigma}{h}+\eta\frac{U_w}{h}\approx\rho_{air}\frac{U_w^2}{2}. \tag{94}$$

Rescaling into a non-dimensional representation

$$\frac{\sigma}{U_w h}+1\approx\rho_{air}\frac{U_w h}{\eta} \tag{95}$$

makes evident that the equality stated in (94) does not hold, as the rhs, which can be rewritten as

$$\frac{\rho_{air}}{\rho}\frac{\rho U_w L}{\eta}\left(\frac{h}{L}\right)\ll 1$$

is well below unity due to the small density and aspect ratios. Hence, the die can be assumed as completely occupied by the liquid, which allows for a pure single-phase consideration of the flow inside.

Figure 31 shows the computational domain used for the single phase simulations, indicating the individual boundaries. The flow was assumed as steady and axisymmetric. The wall boundary conditions strictly follow the analytical model. Accordingly, no-slip conditions were imposed at the inner and the outer radial boundary of the domain, while for the temperature a constant value boundary condition was set at the moving wall, and an adiabatic boundary condition was set at the outer radial wall. As can be seen from Figure 31, the computational domain is extended

upstream of z=0 by a short cylindrical section. The attachment of this short cylinder of 10% length of the die allows for some axial development of the Couette-type flow in order to provide flow conditions at z=0, which are well comparable with the inlet conditions of the computations with the lubrication theory based analytical model. Uniform ambient pressure $p=p_0$ and reference temperature $T=T_w$ were prescribed at the inlet and the outlet of the computational domain, respectively. Although the temperature is not constant at the exit, imposing a constant temperature does not have any significant effect on the temperature field inside the domain, as it will be seen in the discussion of the results. This insensitivity can be attributed to the negligibly small effect of heat conduction in the axial direction and to the only outgoing flow at the die exit. The non-Newtonian rheological behavior as described by Eq. (87), where $\dot{\gamma} = \partial u/\partial r$ (due to $\partial v/\partial z << \partial u/\partial r$), was implemented with User Defined Functions (UDFs), as well as the additional temperature dependency given by Eq. (88). The total size of the computational mesh was about 40000 cells for all considered cases.

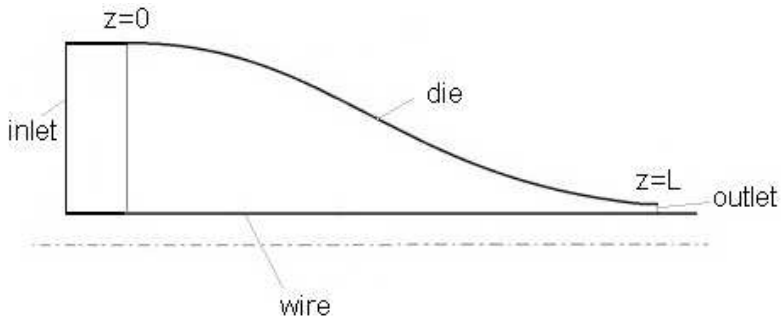

Figure 31: Computational domain and boundary conditions of the numerical CFD model

3.2.5.2 Assessment of analytically predicted momentum and heat transfer

The shear thinning non-isothermal case 3, assuming a geometry associated with the parameter n_{geo}=1.8 as die shape, was selected as validation case. This case particularly challenges the analytical model due to the coupling of the flow field with the temperature field through the dependence of the viscosity of both the shear rate and temperature. Both dependencies expectedly lead to the most pronounced reduction of the local viscosity below the reference value, which basically might increase the local values of the reduced Reynolds number $\widetilde{\mathrm{Re}} = \frac{\rho U_w L}{\eta_I}\left(\frac{h}{L}\right)^2$, jeopardizing the assumption of the lubrication theory to neglect all convective transports. On the other hand, it has to be noted that this decrease in the local viscosity, which can result into a reduction by a factor 10 with respect to the reference value, mainly occurs in the highly sheared region near the exit of the die. Due to the small gap heights ($h<<L$) met in this region, the local reduced Reynolds number does effectively not exceed unity there.

In Figure 32 the analytically obtained zeroth-order predictions for the flow field are assessed by comparing the radial profiles of the velocity at selected streamwise positions, analogously to Figure 24. The agreement is very good at all shown positions, which indicates that the inertia terms remain negligibly small despite the substantial decrease of the local viscosity due to shear thinning and increase in temperature. The good agreement observed for the velocity profiles is also reflected by the accordance of the streamwise variations of the wall shear stress shown in Figure 33.

Some considerable disagreement appears in the zeroth-order predictions for the temperature near the entrance and in the middle region of the die, as seen from the temperature profiles in Figure 34. As compared to the balance of momentum, where the advective transport scales with the reduced Reynolds number ε, the advective transport in the energy balance scales with the reduced Pèclet number $\varepsilon_T = \varepsilon \mathrm{Pr}$ which is for the considered parameter setting for Pr, 5 times higher than ε. Thus, the neglect of the advective transport in the energy balance has evidently a more pronounced effect in the region of the reversed flow. As indicated by the good agreement of the velocity profiles shown in Figure 32, the strain field is predicted very well, so that a

significantly different predicted generation of viscous heat can be ruled out as most relevant reason for the observed discrepancy in temperature. The disagreement of the temperature profiles between the analytical and numerical solution have therefore rather to be attributed to the way, how the generated viscous heat is distributed inside the domain. The zeroth-order solution provides radial heat conduction as the only available heat transfer mechanism. This limitation evidently leads to markedly increased temperature levels near the adiabatic outer wall. As seen from Figure 35, generally higher predicted temperatures also lead to an increased heat flux into the wire as compared to the numerical solution.

The analytical zeroth-order has been further examined for its accuracy in predicting the total drag force on the wire considering very different geometries as determined by the parameter n_{geo}=1.8, 10, and 20. The obtained results are summarized in Table 7 showing only small discrepancies to the numerical results of CFD. Based on this assessment the zeroth-order model appears as a reliable and computationally efficient approach for developing flow optimized die geometries. This will be demonstrated in the next section putting the focus the on the possible reduction in the drag force exerted on the wire which can be achieved by a variation of the converging geometry of the die for different rheological flow behavior.

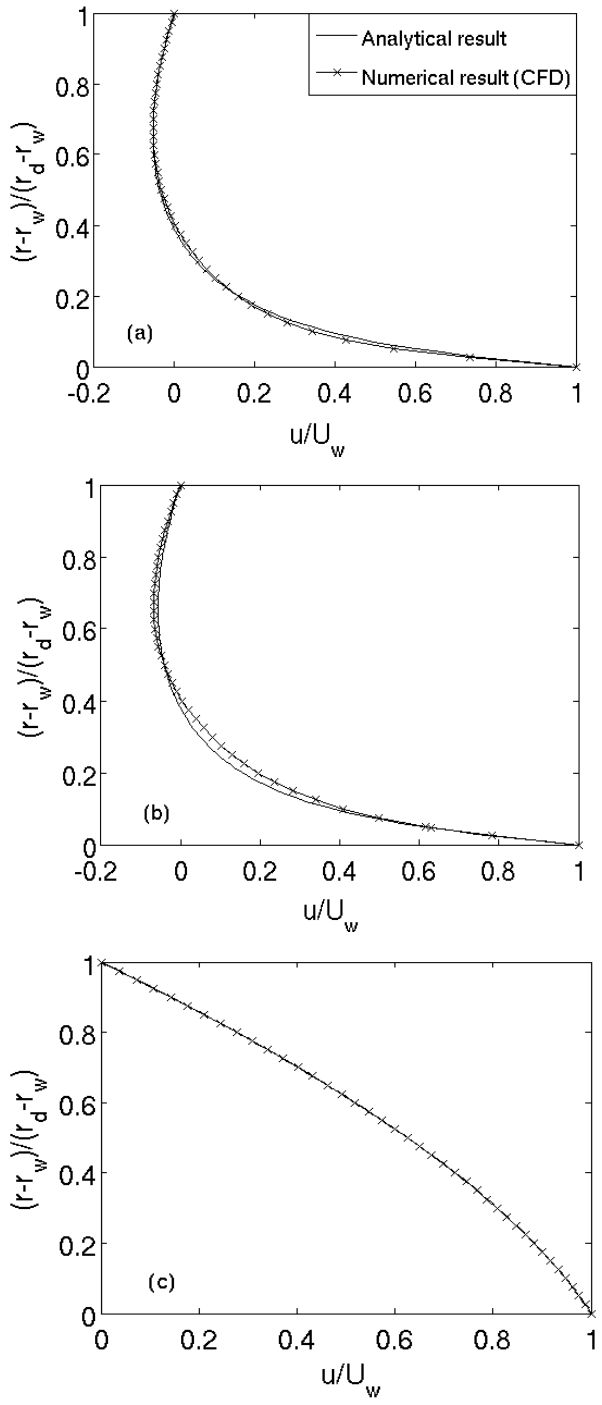

Figure 32: Predicted velocity profiles compared against CFD results at different streamwise positions for Case 3, n_{geo}=1.8: (a) z/L=0, (b) z/L=0.5, (c) z/L=1

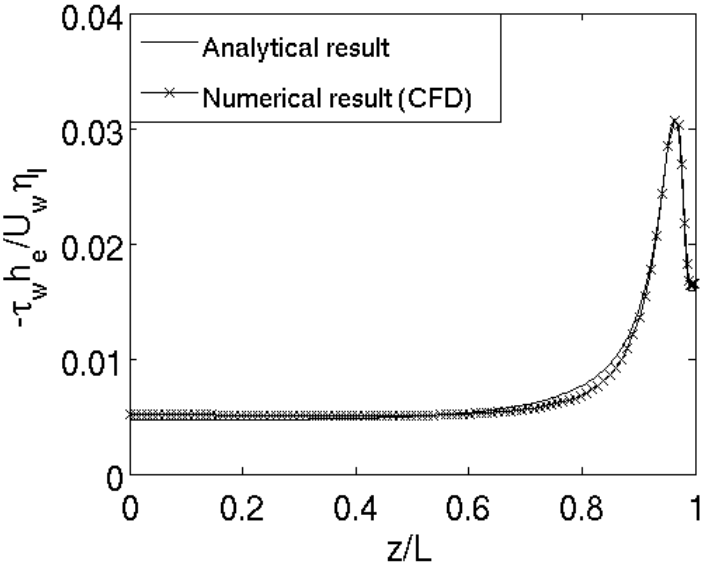

Figure 33: Predicted wall shear stress compared against CFD; Case 3, n_{geo}=1.8

Table 7: Drag forces obtained from the analytical and numerical (CFD) computation

			Newtonian (Case 1)	Shear thinning isothermal (Case 2)	Shear thinning non-isothermal (Case 3)	Shear thickening (Case 4)
n_{geo}=1.8	F_D[N]	Analytical	1.0501	0.3503	0.2346	10.81
		Numerical	1.0608	0.3553	0.2424	10.843
	Relative error [%]		1.00	1.41	3.23	0.34
n_{geo}=10	F_D[N]	Analytical	0.5433	0.2721	0.1790	3.9836
		Numerical	0.5649	0.2783	0.1915	4.0495
	Relative error [%]		3.82	2.22	6.53	1.63
n_{geo}=20	F_D[N]	Analytical	0.4874	0.2620	0.1720	3.1624
		Numerical	0.5021	0.2693	0.1855	3.1584
	Relative error [%]		2.93	2.71	7.3	0.13

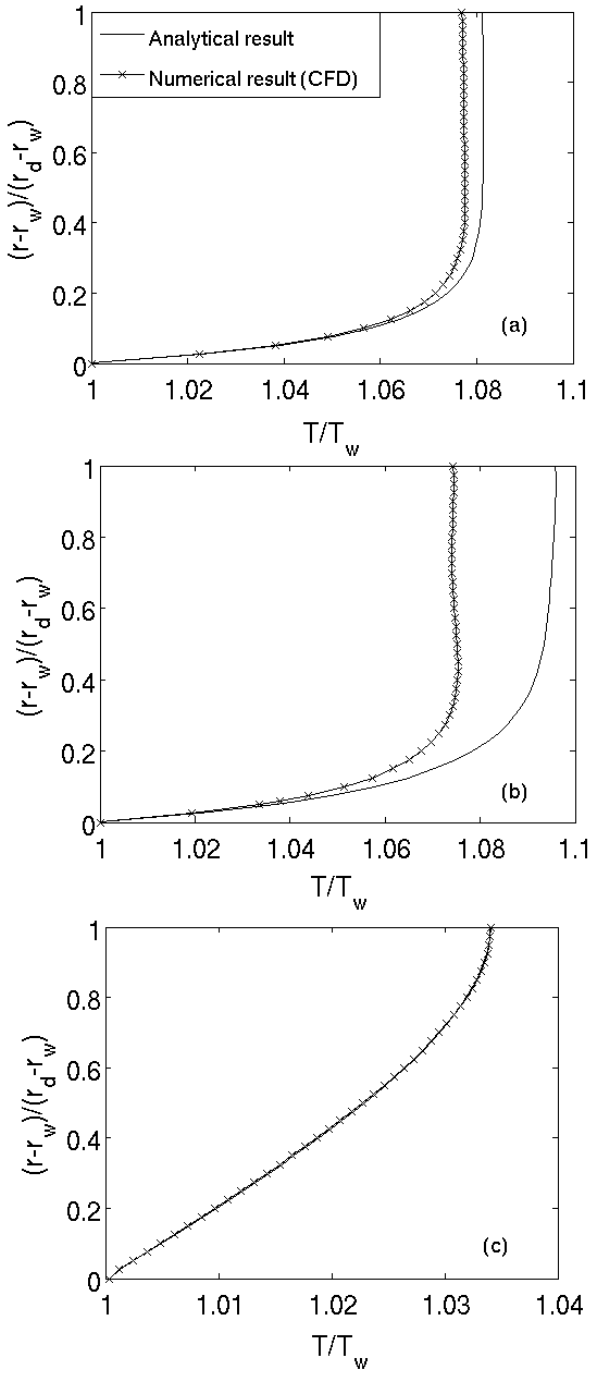

Figure 34: Predicted temperature profiles compared against CFD results at different streamwise positions for Case 3, n_{geo}=1.8: (a) z/L=0, (b) z/L=0.5, (c) z/L=1

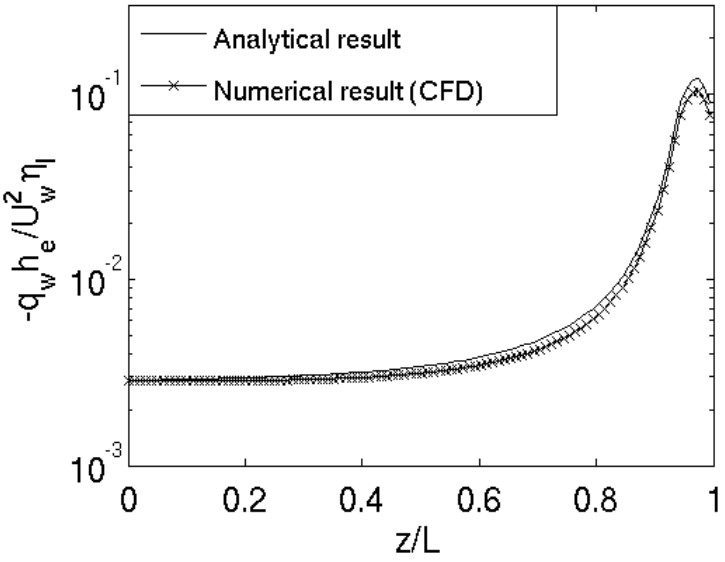

Figure 35: Analytically predicted wall heat flux at the wire compared against CFD results; Case 3, n_{geo}=1.8

3.2.6 Model application to generic die shapes

The targeted reduction of the total drag force is based on the evaluation of influence of the shape of the die by varying the geometry parameter from n_{geo}=0.3 to n_{geo}=50. The four different fluids specified in Table 4 were considered again in order to cover the effect of the rheological behavior as well. Figure 36 gives an overview of the results of this evaluation. The increase in the geometry parameter n_{geo} leads evidently to a monotonous decrease of the drag force regardless of the rheological behavior. As for the influence of the shear rate and temperature on the viscosity, the total drag force clearly reflects the tendency which has already been indicated by streamwise variation of the wall shear stress for the case n_{geo}=1.8 shown in Figure 25. It always reaches the highest level for the shear thickening case, whereas it is always lowest for the case 3 associated with shear thinning and additional thinning at increased temperature. It becomes further evident that the beyond the value $n_{geo}\approx$10 the total drag force shows no significant reduction any more for all types of fluids. This implies that assuming n_{geo}=10 or higher provides a shape of the die which meets the targeted low drag force very well. Since this

result applies to all considered fluids, there is no need for any further modification of the shape dependent of the different rheological properties. It is still important to note that the obtained total drag forces vary over orders of magnitude for the different types of fluid, as indicated by the logarithmic scale of the ordinates in Figure 36. The dashed ordinate to the right shows the corresponding values for tensile stresses on the wire as given by Eq. (91). The horizontal line represents the yield strength of copper, which has the value of about 70 N/mm^2. The tensile stress reaches and exceeds this value for the case of shear thickening and Newtonian behavior of the fluid, as well as for the case of shear thinning in case of small values of n_{geo}. In general shear thickening and Newtonian behavior of the fluid do not describe the realistic enamel behavior, which is usually shear thinning. Nonetheless, even though the stresses may remain below the yield strength limit, they can still be relevant due to the phenomenon termed "low stress elongation". It is known that stresses well below the yield strength, can still cause microstructural changes of the wire material, making it possibly unusable for winding afterwards.

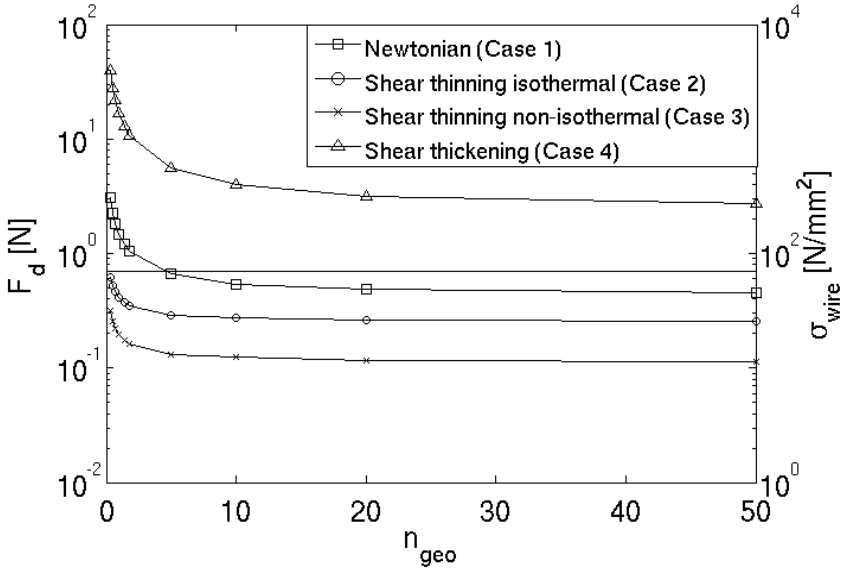

Figure 36: Variation of total drag force and corresponding tensile stress dependent of the parameter n_{geo} for different fluids

3.3 First-order solution

The first-order solution represents basically a linear perturbation of the zeroth-order solution, which accounts for the advective transport of momentum and heat. The perturbed solutions shall particularly provide more accuracy when considering strongly converging geometries associated with a rapid axial decrease in gap height. Accounting for the convective transport of heat shall also improve the predictions for the temperature field, especially for the Prandtl numbers exceeding unity. The first-order extension is applied only to Newtonian fluids with constant dynamic viscosity, though. For non-Newtonian fluids the perturbation of the non-linearly shear rate dependent viscosity would lead to an unfeasible complex mathematical formulation, which impedes the analytical solution of the problem.

Recalling the non-dimensional form of the governing equations (52)-(55), including the series expansions given by Eqs. (62)-(66), and equating all terms of the order ε^1 and $\varepsilon_\Gamma{}^1$, yields the following first-order balance equations for momentum and heat:

$$\left(u_0{}^* \frac{\partial u_0{}^*}{\partial z^*} + v_0{}^* \frac{\partial u_0{}^*}{\partial r^*} \right) = -\frac{\partial p_1{}^*}{\partial z^*} + \frac{1}{r^*} \frac{\partial}{\partial r^*} \left(r^* \frac{\partial u_1{}^*}{\partial r^*} \right), \tag{96}$$

$$\frac{\partial p_1{}^*}{\partial r^*} = 0, \tag{97}$$

$$\frac{1}{r^*} \frac{\partial}{\partial r^*} \left(r^* \frac{\partial T_1{}^*}{\partial r^*} \right) = -\mathrm{Ec} \left(2 \frac{\partial u_0{}^*}{\partial r^*} \frac{\partial u_1{}^*}{\partial r^*} \right) + u_0{}^* \frac{\partial T_0{}^*}{\partial z^*} + v_0{}^* \frac{\partial T_0{}^*}{\partial r^*}. \tag{98}$$

The first-order conservation equation of mass reads

$$\dot{V}_1^* = \int_{r_w^*}^{r_d^*} r^* u_1^* dr^* = const. \tag{99}$$

Assuming no-slip boundary conditions implies zero perturbation for the velocity at both the radially inner moving and outer fixed walls. Assuming a constant wall temperature at the radially inner boundary implies zero perturbation for the temperature as well. Analogously, the adiabatic boundary condition at the radially outer boundary implies a zero gradient for the first-order temperature solution. Based on these assumptions the radial boundary conditions read:

$$r^* = r_w^*: \qquad u_1^* = 0,\ T_1^* = 0, \tag{100}$$

$$r^* = r_d^*: \qquad u_1^* = 0,\ \frac{\partial T_1^*}{\partial r^*} = 0. \tag{101}$$

The prescription of fixed ambient pressure at the inlet and the outlet of the die requires imposing zero pressure perturbations at these axial boundaries.

$$z^* = 0,\ z^* = 1: \qquad p_1^* = 0 \tag{102}$$

In contrast to the zeroth-order solution, accounting for the advective transport of momentum and heat into the axial direction the first-order solution would basically require axial boundary conditions for velocity as well as the temperature to compute the axial derivatives $\frac{\partial u_0^*}{\partial z^*}$ and $\frac{\partial T_0^*}{\partial z^*}$ in Eqs. (96) and (98), respectively. Such a setting is not needed here, as both expressions can be

simply obtained by evaluating the axial derivatives of the analytical zeroth-order solutions for u_0^* and T_0^*, given by Eqs. (84) and (86), respectively.

The first-order solution for the axial velocity is obtained by integrating Eq. (96) in the radial direction and reads

$$u_1^* = A\left(z^*, r^*\right) - A\left(z^*, r_d^*\right)\frac{\ln\left(r^*/r_w^*\right)}{\ln\left(r_d^*/r_w^*\right)} - \frac{1}{4}\frac{dp_1^*}{dz^*}\left[\left(r_d^{*2} - r_w^{*2}\right)\frac{\ln\left(r^*/r_w^*\right)}{\ln\left(r_d^*/r_w^*\right)} - \left(r^{*2} - r_w^{*2}\right)\right], \qquad (103)$$

where $A(z^*,r^*)$ denotes a sum of integrals given as

$$A\left(z^*, r^*\right) = \int_{r_w^*}^{r^*}\frac{1}{r^*}\int_{r_w^*}^{r^*} 2u_0^* r\frac{\partial u_0^*}{\partial z^*}dr^* + \int_{r_w^*}^{r^*} v_0^* u_0^* dr^*. \qquad (104)$$

It can be seen that the zeroth-order solution for the radial velocity component is required in the second integral in Eq. (104). This component is computed from the zeroth-order continuity equation as

$$v_0^* = -\frac{1}{r^*}\int_{r_w^*}^{r^*}\frac{\partial u_0^*}{\partial z^*} r^* dr^*. \qquad (105)$$

The first-order pressure variation is computed by substituting Eq. (103) into the integral mass balance given by Eq. (99) and integrating the obtained expression over the axial direction. The first-order temperature is obtained by integrating Eq. (98) over the radial direction and it reads

$$T_1^* = -2\,\mathrm{Ec}\int_{r_w^*}^{r^*}\frac{D\left(z^*,r^*\right)}{r^*}dr^* + \int_{r_w^*}^{r^*}\frac{E\left(z^*,r^*\right)}{r^*}dr^* + \ln\frac{r^*}{r_w^*}\left[2\mathrm{Ec}D\left(z^*,r_d^*\right) - E\left(z^*,r_d^*\right)\right], \qquad (106)$$

where the integrals denoted by $D(z^*,r^*)$ and $E(z^*,r^*)$ read

$$D\left(z^*,r^*\right) = \int_{r_w^*}^{r^*} r^*\left(\frac{\partial u_0^*}{\partial r^*}\frac{\partial u_1^*}{\partial r^*}\right)dr^*, \text{ and } E\left(z^*,r^*\right) = \int_{r_w^*}^{r^*} r^* u_0^*\frac{\partial T_0^*}{\partial z^*}dr^* + \int_{r_w^*}^{r^*} r^* v_0^*\frac{\partial T_0^*}{\partial r^*}dr^*, \qquad (107)$$

respectively.

3.3.1 Test cases

The results presented in the following were obtained for the same die geometries and operating conditions as defined in section 3.2.3 for the computation of the zeroth-order solution. Accordingly, the diameter of the wire was set to d_w=0.15 mm, the velocity of the wire was set to U_w=22.27 m/s, the length of the die was L=25 mm, the gap height at the exit was h_e=5 µm and the difference in gap height between the die inlet and exit was assumed δ=2.5 mm. Since the first-order expansion shall help to make the analytical solution applicable to a wider range of gap geometries, the results obtained for three very different die shapes shall be discussed. The considered geometries are associated with the geometrical parameter n_{geo}=0.5, n_{geo}=1.8, and n_{geo}=10, which implies that the inner contour of the die varies from a purely convex to a purely concave shape. The first-order solution considers only Newtonian fluid, whose viscosity and thermal conductivity were assumed as η=0.25 Pas, and λ=0.5 W/mK, respectively. For the considered operating conditions and characteristic length scales this implies a Reynolds number $\mathrm{Re_L}$=2230. The specific heat capacity was varied as c_p =2 J/kgK, c_p =10 J/kgK, and c_p =20 J/kgK in order to assess the capability of the proposed first-order extension to capture the convective transport of heat. The selected values of the specific heat capacity translate into Prandtl numbers Pr=1, Pr=5, and Pr=10, respectively. The corresponding values of the Eckert number read Ec=0.72, Ec=0.14, and Ec=0.07, respectively. The reduced Reynolds number defined in Eq. (53),

which is used as expansion parameter in the series expansion for the momentum is $\varepsilon = 8.91\text{x}10^{-5}$. The reduced Pèclet number, which is used as expansion parameter in the series expansion for the internal energy balance (60), varies with the selected Prandtl numbers as $\varepsilon_T = 8.91\text{x}10^{-5}$, $\varepsilon_T = 4.45\text{x}10^{-4}$, and $\varepsilon_T = 8.91\text{x}10^{-4}$, respectively.

The possible gain in accuracy provided by the first-order extension is further evaluated by comparing the predictions of the analytical model against 2D CFD results, which were obtained for the three considered die geometries using the same CFD setup as described in section 3.2.5.1.

3.3.2 Assessment of the analytically predicted momentum and heat transfer

Figures 37 (a) and (b) depict the axial velocity isotachs for the die geometry associated with n_{geo}=1.8 obtained from the extended lubrication theory solution (zeroth- + first-order solution) and numerical CFD solution, respectively, providing a qualitative comparison of the predicted structure of the flow field. The predicted velocity isotachs show very good agreement and exhibit typical features of the converging Couette type flow, such as the partitioning of the flow field into two sub-regions with forward and reverse motion, respectively. The same flow structure was already predicted by the zeroth-order solution as seen from Figure 23. The reason for this good agreement between the CFD results and both analytical solutions (zeroth-order, zeroth- + first-order) is that this particular structure of the flow essentially follows from continuity, which is enforced, and, hence captured, by the analytical solutions at all orders. Figure 38 shows the predictions for the velocity isotachs obtained from the extended lubrication theory solution for the die geometries with n_{geo} =0.5 and n_{geo} =10. It can be seen that regardless of the geometrical outline the basic subdivided structure of the flow field remains unchanged. The contour associated with zero axial velocity, which separates two sub-regions, always resembles the shape of the outer gap contour.

Despite the fairly accurate description of the basic structure of the flow field already provided by the zeroth-order solution, notable quantitative differences occur in the predicted velocity profiles at axial positions, where the cross-sectional area most rapidly changes as indicated by high axial gradients of the outer contour $dr_{\mathrm{d}}^{*}/dz^{*}$. This is illustrated in Figure 39 showing radial profiles of

axial velocity at four selected cross-sections for all considered die geometries. The inclusion of the advective transport in the first-order extension evidently eliminates very well the shortcomings of the zeroth-order solution indicated by its deviations from the CFD results at the positions with the steepest decrease in cross section.

The observed improvements for the velocity profiles are also reflected in the axial variation of the pressure displayed in Figure 40. The first-order correction brings again the analytical solution very close to the CFD results in the in the axial cross sections, where the radial outer contour converges fastest. The observed discrepancy of the pressure profiles between the analytical predictions and numerical results in the close proximity of the die inlet is the result of the domain extension used in the CFD computations in order to match the inflow conditions with the velocity boundary conditions in the analytical solutions. Simulating the flow in such somewhat extended domain leads to a non-zero pressure at the position z/L=0 for all considered geometries. Its value is still vanishingly small, though.

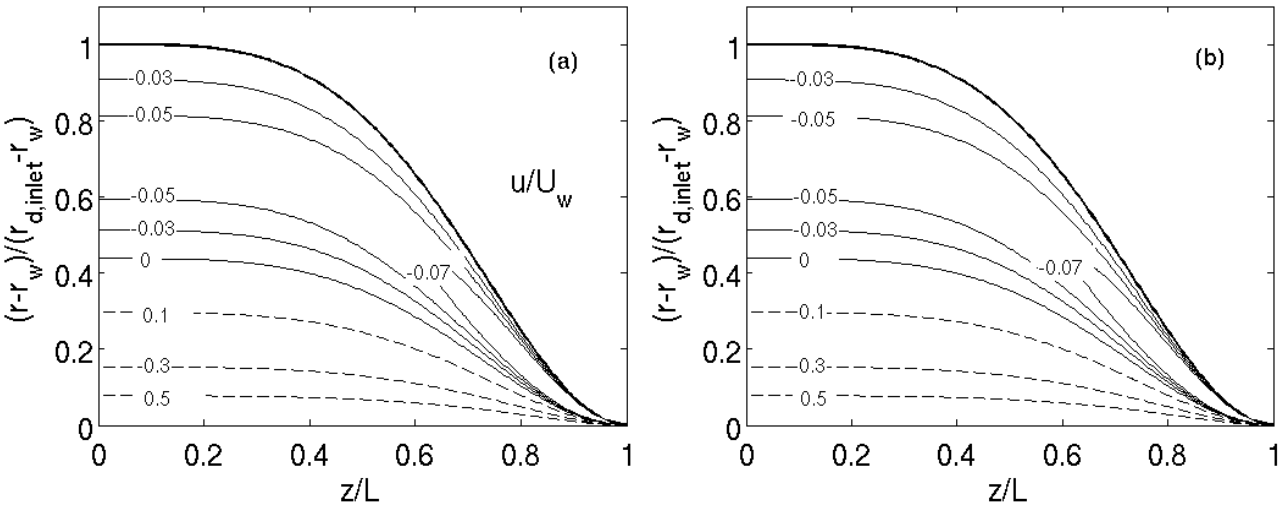

Figure 37: Axial velocity isotachs comparison (n_{geo}=1.8): a) zeroth- + first-order solution, b) CFD

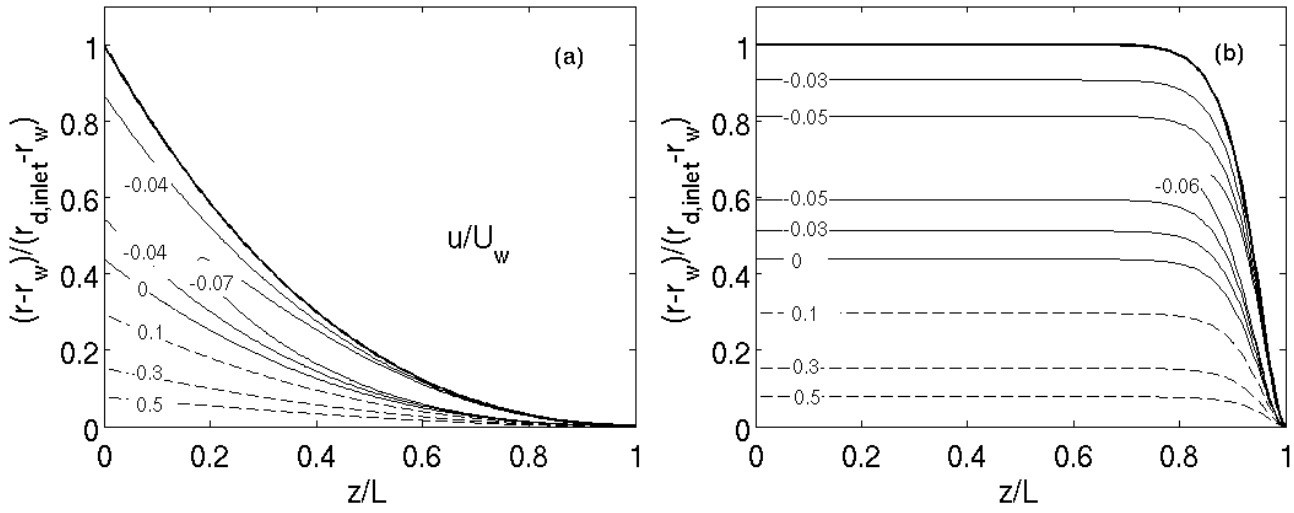

Figure 38: Axial velocity isotachs (zeroth- + first-order solution): a) n_{geo}=0.5, b) n_{geo}=10

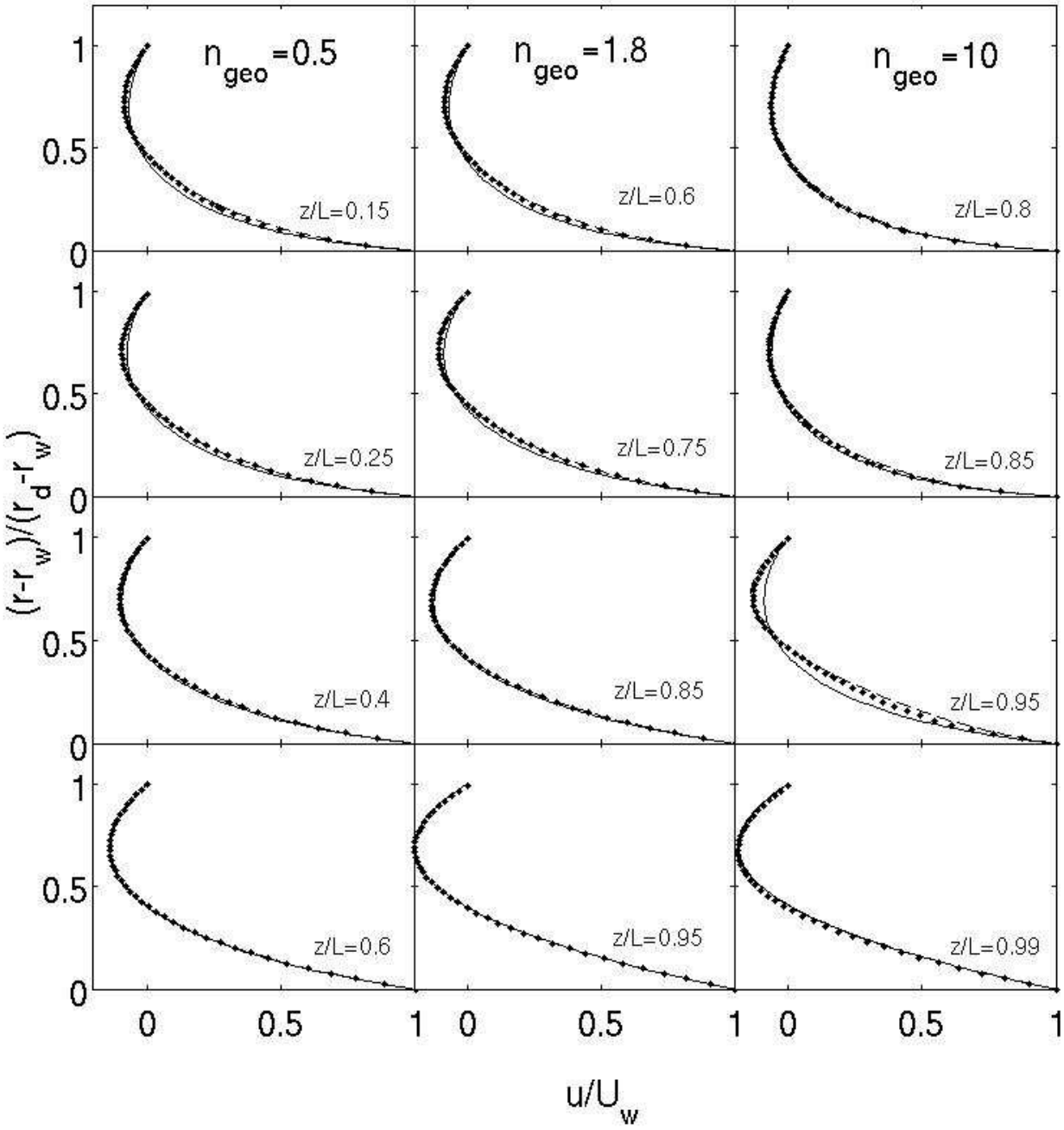

Figure 39: Radial profiles of axial velocity at selected cross sections: zeroth-order (solid line), zeroth- + first-order (dashed line), numerical CFD (dots)

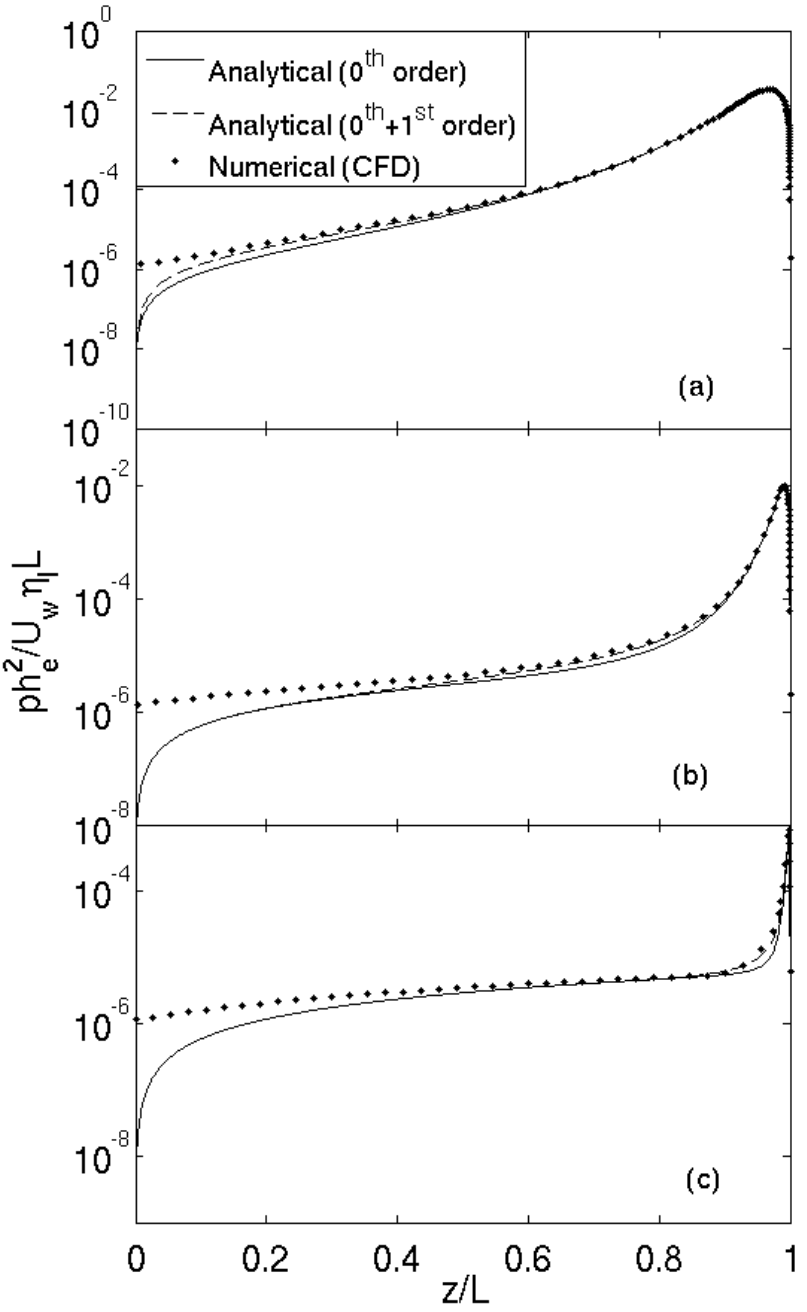

Figure 40: Axial pressure variation: a) n_{geo}=0.5, b) n_{geo}=1.8, c) n_{geo}=10

As compared to the balance of momentum the balance of internal energy involves a source term on rhs of the formulation due to the production of viscous heat. The spatial variation of the viscous dissipation obtained from zeroth- + first-order solution written as

$$\phi^*_{visc,0+1} = \mathrm{Ec}\,\mathrm{Pr}\left[\left(\frac{\partial u_0^*}{\partial r^*}\right)^2 + \left(2\frac{\partial u_0^*}{\partial r^*}\frac{\partial u_1^*}{\partial r^*}\right)\right] \tag{108}$$

is displayed in logarithmic scale downstream of z/L=0.5 in Figure 41. As expected, the viscous heat is mainly generated in the highly sheared region near the moving lower radial boundary with an increasing tendency towards the exit due to the converging geometry. Due to the neglect of convective heat transfer in the zeroth-order solution the generated viscous heat can only be transferred by conduction in the radial direction. As already addressed in the evaluation of the zeroth-order results in the previous section 3.2.5.2 this limitation leads to a significant discrepancy in the prediction of the temperature. The effect of this limitation can be qualitatively seen in the contours of temperature shown in Figure 42, where the zeroth-order solution exhibits markedly increased temperature levels near the adiabatic outer wall. On the other hand, including the convective transport significantly reduces the extension of the high-temperature region as indicated in Figure 42 by the highlighted contour line for T^*=1.3. In the extended lubrication theory solution, as well as in the CFD results, the region associated with T^*>1.3 occupies only a limited zone near the exit, while it extends across the entire radially outer part of the flow domain in the zeroth-order solution.

A more quantitative insight into the possible gain in accuracy of the predicted heat transfer provided by the first-order extension is obtained by comparing the temperature profiles at different axial positions, analogously to the previous assessment of the velocity predictions. Figures 43-45 show the temperature profiles for the different geometries obtained for the considered Prandtl numbers Pr=1, Pr=5, and Pr=10, respectively. It has to be noted that the zeroth-order solution does not vary with the Prandtl number, due to the setting EcPr = *const.*

This implies that the viscous source term on the rhs of Eq. (69) does effectively not change for different Prandtl numbers, so that the zeroth-order solution becomes independent of Pr.

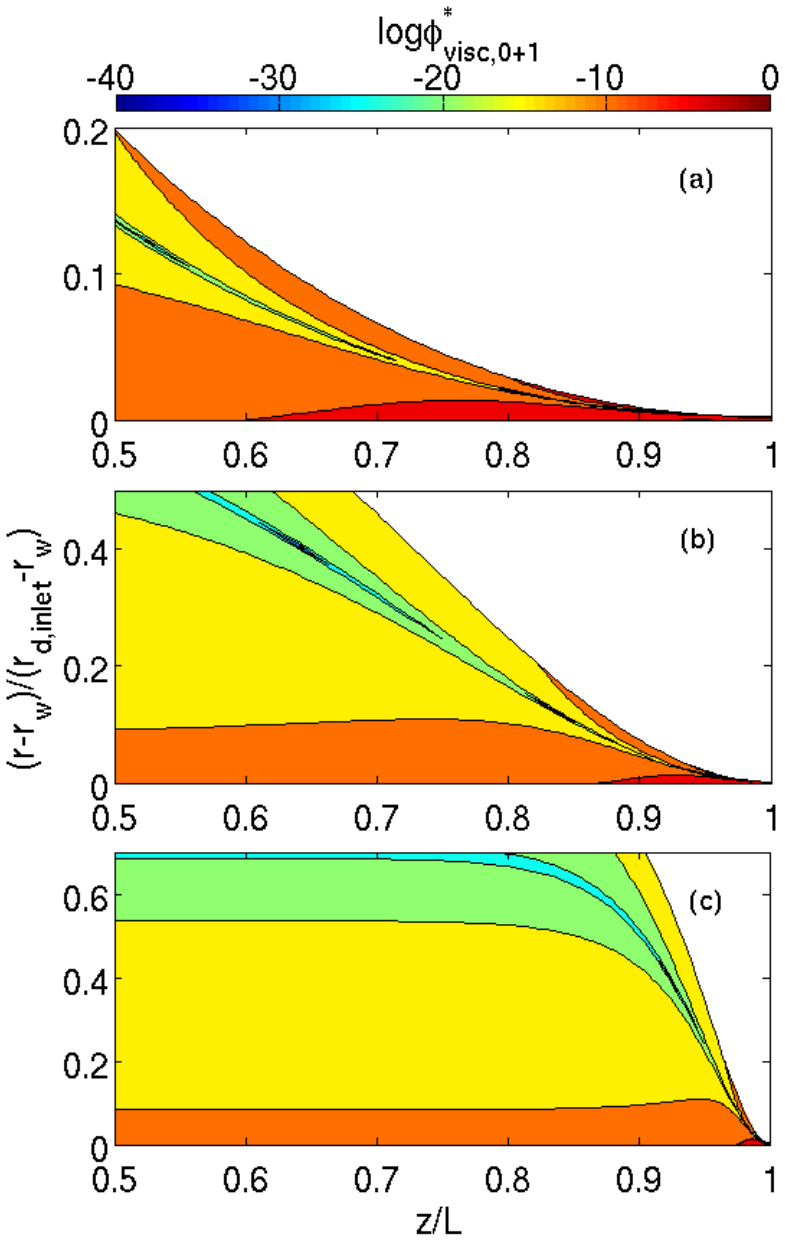

Figure 41: Viscous dissipation (zeroth- + first-order solution) : a) n_{geo}=0.5, b) n_{geo}=1.8, c) n_{geo}=10

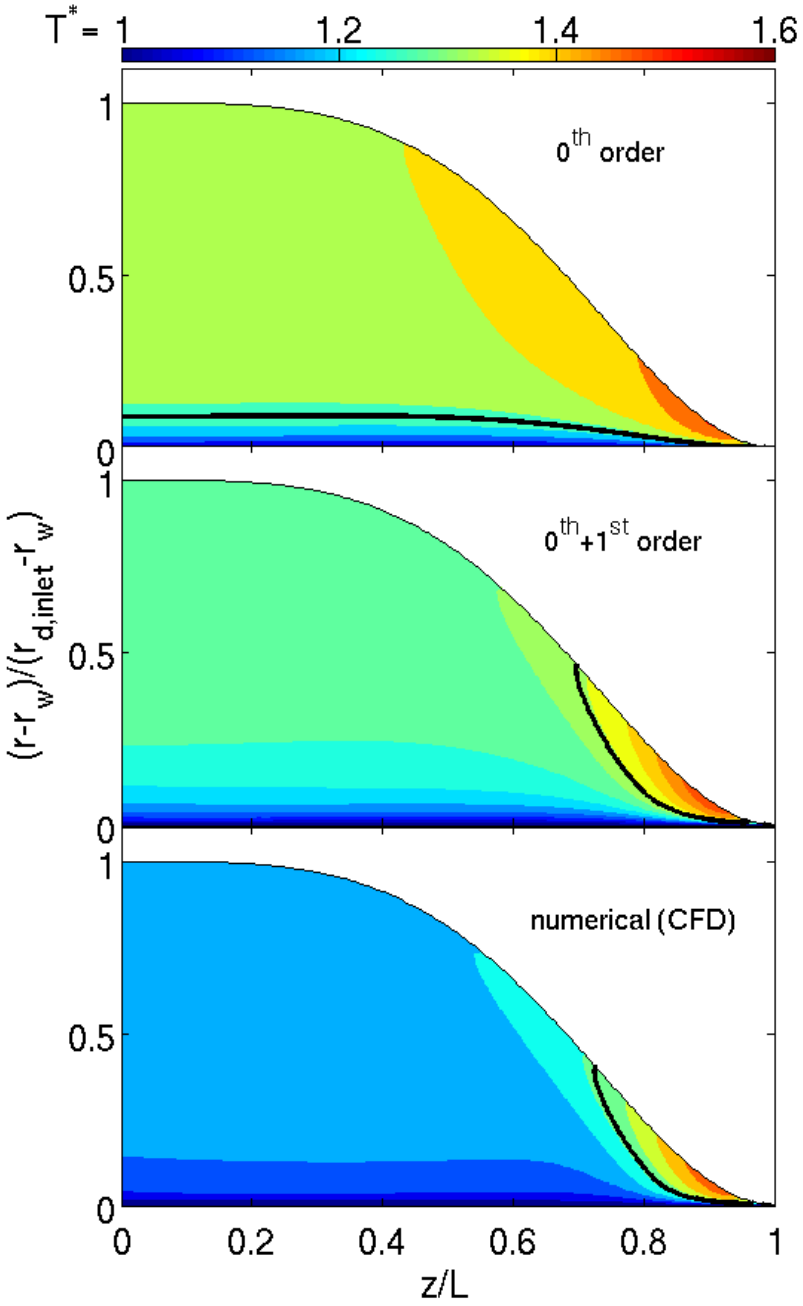

Figure 42: Contours of non-dimensional temperature for geometry n_{geo}=1.8 with Pr=5; black contour line denotes isotherm T^*=1.3

In the case of unity value of Prandtl number the solutions generally agree very well for all considered die geometries due to the relatively small contribution of the convective heat transfer in the internal energy balance. At the cross sections associated with a strong contraction of the radially outer contour the first-order extension still somewhat improves the predictions to a similar extent as observed in the predictions of the velocities. For the higher Prandtl numbers significant differences appear near the radially outer wall. These discrepancies, which have already been addressed above in the discussion of the temperature contours, become evident for all geometries. The zeroth-order generally predicts considerably higher temperatures in the region adjacent to the outer adiabatic wall of the gap. The apparently stronger deviations for increasing Prandtl number can be attributed to the fact that the advective transport in the non-dimensional integral energy balance scales with the reduced Pèclet number, such that its total neglect becomes more influential as the Prandtl number gets higher. Including the first-order extension produces evidently always considerably lower temperatures near the adiabatic outer wall, so that the predicted profiles come much closer to the CFD results for the two higher Prandtl numbers. For Pr=10 the temperature profiles of the extended solution fall even below the CFD solution. For Pr=10 and higher the increasingly high expansion parameter $\varepsilon_T = \mathrm{Re}_L \left(\frac{h_e}{L} \right)^2 \mathrm{Pr}$ leads evidently to an overshooting reduction in temperature, when including only the linear first-order perturbation in the series expansion (65). Applying the series expansion solution to such high Prandtl numbers would require including the non-linear higher-order terms.

While the analytical solutions, especially the zeroth-order approximations, increasingly deviate from the CFD solutions as the Prandtl number is increased, no such pronounced tendency can be observed for the effect of the geometry. The discrepancies between the individual solutions generally tend to increase as n_{geo} becomes higher.

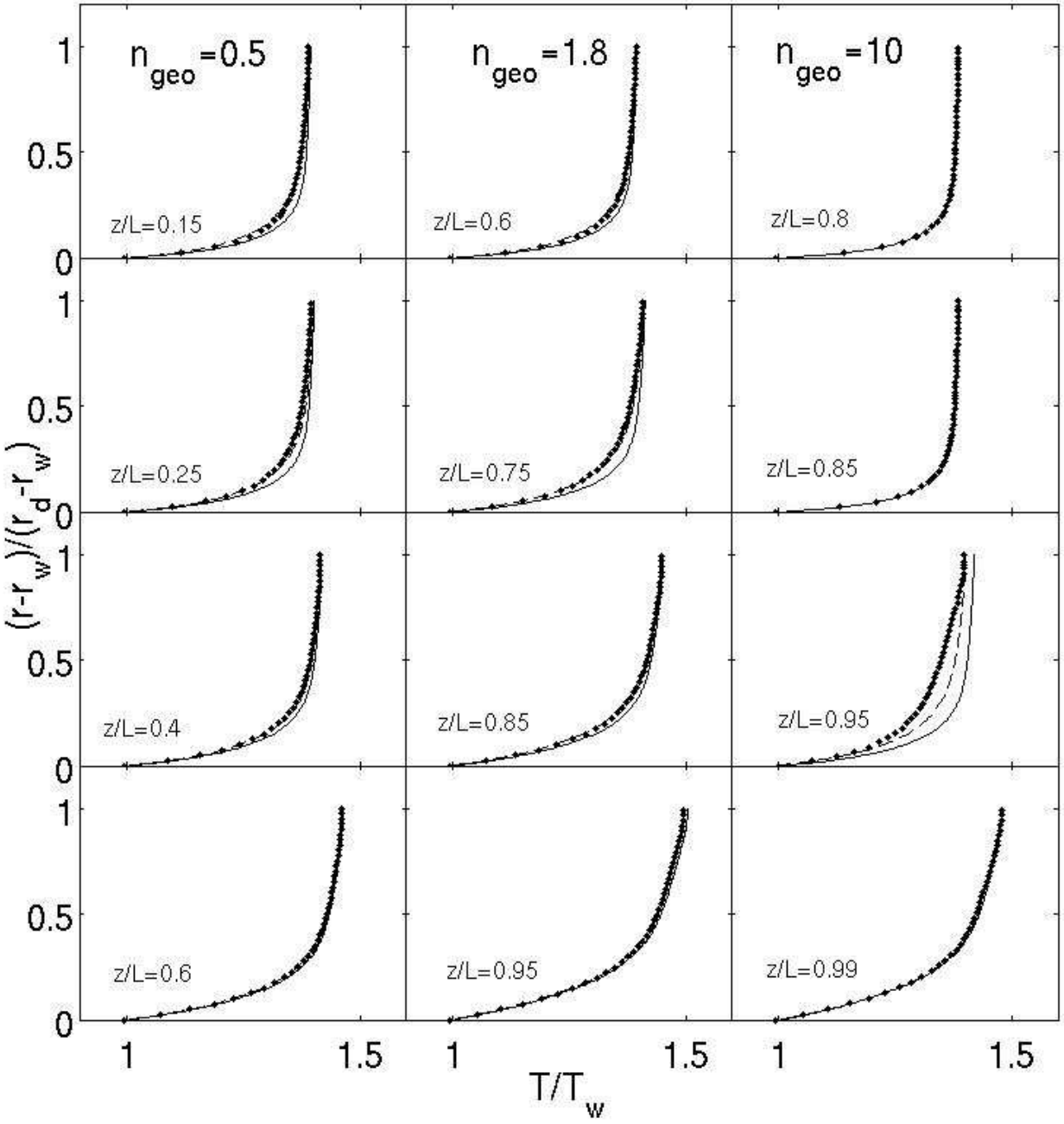

Figure 43: Radial temperature profiles at selected cross sections for Pr=1: zeroth-order (solid line), zeroth- + first-order (dashed line), numerical CFD (dots)

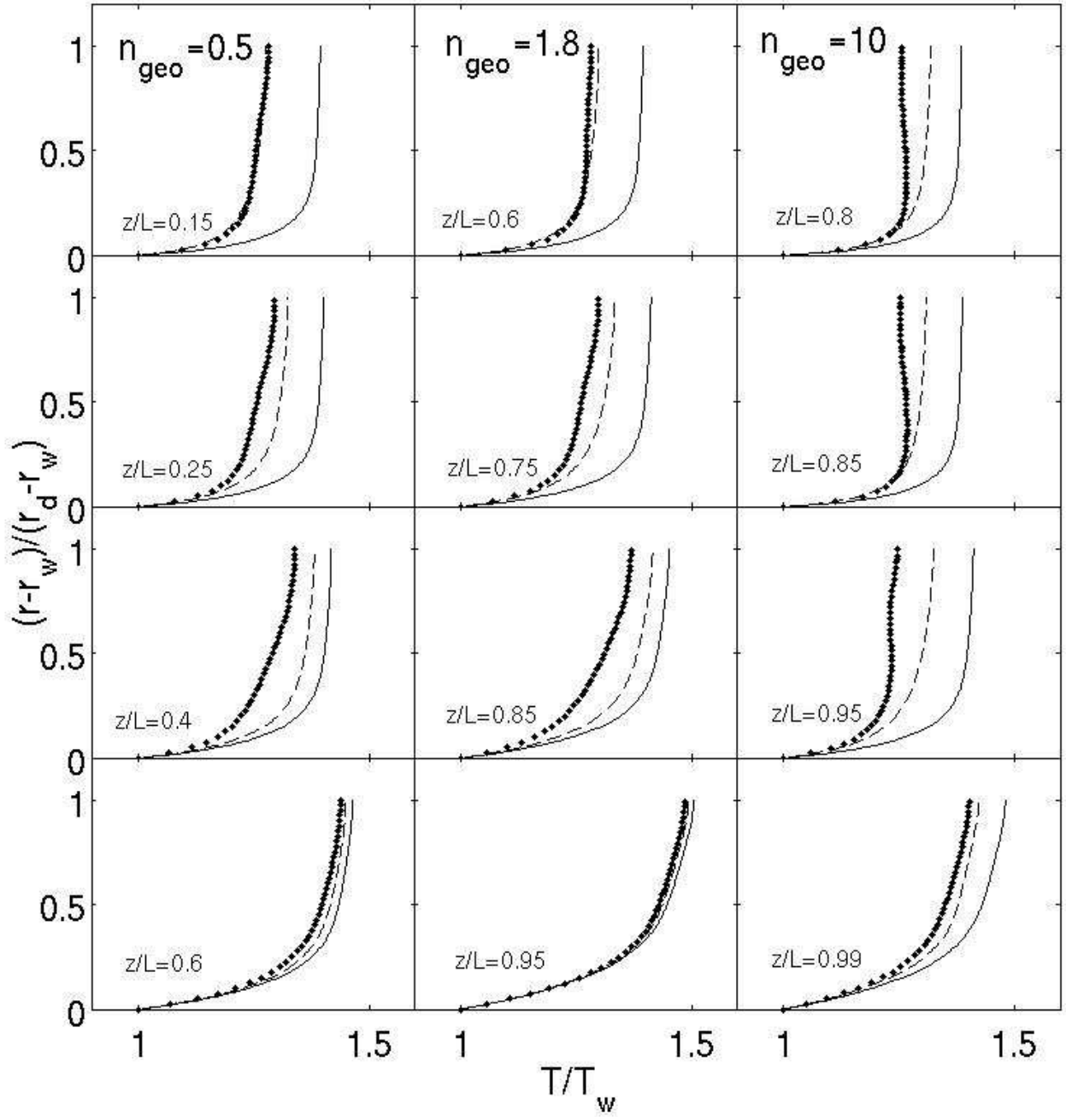

Figure 44: Radial temperature profiles at selected cross sections for Pr=5: zeroth-order (solid line), zeroth- + first-order (dashed line), numerical CFD (dots)

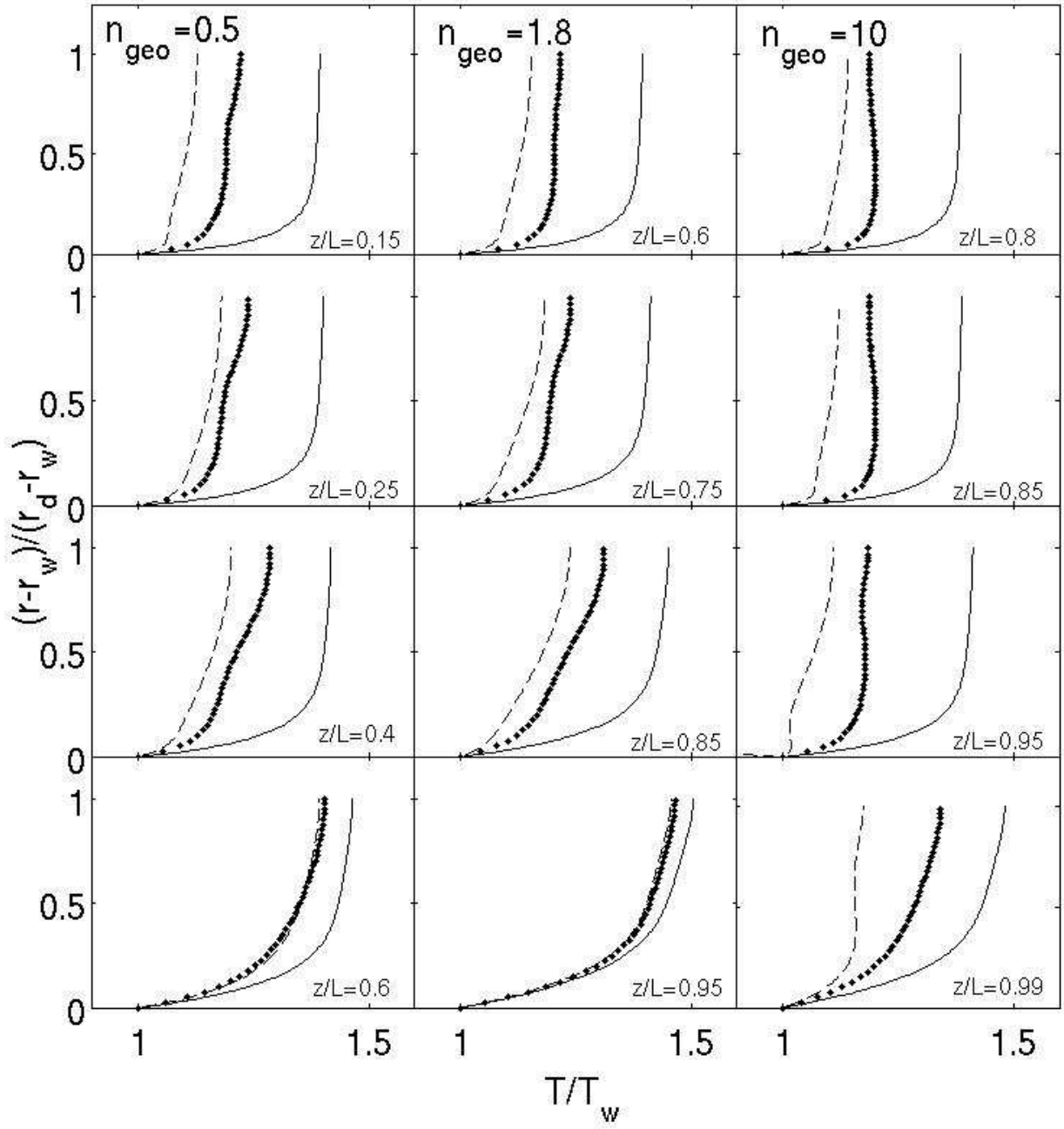

Figure 45: Radial temperature profiles at selected cross sections for Pr=10: zeroth-order (solid line), zeroth- + first-order (dashed line), numerical CFD (dots)

A very detailed insight into the redistribution of the locally generated viscous heat is given by Figure 46, illustrating exemplarily the results for the case of n_{geo}=1.8 with Pr=5. The radial variations of the first-order convective distributions are shown here together with the locally generated viscous heat $\phi^*_{\text{visc, 0+1}}$ computed according to Eq. (108) at four selected axial cross sections. Both the radial and the axial convective term exhibit positive peaks near the moving inner wall. This effectively reduces the increase in temperature caused by viscous heating, whose maximum is always located at the inner radial boundary of the domain. From this maximum the locally generated viscous heat rapidly decreases to almost zero in the rest of the domain as indicated by the steep radial decrease of the red curves.

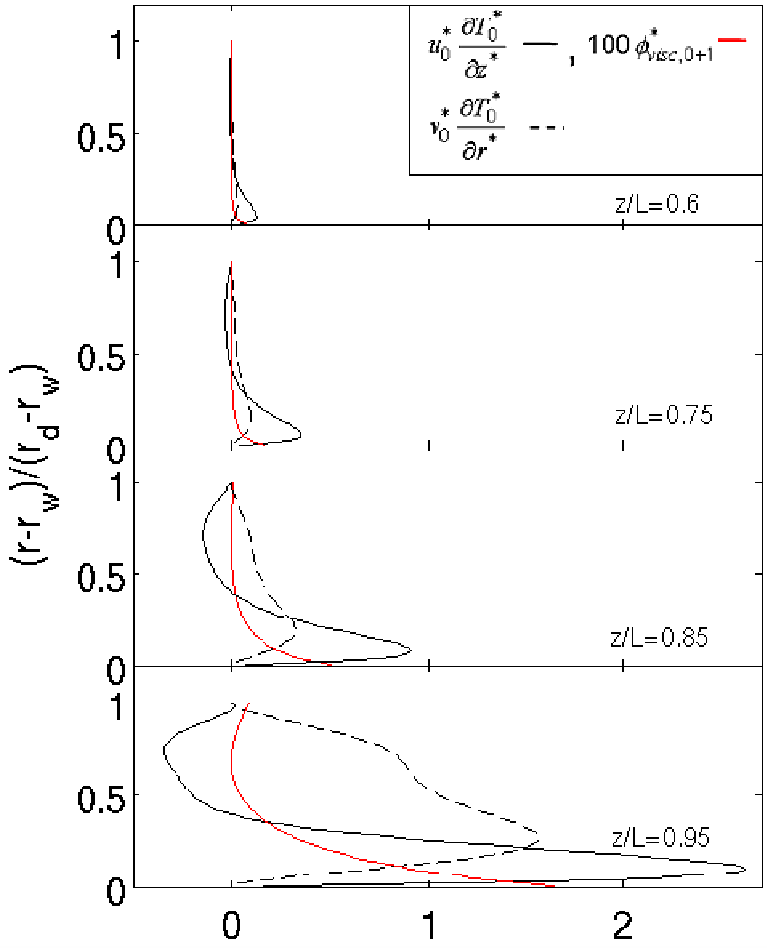

Figure 46: Radial variation of advective transport terms in horizontal and vertical direction and the local viscous heat production for n_{geo}=1.8 with Pr=5

Including the convective transport of heat in terms of the first-order expansion necessarily affects the global energy balance applied to the whole flow domain as well. This global balance of internal energy is also of relevance for satisfying the conservation of energy, which is, unlike the conservation of mass, not explicitly enforced in the analytical solution. The global balance of internal energy over the whole flow domain inside the die can be written as

$$H^*_{z^*=1} - H^*_{z^*=0} = P^*_\eta + Q^*_w. \tag{109}$$

Therein, $P_\eta{}^*$ represents total amount of viscous heat obtained as

$$P^*_\eta = \mathrm{Ec}\,\mathrm{Pr} \int_0^1 \int_{r^*_w}^{r^*_d} \tau^*_{ij} S^*_{ij} r^* dr^* dz^*. \tag{110}$$

Considering dynamically and thermally steady state conditions the produced viscous heat has to completely exit the domain. It can be partly conducted into the wire and partly convectively lost through the die inlet and outlet, as stated in the balance (109). The non-dimensional conductive heat flow into the wire is computed as

$$Q^*_w = -\int_0^1 \left.\frac{\partial T^*}{\partial r^*}\right|_{r^*_w} r^*_w dz^*. \tag{111}$$

The convective heat flows at the die inlet (z^*=0) and outlet (z^*=1) are obtained as

$$H^*_{z^*=0,1} = \mathrm{Re}\left(\frac{h_e}{L}\right)^2 \mathrm{Pr} \int_{r^*_w}^{r^*_d} u^* \left(T^* - 1\right) r^* dr^*, \tag{112}$$

respectively. It is noted that the total convective heat flow at the inlet is always negative, $H^*_{z^*=0}<0$, due to the strong reverse flow in the radially outer region near the adiabatic wall of the die.

The individual contributions to the energy balance as obtained for the considered variation of Prandtl numbers and die geometries are listed in the Tables 8-10. It can be seen that already the zeroth-order solution predicts considerably well the total amount of the produced viscous heat P_η^* for all considered cases. On the other hand, significant differences appear in the distribution of the outgoing heat flow. Considering an adiabatic radial outer boundary the total neglect of advective transport implies that the total generation of viscous heat must be fully balanced by the conductive heat loss into the moving wire in the zeroth-order solution, such that $P_\eta^* = -Q_w^*$. In the case of Pr=1 the contribution of the advective transport appears to be fairly small, as seen from the relatively small convective heat losses predicted by the extended analytical and CFD solutions. For Pr=5, the contribution of the advective transport is evidently more pronounced, and it relatively increases with increasing value of n_{geo}. The convective loss through the die inlet runs up in the case of n_{geo}=10 to approximately 25% of the total production of viscous heat. The convective loss through the die outlet has a negligibly small contribution in all considered cases due to the very small exit gap height. The extended analytical solution (zeroth- + first-order) somewhat overpredicts the convective heat loss through the inlet as compared to the CFD solution for Pr=10. In turn, the conductive heat loss into the wire is somewhat underpredicted. Aside from this small deviation the extended analytical solution appears to describe the redistribution of heat in the global internal energy balance very well.

Summing up the individual contributions according to the global balance (109) it can also be seen that the global conservation of energy is fulfilled in both the zeroth- and first-order solution for all considered cases.

Table 8: Energy balance for different die geometries; Pr=1

	n_{geo}=0.5			n_{geo}=1.8			n_{geo}=10		
	0^{th}	0^{th}+1^{st}	CFD	0^{th}	0^{th}+1^{st}	CFD	0^{th}	0^{th}+1^{st}	CFD
P_{η}^{*}	1.6451	1.6494	1.6502	0.926	0.928	0.929	0.3674	0.3714	0.3725
$-Q_{w}^{*}$	1.6451	1.6296	1.6303	0.926	0.9116	0.9123	0.3674	0.353	0.3539
$-H_{z^{*}=0}^{*}$		0.0194	0.0194		0.0161	0.0163		0.0178	0.0179
$H_{z^{*}=1}^{*}$		0.0004	0.0005		0.0003	0.0004		0.0006	0.0007

Table 9: Energy balance for different die geometries; Pr=5

	n_{geo}=0.5			n_{geo}=1.8			n_{geo}=10		
	0^{th}	0^{th}+1^{st}	CFD	0^{th}	0^{th}+1^{st}	CFD	0^{th}	0^{th}+1^{st}	CFD
P_{η}^{*}	1.6451	1.6494	1.6502	0.926	0.928	0.929	0.3674	0.3714	0.3725
$-Q_{w}^{*}$	1.6451	1.5505	1.5507	0.926	0.8462	0.8455	0.3674	0.2798	0.2795
$-H_{z^{*}=0}^{*}$		0.097	0.097		0.0804	0.0816		0.0888	0.0896
$H_{z^{*}=1}^{*}$		0.0019	0.0025		0.0014	0.0019		0.0028	0.0034

Table 10: Energy balance for different die geometries; Pr=10

	n_{geo}=0.5			n_{geo}=1.8			n_{geo}=10		
	0^{th}	0^{th}+1^{st}	CFD	0^{th}	0^{th}+1^{st}	CFD	0^{th}	0^{th}+1^{st}	CFD
P_{η}^{*}	1.6451	1.6494	1.6502	0.926	0.928	0.929	0.3674	0.3714	0.3725
$-Q_{w}^{*}$	1.6451	1.4321	1.4515	0.926	0.7555	0.7622	0.3674	0.1758	0.1867
$-H_{z^{*}=0}^{*}$		0.2110	0.1937		0.1681	0.1631		0.1885	0.1791
$H_{z^{*}=1}^{*}$		0.006	0.005		0.0044	0.0037		0.0071	0.0067

3.4 Scope of the analytical model

Based on the discussion of the analytical results and the validation against CFD data the scope and the limits of the zeroth-order solution, which essentially represents the full lubrication theory approximation, and of the first order extension can be summarized as follows:

Zeroth-order solution

- predicts the velocity field very well despite the effectively increased values of the local reduced Reynolds number above unity
- captures very well the effect of different rheological properties in terms of shear thinning or shear thickening on the flow and temperature fields inside the die.
- predicts reliably well the axial variation of the wall shear stress and the and the resulting drag force on the wire
- captures sufficiently accurately the effect of the geometry of the die on the resulting total drag forces for all considered rheologies
- describes fairly accurately the local production of viscous heat
- exhibits major shortcomings in the predicted heat transfer as the Prandtl number exceeds unity. This particularly means that

    the increase in temperature caused by viscous heating is significantly overpredicted

    the conductive heat transfer into the moving wire is predicted too high

    the convective heat loss with the reverse flow at the inlet is completely disregarded in the global internal energy balance.

First-order extension

- accounting for the advective transport in the momentum balance improves the zeroth-order predictions for the velocity at the positions inside the die with the steepest decrease in cross section

- the inclusion of the convective heat transport effectively leads to a smaller increase in temperature caused by viscous heating, bringing the predicted temperature profiles much closer to the CFD data
- describes the individual contributions to the global balance of internal energy very accurately
- is restricted to Newtonian fluids with constant dynamic viscosity. A shear rate dependent viscosity would lead to a first-order formulation, which cannot be solved analytically.

Summing up, it can be stated that the zeroth-order solution can be applied as a reliable and computationally efficient tool when considering the flow field evolving inside the die for fluids with different rheological behavior in the large variety converging gap geometries, ranging from purely convex to purely concave. For an accurate description of the local heat transfer it is necessary to extend the model using the presented first-order perturbation in order to account for all relevant heat transfer mechanisms.

4. APPLICATION TO REAL ENAMELING DIE GEOMETRIES

A highly controlled deposition of a defined liquid enamel layer on the wire surface is a prerequisite for the production of high quality magnet wires. Realizing this deposition based on the principle of die coating poses two particular challenges:

First, the fresh coating must not be overheated in the drying and curing zones, which the wire passes immediately after each deposition step. This limits the residence time of the wire in the respective heated regions, implying that, the thinner the wire, the higher the production velocity (= wire velocity). In the practical application, this relationship is determined by the operating parameter "*vxd*" representing the product of the production velocity (given in m/min) and the wire diameter (given in mm). Due to the tendency to push this parameter as high as possible for productivity reason the thin wires are inherently subject to the highest flow induced shear forces.

Secondly, for the sake of a most efficient coating process and low costs for diluent solution the manufacturers of enameled wire tend to deposit a highest possible amount of solid mass per each pass through the dies. This ambition fosters the general trend using fresh enamel solutions with the highest possible content of solid mass being mainly constituted by large polymers, which are less volatile during the drying and curing process. Using such highly concentrated fresh enamel solutions implies a strongly increased dynamic viscosity, which further adds to the total drag force on the wire.

In summary, both challenges have in common, that they expectedly bring about significantly increased mechanical loads especially on the thin wires. Even though this increase may not yet be high enough for wire breakage, it may still lead to a so called "low stress elongation" (LSE) of the material, which makes the wire unusable for further application like winding on spools.

Table 11 lists the horizontal wire enameling machines presently produced by the company MAG, including the ranges of possible wire diameters, velocities, and enamel solid contents they cover. The machine processing the thinnest wires is evidently associated with the most stringent upper limit in solid content. Accordingly, it was reported by magnet wire producers that the range of wire diameters processed on the machine Mozart Zero H3 is generally the most critical one, where both wire deformation and even wire breakage most likely appear even when applying

initial basecoat.

Table 11: Horizontal machines, some of their key operating conditions and proposed ranges of solid content for the enamels

Machine model	Mozart Zero H3	Mozart Zero H4	Mozart Zero H5	Mozart Zero H6
Wire material	Copper	Copper	Copper	Copper
Wire diameter	0.15-0.35 mm	0.20-0.50 mm	0.30-0.80 mm	0.50-1.20 mm
Production velocity	1240-487 m/min	1135-416 m/min	733-236 m/min	416-111 m/min
Enamel solid content	up to 32%	up to 36%	up to 40%	up to 45%

Reliable drag force calculations require first of all a very accurate description of the die geometry. Wire enameling dies basically consist of a stainless steel body, into which the die core is embedded. While the geometry of the steel body is the same for all wire diameters, the inner radial geometry of the die core is varied in order to provide the targeted gap height between the moving wire and the inner surface of the die. Regarding the material the die cores are made from there are currently two types available on the market. The most widely used type of dies cores is made of hard metal. The other type is made of diamond, and is used rather scarcely due to the markedly higher price of the material.

4.1 Present die designs

4.1.1 Hard metal dies

As stated in the previous section the wire enameling dies usually consist of two main parts, the steel body and the core of the die. The first is typically produced in a standard geometry being the same for the whole range of die exit diameters. The die core is responsible for removing the excess enamel deposited on the wire surface in the preceding dip coating process and for ensuring the desired thickness of the fresh coating at the exit of the die. Therefore, the core part of the die has to be made from a material which can be processed with high geometrical accuracy, and also provides high durability during the operation. Hard metal can meet these requirements reasonably well. It is therefore widely used as core material, in particular tungsten carbide.

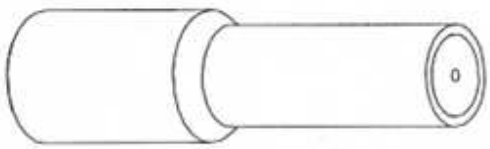

Figure 47: Outer design of the die body

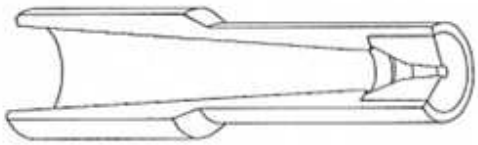

Figure 48: Meridional section; inner design

Figure 47 shows the outer design of the die body, while Figure 48 shows a meridional cut through both the stainless steel body and the core at the die exit. The radially outer contour of the die is shown in Figure 49, including a more detailed view of the exit section made of hard metal.

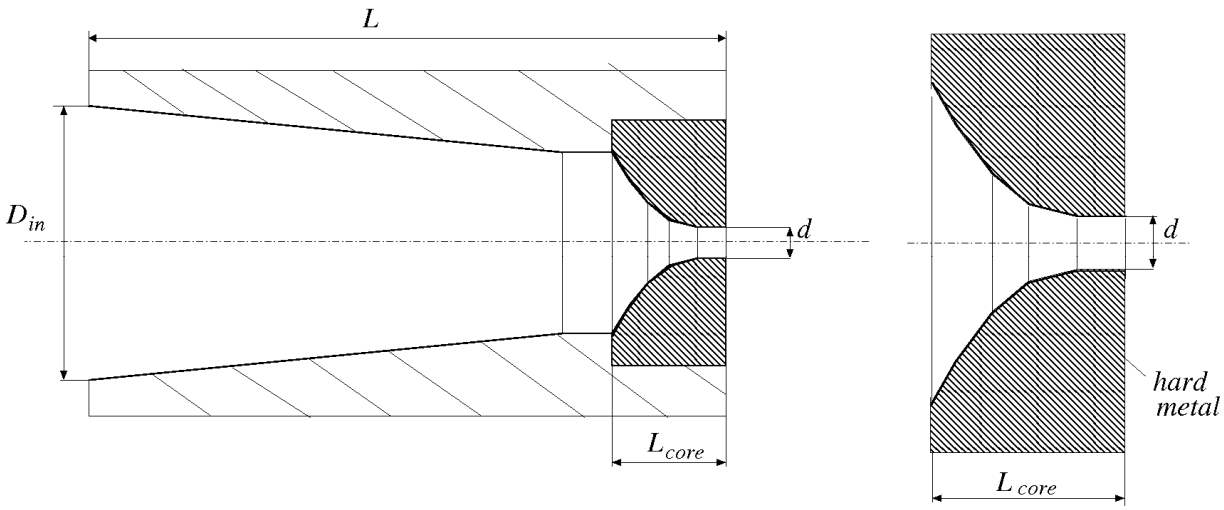

Figure 49: Hard metal die geometry

The die cores are produced for a specific wire diameter. The pre-fabricated hard metal dies have in general a core with a conically shaped exit hole. The desired short cylindrical shape of the exit section, which essentially determines the resulting deposition height of fresh enamel, is realized in a further manufacturing step. In this final step the cylindrical exit geometry is obtained by pulling a bore with a defined diameter $d_{bore} = d$ through the converging exit section of the pre-fabricated die. As seen from Figure 50 the resulting length of the cylindrical exit section, generally termed calibration region, depends of the bore diameter and the cone angle α of the exit hole of the pre-fabricated die. The increase in diameter due to the successive deposition of enamel in each pass through the dies has to be matched with a corresponding increase in exit diameter of the dies d being successively passed by the wire as well. This increase is generally realized in diameter steps of 5 µm.

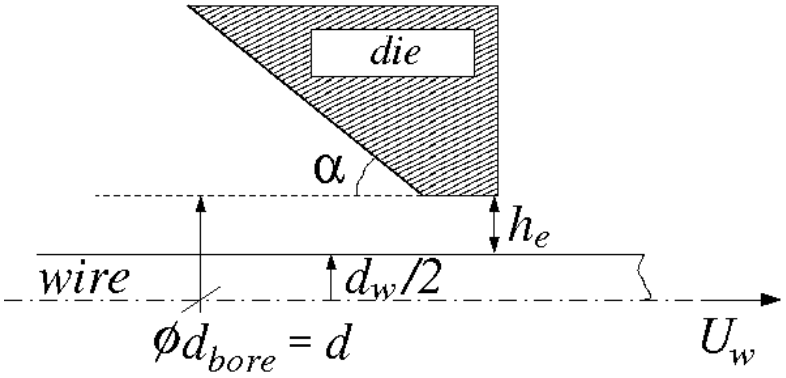

Figure 50: Die exit section

4.1.2 Diamond dies

The dies with diamond cores also cover a wide range of wire diameters, so that they are basically applicable to all types of wire enameling machines. Usually the dies covering smaller wire diameters have cores made of natural diamond, while for the larger diameters synthetic polycrystalline diamond is mainly used. The radially outer contour of the die with a diamond core is shown in Figure 51. It can be seen that the main geometrical outline of the die is similar to the one with a tungsten carbide core. The design mainly differs in the detailed geometry of the exit section made of diamond, shown in the zoom in Figure 51.

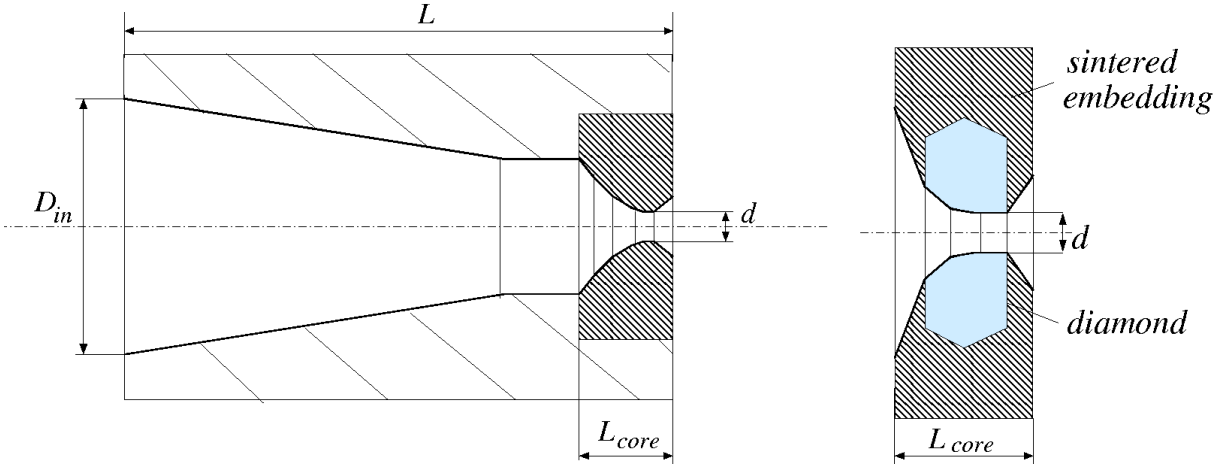

Figure 51: Diamond die

The complex production procedure of diamond dies ensures highest possible accuracy regarding the diameter and the shape of the calibration region. Since diamond can practically not be deformed it is no longer possible to use a bore to finalize the cylindrical calibration section as in the case of hard metal cores.

The production process is divided into multiple steps. First, it is necessary to conduct an optical inspection for the selection of diamonds which are suitable for this kind of application. They must not have any imperfections in their internal structure, because during further manufacturing steps (especially drilling) any imperfection can cause breakage of the diamond making it unusable. After selecting appropriate diamonds without any relevant imperfections the top and the bottom surfaces of each diamond are flattened which become the inlet and the outlet cross sections of the final geometry. After that the diamonds are embedded in a sinter shell which finally holds the diamond core inside the die body. The realization of the accurate diameter of the calibration section is again a multiple stage process:

A conical hole is initially drilled into the diamond using a special laser drilling technique. The surface of the obtained conical hole is then further smoothened with ultrasonic shaping, where an ultrasound probe gradually removes the step-like roughness elements produced by the laser drilling, making the surface optically smooth. In a final polishing step the targeted diameter of the cylindrical calibration section is produced with very high geometrical accuracy. In this step a thin wire covered with diamond paste is pulled through the die, grinding a small amount of excess material from the surface. This process can take even up to three days in order to ensure perfect surface quality.

The outstanding hardness of the diamond material together with the sophisticated production of the calibration section brings about least possible deviations of the real geometry from the target geometry. Imperfections in the real geometry, such as a slightly oval instead of a cylindrical shape of the calibration section, inevitably lead to a faulty deposition, which, when accumulating in successive deposition steps, possibly lead to solid contact between the moving wire and the die, resulting in a breakage of the wire. Apart from the highly accurate geometry diamond is further extremely resistant to weir, so that it can resist against a long term change of the geometry during the operation.

4.2 Computational analysis

The computational analysis of the flow evolving inside real enameling dies with a piecewise linear contraction of the radially outer contour was conducted analogously to the analysis of the flow inside dies with different generic shapes presented in the previous section. The present computations consider real-life geometries of hard metal and diamond dies, assuming for both types the same operating conditions.

The computations in particular investigate the flow field evolving inside the wire enameling dies for the most critical cases, where wire breakage frequently occurs, as it is reported from the magnet wire producers. Since the focus of this investigation is on the prediction of the hydrodynamical drag force exerted on the wire as a possible reason for deformation and breakage of the wire, the computational results will all be presented in dimensional form. As already stated above, the production parameter *vxd* (= product of wire velocity and diameter) is generally pushed as high as possible for productivity reason, which implies that the small wire diameters are associated with very high production velocities. The most critical cases will therefore be met in the enameling of the thin wires. The present computations consider in particular the diameter d_w=0.25 mm, which is well representative for the thin wire processing covered by the machine Mozart ZERO H3. The highest shear rates appearing during the complete multi-pass coating process will not be observed in the passage of the first die due the relatively large gap heights. The largest shear rates are rather expected in some of the successive passes, where the already solidified coating of the previous deposition steps effectively leads to a thicker wire entering the next die and, hence, smaller gap heights. For that reason the wire diameter actually chosen for computation exceeds the value of the bare wire diameter $d_{w,0}$ = 0.25 mm, taking into account amount of enamel already deposited on the wire surface. As it can be seen from Table 11 the enamel which is currently applied to the considered thin wire diameter range contains between 25% and 32% solid mass fraction of polymer. It has been reported that using hard metal dies, exceeding the upper limit of this range would lead to permanent deformation or even breakage of the wire. The present computations attempt to gain more insight into this problem assuming two basecoat enamels with 25% and 45%, respectively.

Especially the latter concentration, which markedly exceeds the currently permissible range shall reveal to which extent the increase in viscosity can finally contribute to wire deformation and breakage due to an increased drag force.

A reliable description of the flow field inside the die requires first of all a realistic description of the rheological behavior of the considered wire enamels. The shear rate dependent behavior of the fluid was described using series of measurements for different enamel solid contents. The obtained flow behavior was implemented into the analytical formulation using a Carreau-Yasuda model, whose model parameters were fitted to the measured data. The extension of the Carreau-Yasuda model towards the second Newtonian plateau could not be based on experimental measurements, as the respective range of extremely high shear rates cannot be reached using conventional measuring techniques for measuring viscosity. The level of the second Newtonian plateau, which is indicated in the flow curves shown in Figure 52 (a) and (b) as dashed line had therefore to be arbitrarily chosen.

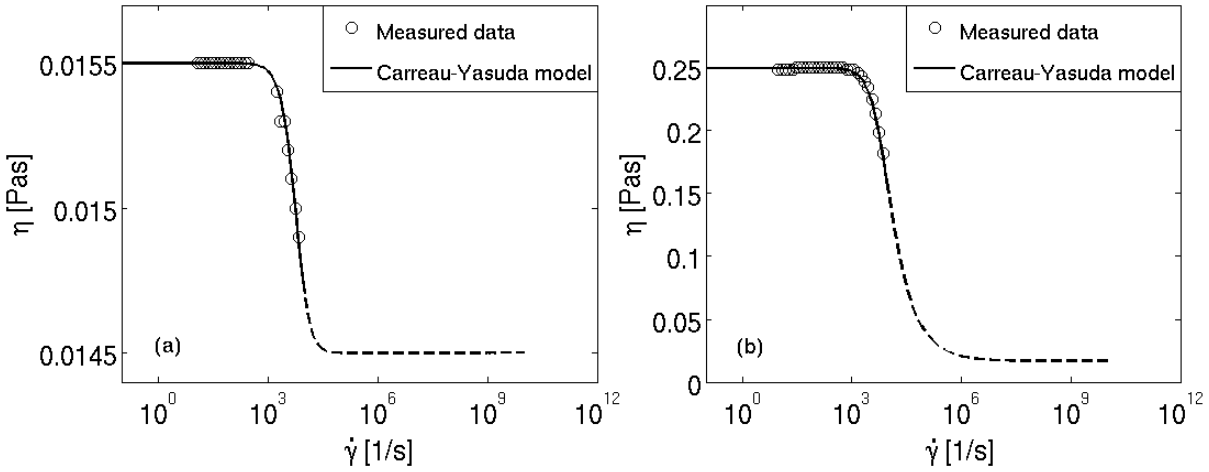

Figure 52: Shear rate dependent viscosity; (a) Terebec 533-25 (b) Terebec 533-45

The parameters used for fitting the Carreau-Yasuda model to the measurements are given in Table 12.

Table 12: Model parameters for Carreau-Yasuda model

	Terebec 533-25	**Terebec 533-45**
η_I [Pas]	0.0155	0.25
η_{II} [Pas]	0.0145	0.0167
K_1 [s]	0.000145	1.74×10^{-5}
$m_{1/2}$ [-]	1.4	0.3

4.2.1 Results for hard metal dies

Accounting for an already solid coating of height h_s=0.01 mm which has been deposited in the passes before, the computations consider a wire diameter $d_w = d_{w,0} + 2h_s$=0.27 mm. The wire velocity and die exit gap height were set to U_w=11.5 m/s, and h_e=8.2 µm, respectively.

Figure 53 shows the contours of the axial velocity which were computationally obtained for the two considered wire enamels. The difference in solid content does evidently not affect the structure of the flow field inside the die, which is characterized by strong backflow in the radially outer part of the domain, carrying the excess enamel towards the die inlet, and forward flow in the radial inner region of the domain, where the enamel is entrained by the motion of the wire.

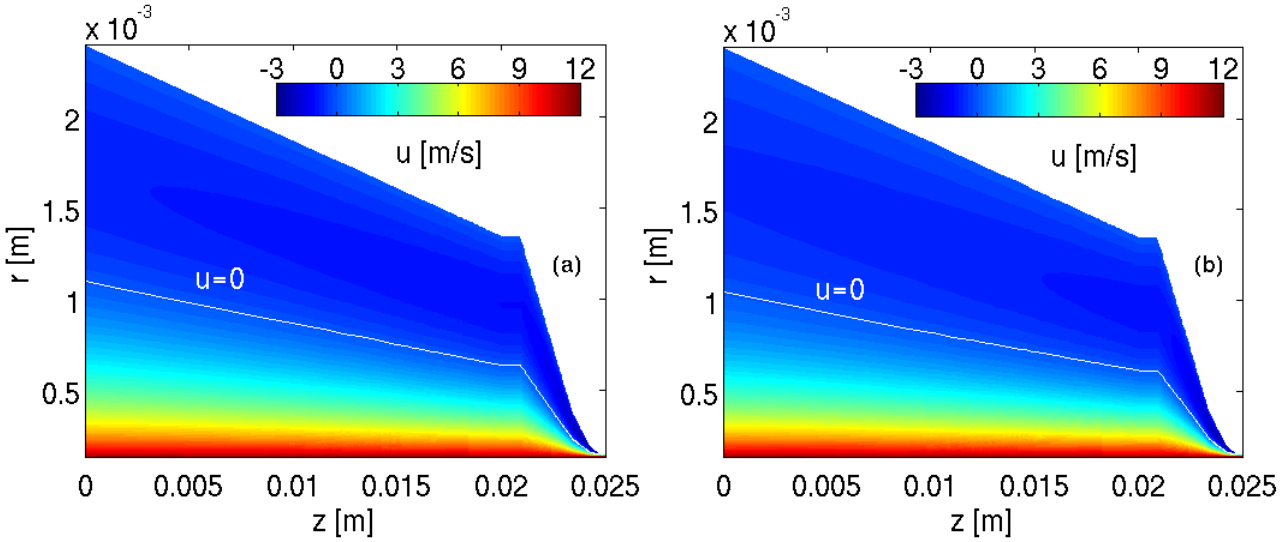

Figure 53: Velocity contours inside hard metal die: (a) Terebec 533-25, (b) Terebec 533-45

A more quantitative insight into a possible effect of the different considered polymer concentrations shall be given by the velocity profiles obtained at selected cross-sections of the domain. The positions of the cross sections were chosen similarly to the discussion of the results for the generic die shapes located at the die inlet (z=0 mm), the middle (z=12.5 mm) of the die, and die outlet (z=25 mm), respectively. Figure 54 shows the velocity profiles as obtained at these three positions. At the inlet and the middle cross section the velocity profiles for the case of the fluid with 45% solid content are evidently a bit more bulky. This difference can be attributed to the fact that the enamel with 45% solid content exhibits a considerably more pronounced shear thinning behavior than the one with 25% solid content as seen from the flow curves in Figure 53. In the last cross section at the die outlet velocity profiles practically collapse so that the volumetric flow rate at the exit is the same. This implies that the amount of the deposited fresh enamel on the surface of the wire is not affected by the amount of solid content in this case.

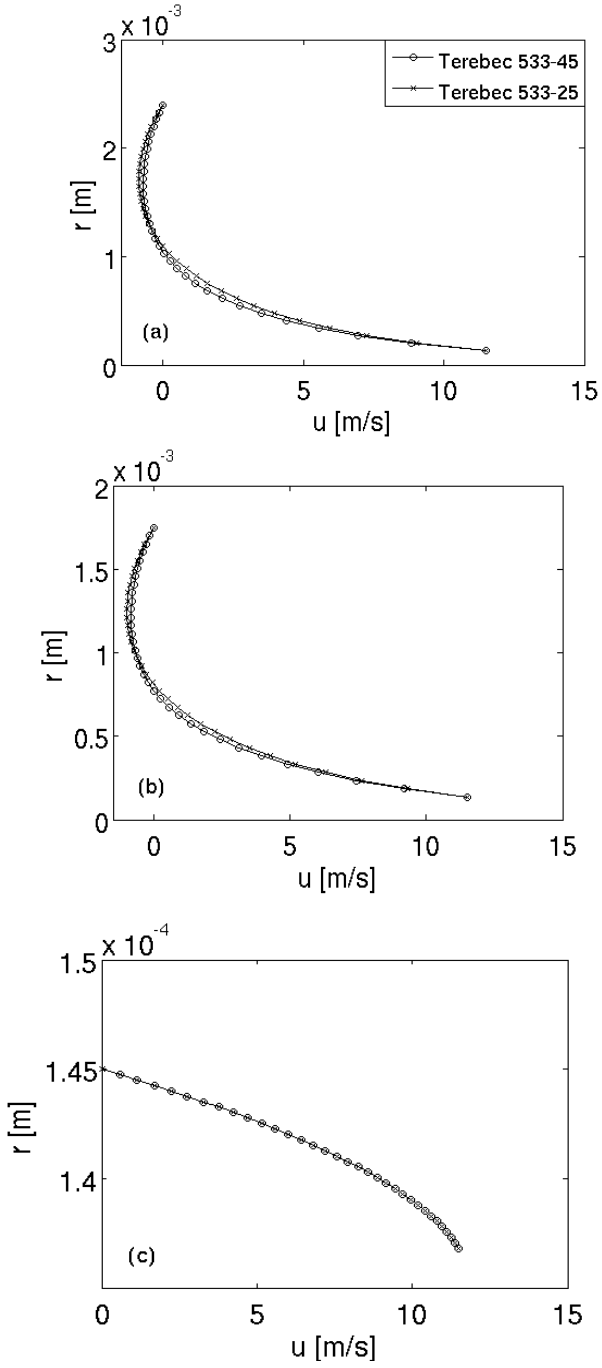

Figure 54: Velocity profiles at different cross sections, hard metal die; (a) *z*=0 mm, (b) *z*=12.5 mm, (c) *z*=25 mm

Figures 55 and 56 show the streamwise variation of the pressure and wall shear stress along the wire for the considered enamels. All profiles evidently exhibit a sharp peak at the same axial position very close to the exit. The observed magnitudes of both pressure and wall shear stress are always higher for Terebec 533-45, which can be attributed to the higher apparent viscosity of this enamel.

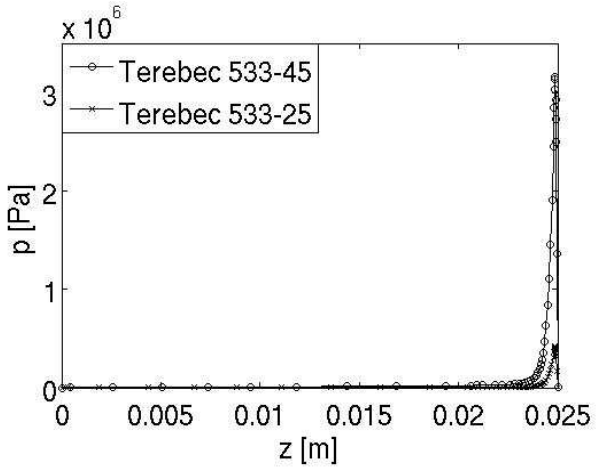

Figure 55: Streamwise variation of pressure along the wire for two considered enamels; hard metal die

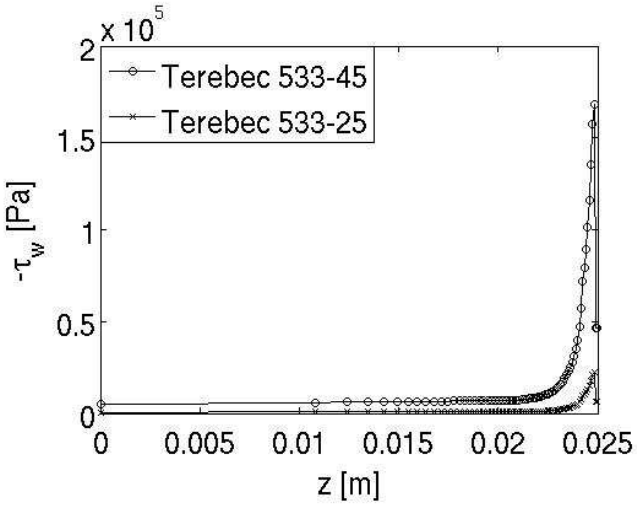

Figure 56: Streamwise variation of wall shear stress along the wire for two considered enamels; hard metal die

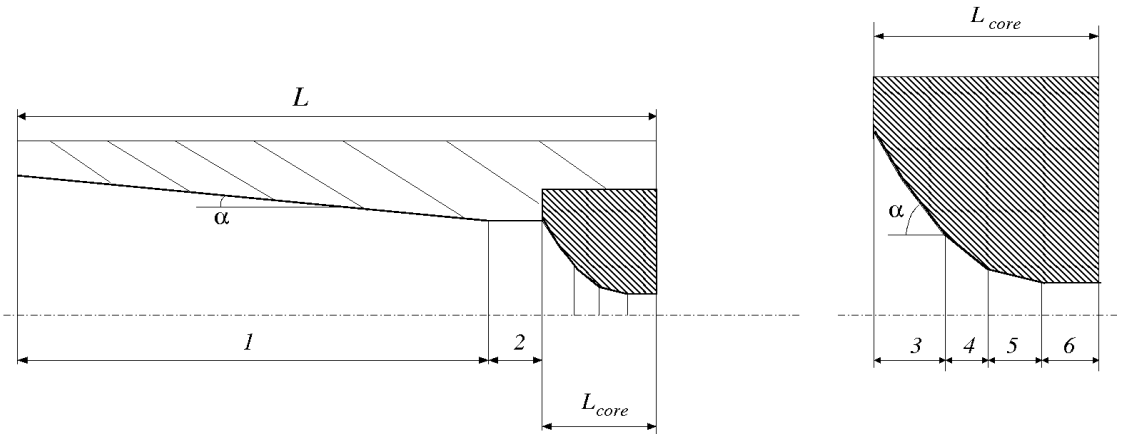

Figure 57: Subsections inside the die; hard metal die

The axial integration of the wall shear stress along the surface of the wire between the inlet and the outlet gives the total drag force which is for the case with 25% solid content enamel F_d=0.0293 N and F_d=0.2285 N for the case with 45% solid content enamel. The local generation of drag force is analyzed in more detail by evaluating the individual contributions from six subsections of the domain as specified in Figure 57. The individual subsections are evidently distinguished by the different inclination angles α of the piecewise linear radially outer contour. The contributions to the total drag force coming from each individual subsection are given in Table 13.

Table 13: Local distribution of drag force generation, hard metal dies; Terebec 533-25 and Terebec 533-45

	Subsection	1	2	3	4	5	6	Σ
Terebec 533-25	F_d [N]	0.0192	0.0014	0.0009	0.0021	0.0074	0.0009	0.0319
	Contrib. [%]	60.19	4.39	2.88	6.43	23.04	3.07	100
Terebec 533-45	F_d [N]	0.111	0.00519	0.0209	0.0247	0.06222	0.00448	0.2285
	Contrib. [%]	48.60	2.27	9.13	10.81	27.23	1.96	100

Two subsections contribute evidently most to the total drag force exerted on the wire regardless of the applied solid content in the used enamel. In subsection 1 the major part of the drag force is generated, even though the cross section available for the flow is highest in this section, which

leads to the lowest shear rates. The relatively highest contribution of this subsection is simply due its axial length which makes up almost 80% of the total length of the die. The second significant contribution to the drag force comes from subsection 5. In this region the wall shear stress is increased to a sharp peak as seen in Figure 56. Even though the axial length of this subsection is relatively small, the peak in the local shear stress still leads to a significant contribution. The results of the present analysis of the local drag force generation suggest that a possible shape optimization should be focused on the variation of these two subsections in order to obtain a significant drag force reduction.

4.2.2 Results for diamond dies

The computations consider the same operating conditions as in the case of hard metal dies, assuming again d_w=0.27 mm, U_w=11.5 m/s, and h_e=8.2 µm for the wire diameter, velocity, and exit gap height, respectively. The total length of the die is somewhat shorter than that of the hard metal die. This is due to a short diverging section at the die exit which results from the production process of the diamond core. Under the considered contact conditions the radial outer surface of this diverging exit section remains unwetted, as schematically shown in Figure 58.

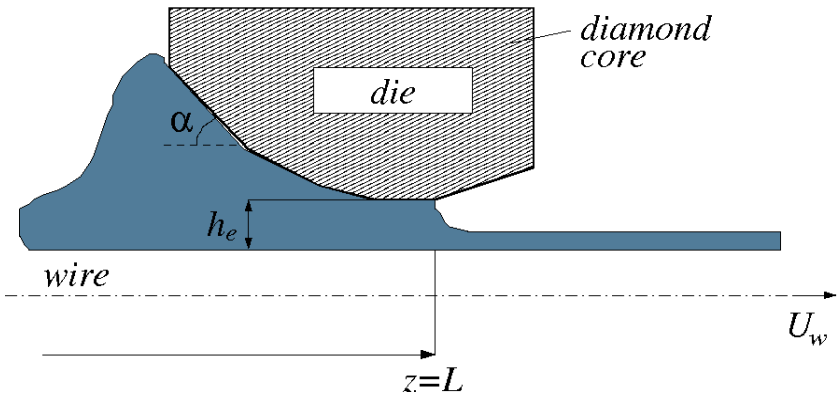

Figure 58: Detail of the diamond core with diverging exit section

This section has therefore no relevant effect on the flow field upstream and the finally obtained enamel deposition, so that it can be excluded from the computational domain leading to a somewhat shorter axial length L=24.2 mm.

Analogously to the hard metal die case the solid polymer content of the enamels was 25% and 45%. The velocity contours shown in Figure 59 provide a qualitative insight into the structure of the velocity field evolving inside the diamond die for the two considered enamels. Similar to the case of the hard metal dies the structure of the flow field exhibits also no notable difference for the considered enamels. Both cases show again the typical structure of the Couette-type flow inside converging gaps, featuring a strong reverse flow towards the inlet for continuity reason.

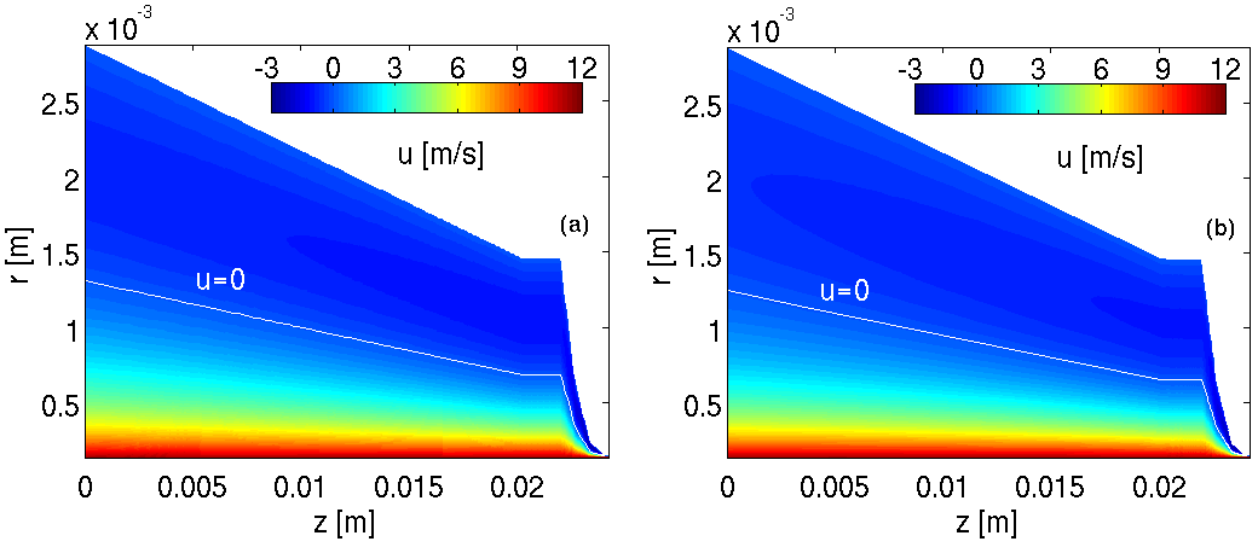

Figure 59: Velocity contours inside diamond die: (a) Terebec 533-25, (b) Terebec 533-45

A more quantitative insight into the velocity field is obtained again by comparing the velocity profiles at three different cross-sections located at the inlet, the middle, and the outlet of the die, with the axial positions z=0 mm, z=12.1 mm, and z=24.2 mm, respectively, as shown in Figure 60. Similar to the results for the hard metal dies the enamel with the higher solid content shows somewhat more bulky profiles at the two upstream positions due to the more pronounced shear thinning, while the profiles collapse at the exit cross-section.

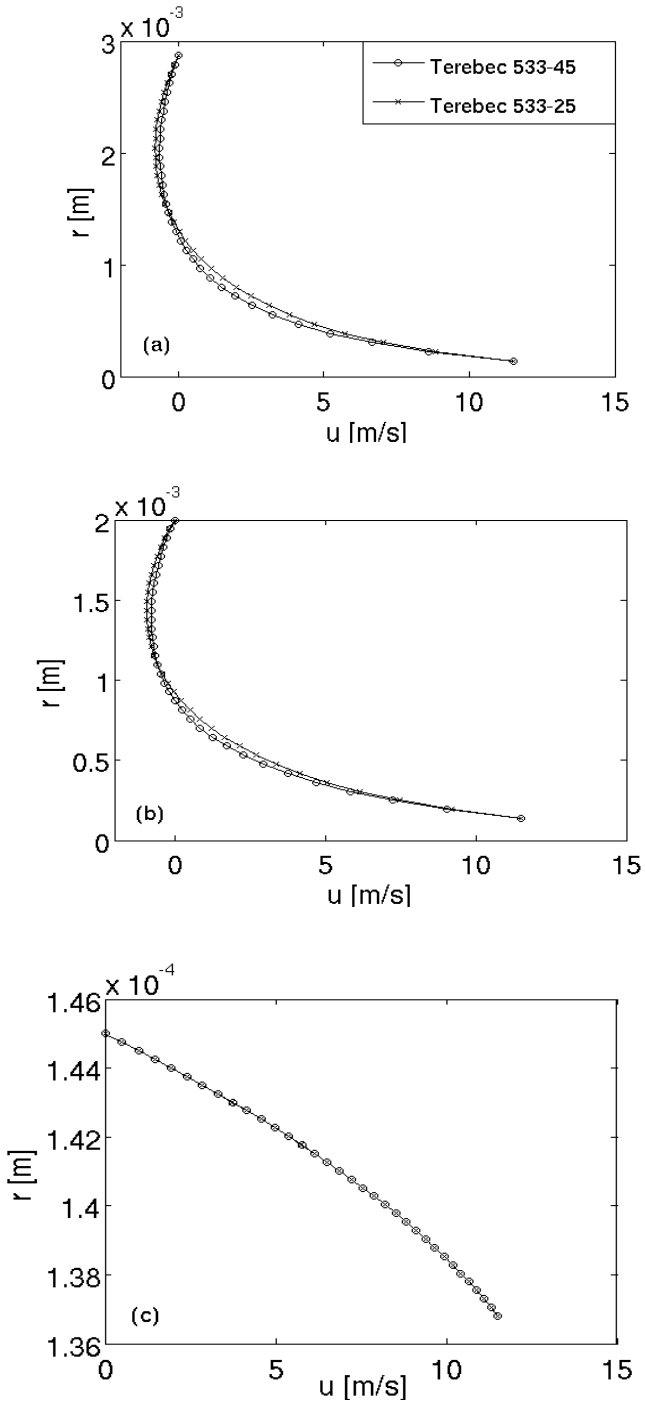

Figure 60: Velocity profiles at different cross sections, diamond die; (a) *z*=0 mm, (b) *z*=12.1 mm, (c) *z*=24.2 mm

Streamwise variations of pressure and wall shear stress are shown in Figures 61 and 62 respectively. They both exhibit a peak at close to the die exit as already observed in the case of hard metal dies. It can be seen that the peak values of both pressure and wall shear stress are higher in the case of diamond dies as compared to the hard metal dies.

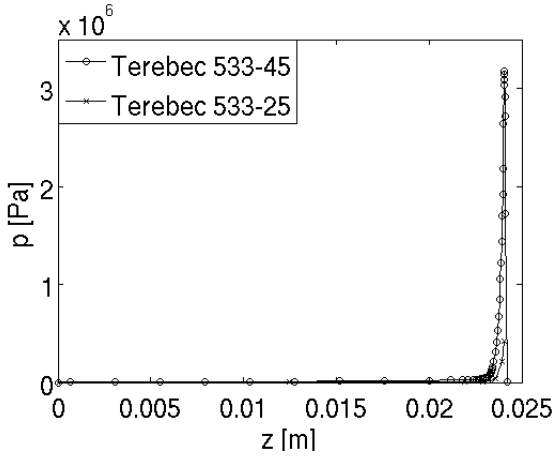

Figure 61: Streamwise variation of pressure along the wire for two considered enamels; diamond die

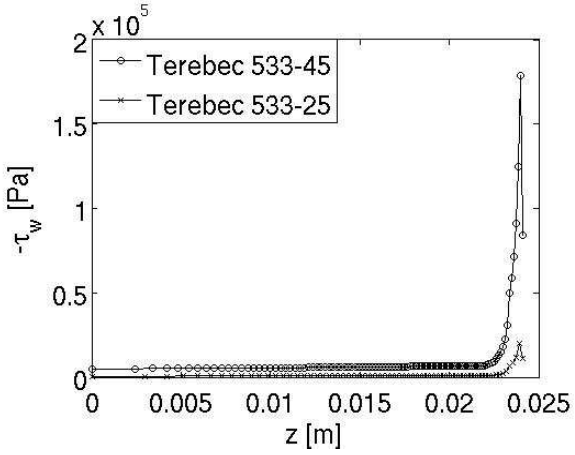

Figure 62: Streamwise variation of wall shear stress along the wire for two considered enamels; diamond die

Even though the observed peak of the wall shear stress is higher in the case of diamond dies, the integral values of the drag force computed as F_d=0.0319 N for the case with 25% solid content and F_d=0.1951 N for the case with 45% solid content are lower as compared to the drag forces computed for hard metal dies. The reason for that is that the peak shear stress region extends along a very short part of the wire, so that it does not significantly contribute to the total drag force.

Similar to the hard metal dies the diamond dies are also subdivided into individual axial subsections based on the inclination angle of the piecewise linear outer contour to analyze the local generation of drag force. The positions of the individual subsections, which are again distinguished by the different inclination angles α of the radially outer contour, are shown in Figure 63. The contribution of each individual subsection to the total drag force is listed in Table 14.

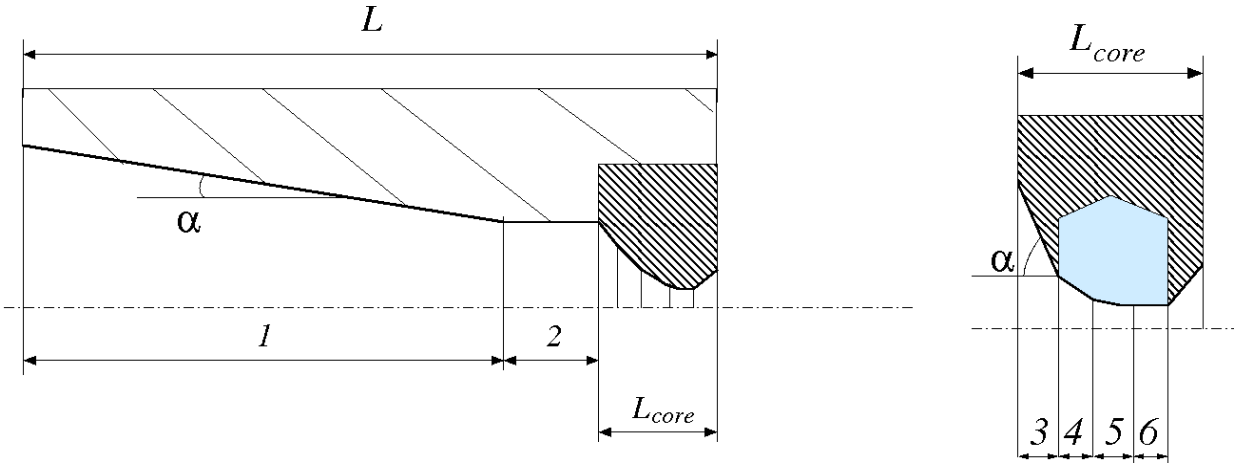

Figure 63: Subsections inside the die; diamond die

Table 14: Local distribution of drag force generation, diamond dies; Terebec 533-25 and Terebec 533-45

	Subsection	1	2	3	4	5	6	Σ
Terebec 533-25	F_d [N]	0.0174	0.00054	0.00234	0.00242	0.00625	0.00034	0.0293
	Contribution [%]	59.43	1.84	7.99	8.25	21.32	1.17	100
Terebec 533-45	F_d [N]	0.1044	0.0098	0.005	0.0123	0.0553	0.0082	0.1951
	Contribution [%]	53.55	5.03	2.56	6.29	28.35	4.22	100

As already observed in the results for the hard metal dies, the major contributions in the case of diamond dies come also from the relatively longest subsection at the inlet 1, and the most downstream converging subsection 5 immediately before the cylindrical exit section 6. A good starting point for a possible drag force reduction through optimization of the geometry could therefore lie in a modification of subsections 1 and 5.

4.3. Experimental validation of predicted drag force

Since there exists basically no experimental data on the flow induced drag forces occurring in the presently considered generalized Couette flow, it was decided to perform own measurements under real operating conditions using a specially designed experimental device. The acquired data should provide additional validation of the present analytical model, along with the already obtained numerical data from CFD simulations.

4.3.1 Experimental facility

An experimental device was specially designed to measure the drag force exerted on the wire when being pulled through the coating die. As schematically shown in Figure 64, the measurement principle is based on Newton's third law (actio=reactio). Following this principle the drag force exerted on the wire is obtained indirectly by measuring the equivalent counter

force which holds the die in place. The counter force is measured using a ring force transducer placed between the die carrier and the support. This setup allows for a measurement of the drag force without perturbing the coating process.

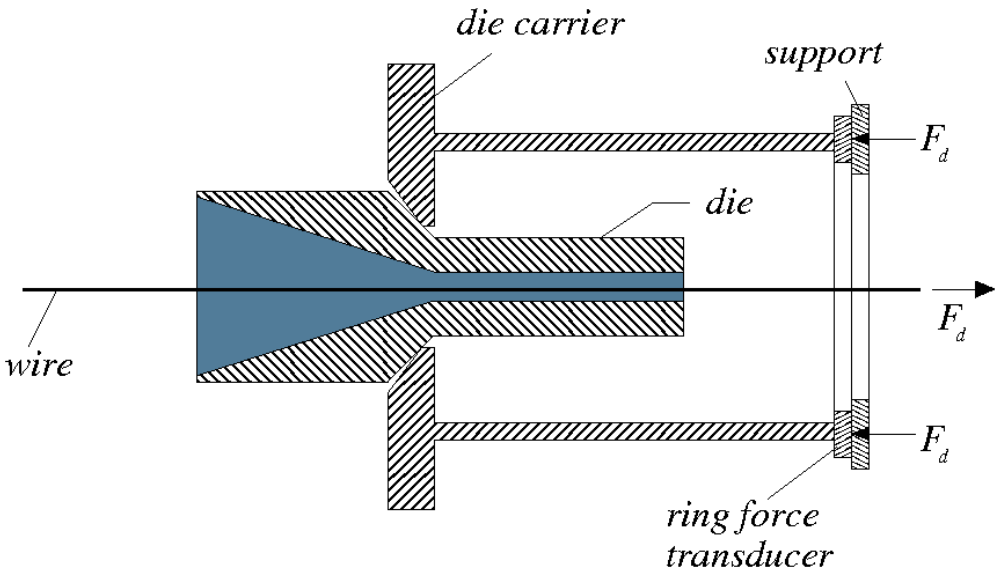

Figure 64: Measurement device operating principle

The ring force transducer is basically a piezo-electric annular pressure sensor. It is illustrated in Figure 65.

Figure 65: Ring force transducer

Based on the analytical computations the expected magnitudes of the hydrodynamically induced drag forces are relatively low. Therefore, a sensor covering the range of relatively small forces up to 10 N was chosen. The accuracy of this measuring device is 1% of the maximum measured

value, which corresponds to 0.1 N. A meridional cross section through the finally realized measuring device is displayed in Figure 66.

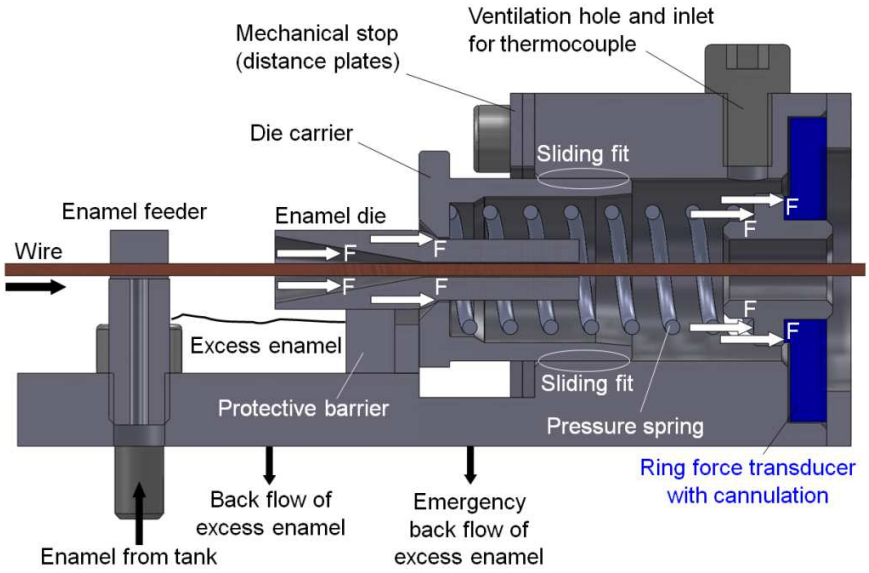

Figure 66: Meridional cross section through the measuring device

It can be seen that the die carrier is not rigidly connected with the ring force transducer, but with a spring in between. This spring elastic, hence compressible, connection protects the transducer from a possible mechanical overload during measurements due to some unforeseen forces. The opening above the ring force transducer allows for a monitoring of the enamel temperature, if necessary, using a thermocouple. Due to its relatively small dimensions the device can be mounted at any die within the die set arrangement.

4.3.2 Measured drag forces compared against computational results

The measurements were performed on a real production machine using an arrangement of ten diamond dies, where only basecoat enamel with 45% solid content was successively deposited on a wire with a bare wire diameter $d_{w,0}$=0.25 mm. Two devices for measuring the drag force were mounted at the first and the last pass. The first pass was chosen, because there it is easy to

determine the gap height at the die exit, since there is no enamel deposited yet on the surface of the oncoming wire. The oncoming solid deposition height ahead of the last pass was determined assuming a uniform enamel deposition per each pass and taking into account the accumulated losses of solid content appearing during the drying and curing steps. The measurements were started after stringing in the wire into the machine. The velocity of the wire was gradually increased towards the final production velocity U_w=690 m/min, as it is generally done for the considered wire diameter to provide the required residence time in the oven during the heat up. The velocity of the wire was further increased up to 1200 m/min, which represents almost twice the production velocity typically used for the processed wire diameter d_w=0.25 mm. This substantial increase of the wire velocity far above typical setting in production did still not lead to any breakage of the wire.

Figure 67 shows the drag force which was measured at the last die of the die set arrangement for the different wire velocities. The corresponding predictions of the analytical model are included for validation as well. The computational predictions lie evidently always well within the uncertainty range of the measurements. The measurements do not clearly exhibit the same essentially linear dependence of the wire velocity as seen in the analytical results. In the present flow configuration non-linearity mainly resides in the non-Newtonian stress-strain dependence. However, due to the extremely high shear rates the fluid effectively behaves as Newtonian near the wire, so that the experimentally observed deviation from linearity should be rather attributed to an inaccuracy in the measurements.

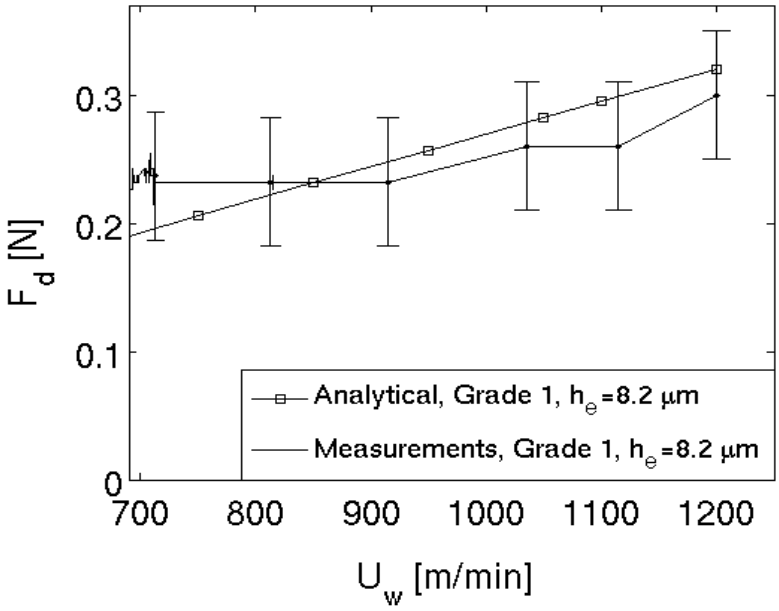

Figure 67: Comparison between computations and measurements

4.4 Discussion of possible reasons for deformation and breakage of the wire

The computational analysis of the flow inside the hard metal and diamond dies yielded very similar drag forces for both types. Using these drag forces and the cross section of the bare wire with the diameter $d_{w,0}$, Eq. (91) yields for the enamel with 25% solid content mechanical tensile stresses σ_{wire}=0.65 N/mm^2, and σ_{wire}=0.6 N/mm^2 for the hard metal and diamond dies, respectively. For the enamel with solid content of 45% the tensile stress is increased to σ_{wire}=4.65 N/mm^2 in the case of hard metal dies, and to σ_{wire}=4 N/mm^2 in the case of diamond dies. For all considered cases the computed tensile stresses remain evidently well below the limit of plastic deformation of pure copper σ_{02}=70 N/mm^2.

Even though the drag force generated inside a single die is apparently too small for producing any significant plastic deformation of the wire, it is still possible that the drag force is accumulated in the successively passed dies to finally reach a critically high level for deformation. Additionally, the observed fairly low levels of drag forces may still be sufficient to cause a so called low stress elongation (LSE), where a microstructural change of the wire

material is induced by the stresses considerably lower than the yield stress limit of plastic deformation. This phenomenon is even more relevant, when the stressed wire enters the oven for drying and curing due to its exposure to highly elevated temperatures.

Despite the possible relevance of the flow induced drag force for an undesired change in the microstructure of the material and even plastic deformation the resulting tensile stresses will most unlikely exceed the ultimate tensile stress of copper σ_{UTS}=200 N/mm^2 even in a worst-case scenario. Thus, the flow induced drag force can be excluded as a possible reason for wire breakage. The fact that the tests with diamond dies did not lead to any wire breakage, even when strongly exceeding typical production velocities, suggested to look for other possible reasons for the reported wire breakage in the case of hard metal dies. Since the calibration section made of hard metal can be manufactured with considerably lower geometrical accuracy than those made of diamond, the expectedly stronger deviations from the perfect target geometry appeared as most likely alternative reason for wire breakage. The effect of such geometrical imperfections on the coating was therefore investigated in more detail, as will be shown in the following subsection.

4.4.1 Die imperfections

Deviations from the target geometry may have different reasons. They can be introduced during the production process, or, they may be caused by the wear of the die occurring during a longer period of application. A faulty die geometry inevitably leads to a faulty deposition of enamel on the wire surface, which can further accumulate, when the wire passes through a sequence of dies. The computational model developed in the present work was used to investigate the influence of a faulty die geometry on the deposition. The computations considered three different scenarios which are representative for an imperfect geometry. The respective cross sections are shown in Figure 68.

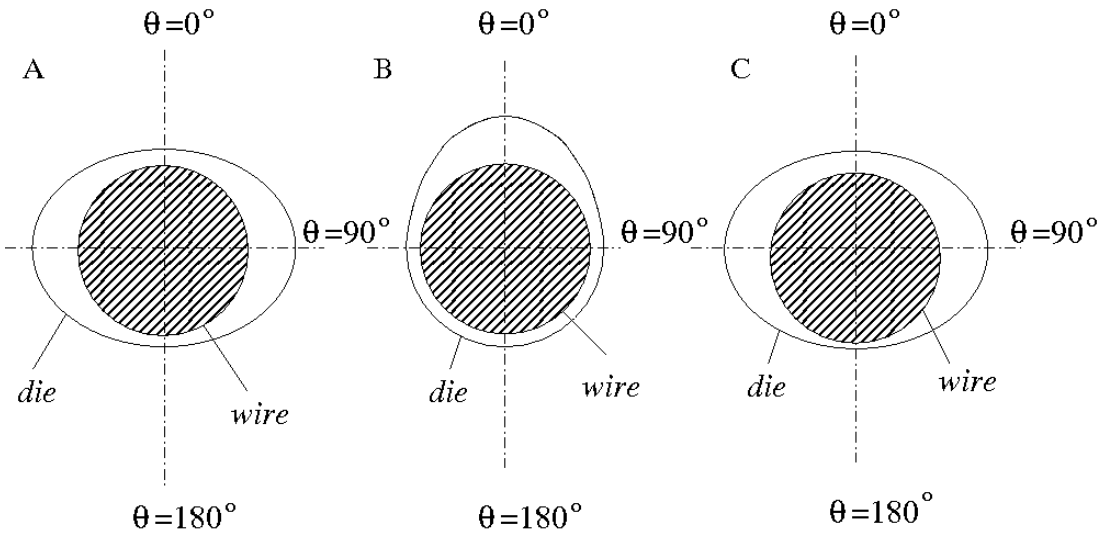

Figure 68: Considered die imperfections

Case A represents a symmetric deviation from the perfectly round die shape, resulting in an oval shape of the die exit cross section. Case B represents an asymmetric deviation, where the lower part of the exit cross-section is concentric with the wire, while the upper part has an oval shape. In Case C the exit cross-section has the same symmetric oval shape as in Case A, but the position of the wire is eccentric. The effective gap heights at different circumferential positions are shown for the individual cases in Table 15. The considered geometrical imperfections only affect the cylindrical calibration section at the die exit. The eccentric position of the wire assumed as 1 µm in Case C axially extends through the whole domain. The perfect reference geometry, from which the imperfect cases deviate, is associated with an axisymmetric exit gap height h_e=8.2 µm. The diameter and velocity of the wire are assumed as d_w=0.27 mm and U_w=11.5 m/s, respectively.

Table 15: Gap height h_e at selected circumferential positions of the exit cross section

h_e [µm]	Θ=0°	Θ=90°	Θ=180°
Case A	8.2	10.2	8.2
Case B	9.42	8.198	8.98
Case C	9.2	10.3	7.2

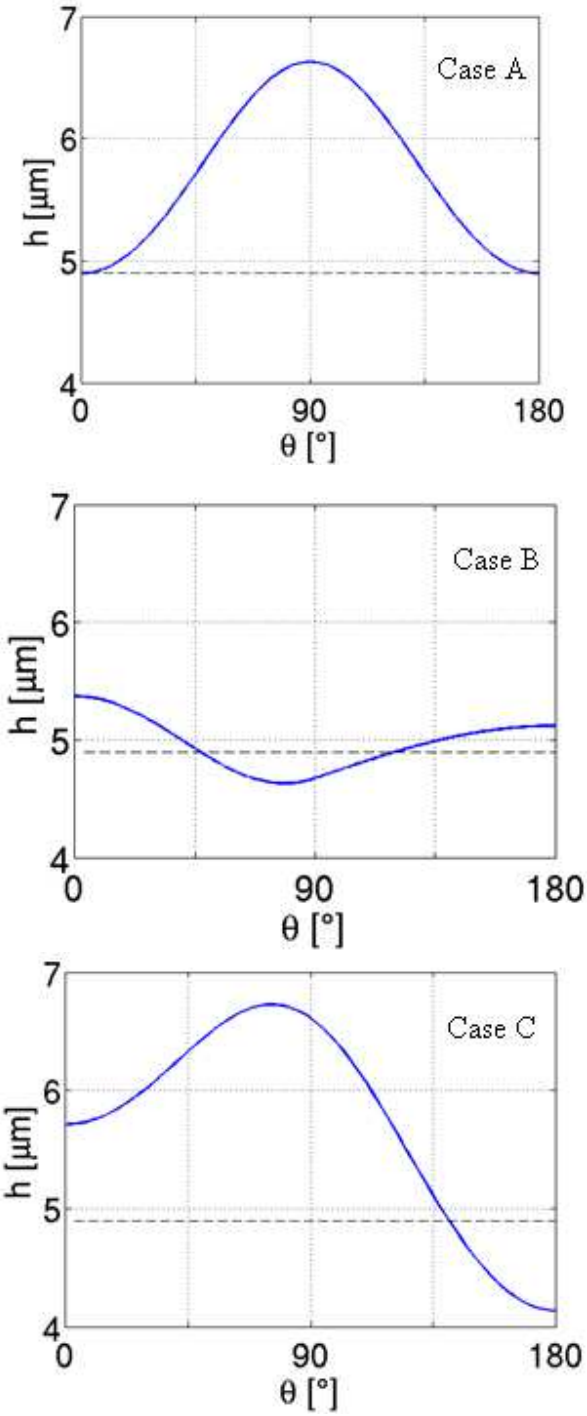

Figure 69: Influence of the geometry on enamel deposition, the deposition height of the perfect reference geometry denoted by the dashed line

Figure 69 shows the circumferential variation of the deposition height as predicted for the different cases. As one might expect, the obtained variations of the deposition height follow clearly the circumferential variations of the exit gap height due to the imperfect geometries. Case C turns out as the most critical scenario, as the deposition height exceeds here most significantly the target value. It has to be emphasized that the faults in the deposition height can accumulate, when the wire is passed through successive dies having also imperfect geometries in the calibration section. This may finally lead to a solid contact between the coating, which has already been deposited and solidified in previous die passes, and the surface of the die, as schematically shown in Figure 70. Such a solid contact between the thin wire and the die at the typically high production velocity will inevitably lead to wire breakage.

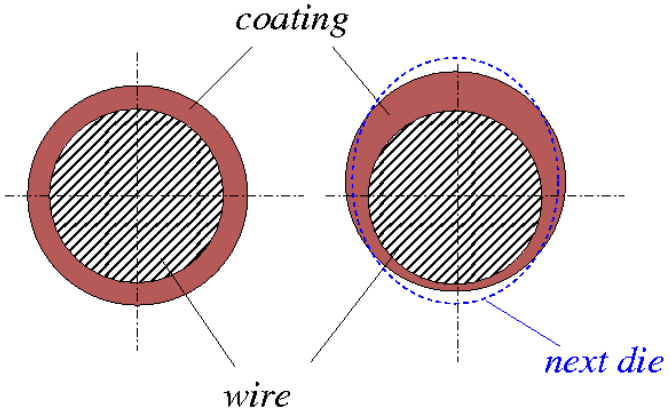

Figure 70: Example of a possible solid contact between the die and wire

The present analysis helps to explain, why the wire breakage mainly occurs when using hard metal dies. The geometries of the calibration section of these dies can be manufactured with markedly lower accuracy than it is achieved with diamond dies, so that the imperfections in the geometry are the most likely reason for wire breakage. In order to rule out this shortcoming as much as possible the proposed new die designs discussed in chapter 5 considered therefore only dies with diamond cores, because only these can be manufactured with the required geometrical accuracy as needed for future application with further increased solid content and production velocities.

5. NEW DIE DESIGNS

5.1 Motivation and reasoning

Even though the flow induced drag forces turned out to be too small for breakage of the wire, a reduction in total drag force is still beneficial in the light of the expected advances in the operating conditions. The availability of enameling dies, which generate lowest possible drag forces, gives room to substantially increased production velocities and solid mass contents without the hazard of an undesirable permanent elongation of the wire in the heated zone of the oven. Finally, some of the suggested modifications of the geometry may simplify the production process of the die, which would lower their price. The relatively high price is especially an issue for the diamond dies, due to the expensive material, but also due to the sophisticated multi-step manufacturing.

5.2 Proposed designs and computational analysis

Three different modifications of the currently used design of the dies with a diamond core were proposed. The modifications are based on the analysis of the computed flow field revealing the local generation of drag force as well as inputs from the manufacturer of the dies. The latter ensured that the proposed designs can be practically realized at acceptable, or better, reduced production costs as compared to the current design. The current and the proposed designs together with their salient geometrical modifications are listed in Table 16. Following the analysis of the local drag force generation in the current die design (see Table 14) the focus of the modifications was put on the subsections 1 and 5. After discussions with the die producer, it was seen that a modification of the geometry of subsection 5 was not possible without extensive investment into the development of specialized tools required for its production. It was therefore decided to keep the inner contour of the diamond core unchanged, and modifying only the axial position of the core and the geometry of subsection 1. As seen from the sketch in Figure 72 the core of the design AK1 is axially shifted towards the very end of the die, so that the axial ends of

the steel body and the diamond core are in plane. This modification was not proposed for drag force reduction reason but rather for reduction of production costs.

Table 16: Proposed geometry variations

Design	Description
AK0	Currently used die geometry
AK1	Calibration region shifted towards exit
BK0	Reduction in the inlet section length
BZ0	Reduction in the inlet section length and change from conical to cylindrical inlet geometry

In the design BK0 shown in Figure 73 the conical inlet section (= subsection 1) is strongly reduced in length. The diameter of the inlet D_{in} is still left unchanged leading to an increase in the cone-angle of the axial contraction. The design BZ0 shown in Figure 74 features the same reduced axial length of the inlet subsection 1 as the design BK0, but its shape is changed from conical to cylindrical. This modification was again mainly motivated by savings in production costs, as cylindrical holes can be produced at much lower costs than conical ones.

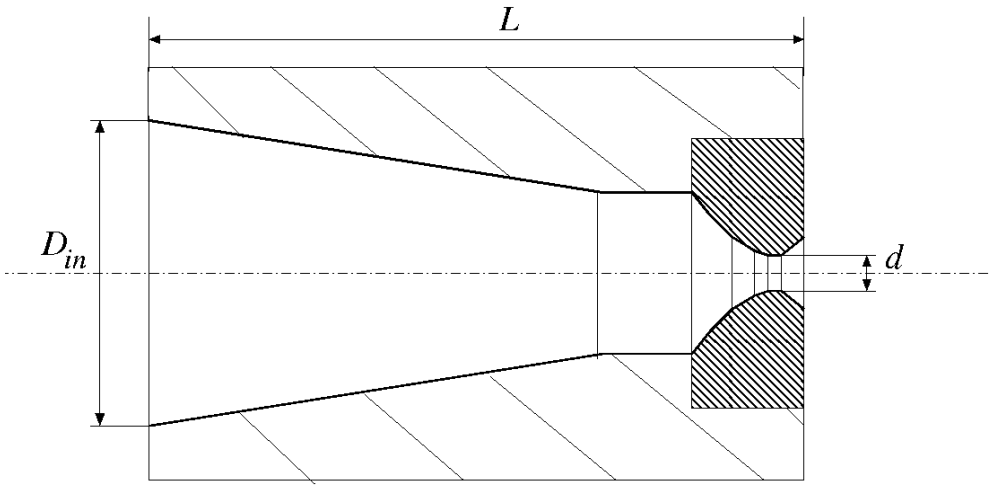

Figure 71: Geometry AK0

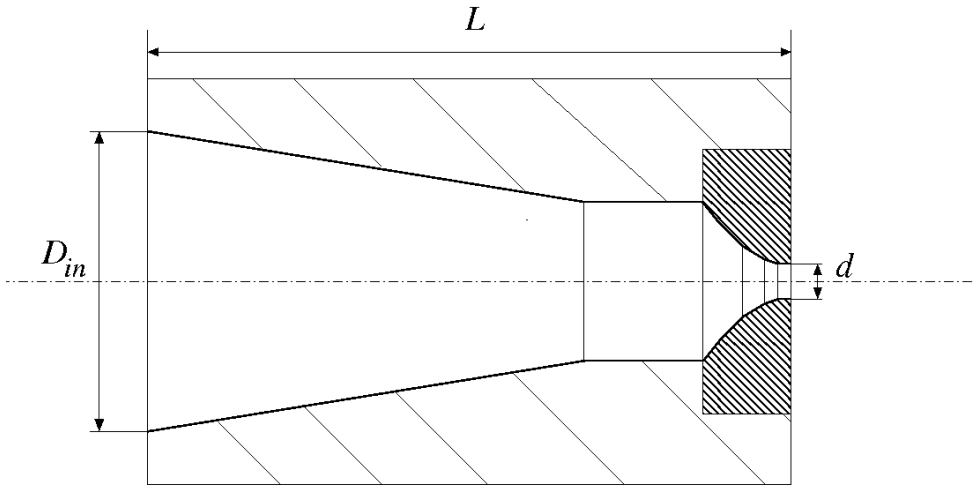

Figure 72: Geometry AK1

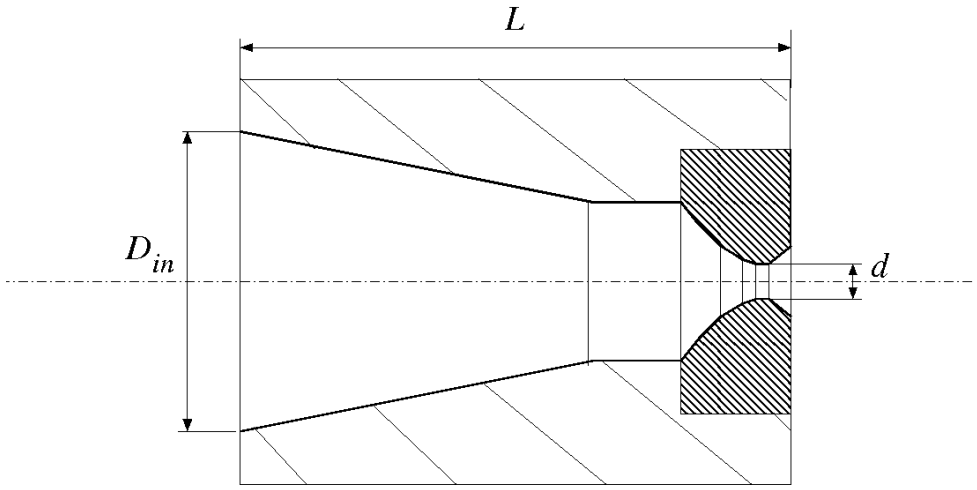

Figure 73: Geometry BK0

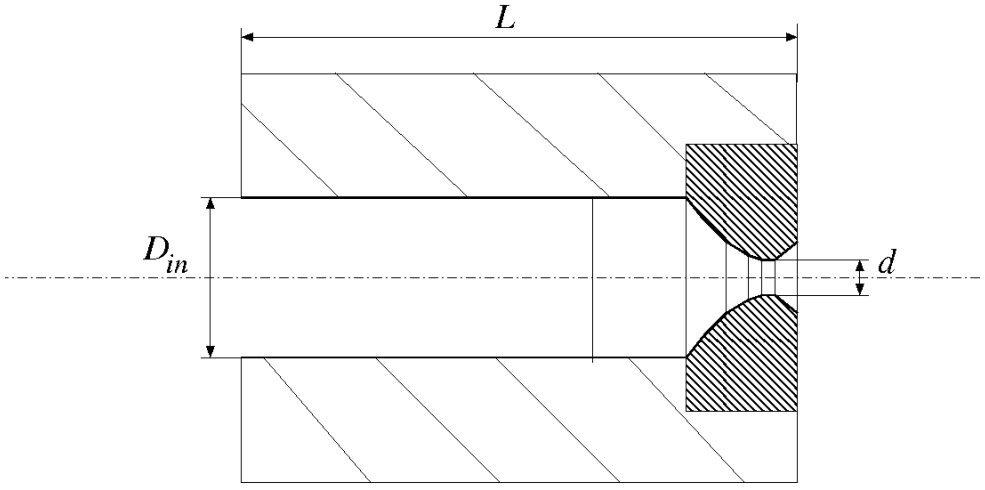

Figure 74: Geometry BZ0

The effect of the geometry modifications on the flow field inside the die and the resulting drag force was computationally investigated using the analytical model. The calculations were carried out for the basecoat with 45% solid content using again the experimentally based Carreau-Yasuda flow curve shown in Figure 53 (b). Analogously to the computations already performed for the currently applied die geometry the wire diameter and velocity were assumed as d_w=0.27 mm, and U_w=11.5 m/s, respectively. The exit gap height was set to h_e=8.2 µm.

The computationally obtained non-dimensional axial variations of the pressure and shear stress along the wire are shown in Figures 75 and 76, respectively, where the reference scales only differ in the axial length scale *L*. The peak in the pressure near the exit does evidently not vary significantly, which is due to the fact that the geometry of die core at the exit was not modified. However a notable increase in pressure can be observed in the inlet section of the die due to the reduction in the length of subsection 1, and, more pronouncedly, due to a change from a conical to a cylindrical shape.

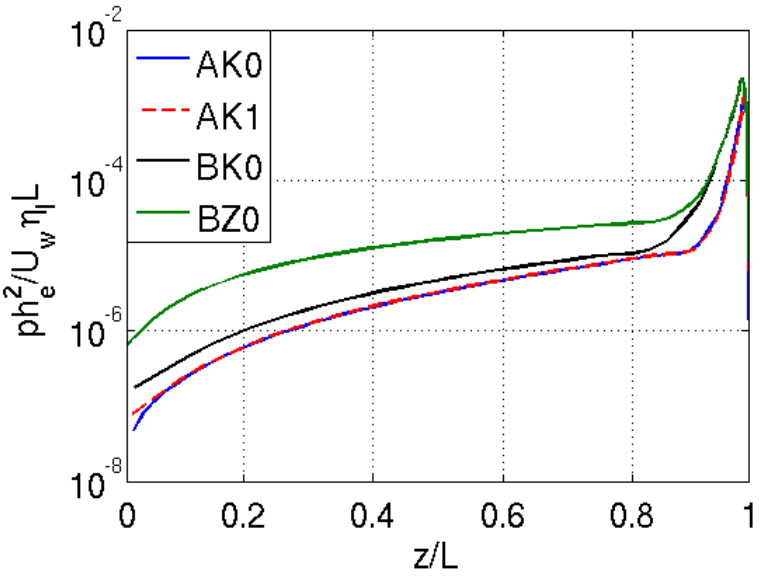

Figure 75: Axial variation of pressure along the wire

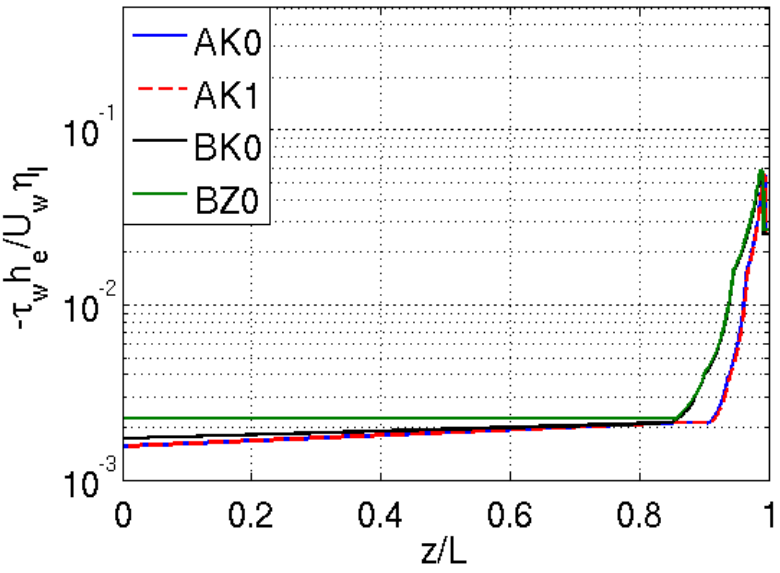

Figure 76: Axial variation of wall shear stress along the wire

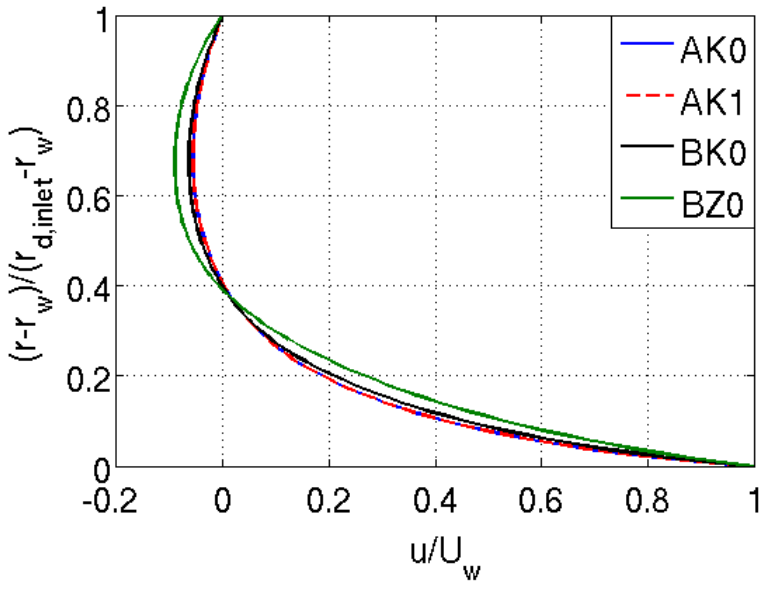

Figure 77: Velocity profiles at the die inlet

The tendencies observed for the pressure are also seen in the axial variations of the wall shear stress. The shortening and the change from conical to cylindrical shape of the inlet section (subsection 1) leads to an increase in shear stress in the inlet region, while the peak near the exit essentially remains the same. Table 17 shows the total drag forces and the relative contributions of the individual subsections resulting from the axial variation of the shear stress along the wire. The shortening of subsection 1 brings about 25% reduction in drag force for the design BK0 and a little bit less for BZ0. The constantly narrower gap height associated with the cylindrical shape apparently increases the general magnitude of shear stress as compared to the conical gap of BK0, which translates into a higher generation of drag force in subsection 1 observed for BZ0. A further concern was related to a possible increase in the intensity of the backflow, which may arise with the shortening of the inlet section and the reduction of the annular cross section between the wire and the die near the inlet in the case BZ0. The resulting higher kinetic energy of the backflow would expectedly enfavour a very fast breakup of the ejected liquid lamella into small droplets leading to undesirable effects like cross contamination. Using the velocity profiles obtained at the inlet cross-section (z/L=0), as shown in Figure 77, the rates of the ejected kinetic energy can be computed as

$$\dot{E}_{kin} = 2\pi \int_{r_w}^{r_d} \rho u \frac{u^2}{2} r dr. \qquad (113)$$

As seen from the last column in Table 17, the rate of the ejected energy is not significantly increased for the shortened die with the conical shape of the inlet section (BK0), while it is even decreased for the cylindrical inlet section (BZ0). These results suggest that both the shortened geometries will not lead to a more rapid fragmentation of the continuous liquid backflow.

Table 17: Local generation of drag force and rates of kinetic energy ejected at the die inlet

Design	**Subsection**						F_d **[N]**	E_{kin} **x10^6 [W]**
	1	2	3	4	5	6	Σ	
AK0	53.55%	5.03%	2.56%	6.29%	28.35%	4.22%	100%	6.047
	0.1044	0.00981	0.00499	0.0123	0.05531	0.00823	0.1951	
AK1	52.18%	7.58%	2.43%	6.08%	27.62%	4.11%	100%	6.326
	0.1046	0.01519	0.00487	0.0122	0.05335	0.00824	0.2004	
BK0	41.61%	6.23%	3.14%	7.87%	35.8%	5.34%	100%	6.711
	0.063	0.00944	0.00476	0.0119	0.0542	0.00809	0.1515	
BZ0	44.65%	6.63%	3.03%	7.36%	33.38%	4.95%	100%	5.736
	0.0736	0.0109	0.005	0.0121	0.05501	0.00816	0.1648	

The present analysis outlines possible gains for the magnet wire coating process yielded by relatively simple modifications of the die geometry. As seen from Table 17 the modifications affecting both the length and angle of subsection 1 lead to the most significant reduction in the hydrodynamically induced drag force of up to 25%. Based on the computed magnitudes of the kinetic energies ejected with the backflow at the die inlet, possible negative effects like cross contamination due to the intensified backflow turned out as very unlikely. Aside from the drag force reduction, the proposed shortening and simplification of the geometry of the subsection 1 leads to a reduction in the manufacturing costs of the dies, reducing their total price.

6. SUMMARY AND CONCLUSIONS

The flow evolving inside wire enameling dies applied in the production of electrically insulated magnet wires was computationally investigated. The analysis should help to identify possible flow related reasons for the appearance of wire hardening due to plastic deformation, or in extreme cases even wire breakage, as frequently reported by magnet wire producers. For the mathematical description of the generalized Couette flow typically met in this coating application an analytical model was developed based on the lubrication theory approximation of the Navier-Stokes equations. The developed model does also account for non-Newtonian behavior of the working fluid and heat transfer, which allows investigating the effect of different rheological properties in terms of shear thinning or shear thickening on the flow and temperature fields as well. The computational analysis was applied to a wide range of generic converging die geometries following a generalized cosine-type shape as well as real die geometries currently used in the production.

Due to the lack of experimental data on the flow field inside the considered narrow gaps, a detailed validation of the analytical predictions had to rely mainly on a comparison against numerical results obtained from CFD. The analytically predicted flow field showed generally very good agreement with the numerical data. Some deviations appeared mainly at axial positions associated with a strong contraction of the annular cross-section. More significant discrepancies were observed in the prediction of the temperature field for larger Prandtl numbers. These observed deficits clearly illustrate the limits of the lubrication theory due to the total neglect of advective transport, especially when applied to strongly converging die geometries and fluids with high Prandtl number. The lubrication theory based model was therefore extended by first-order perturbations accounting for the advective transfer in both the momentum and energy equations for the case of a Newtonian fluid. In a comprehensive comparison against CFD results the proposed first-order extension was proven to yield a significant gain in accuracy. Especially the convective redistribution of viscous heat, which is increasingly important for higher Prandtl numbers, was shown to be captured considerably well by the extended model. Less pronounced improvements were observed for the predicted velocity field, which is already

described reasonably well by the zeroth-order (non-extended) base model. The total neglect of the advective (inertia) terms appears to be less critical for the solution of the momentum transfer. Aside from a more accurate prediction of the local variation of the velocity and, particularly, the temperature, the proposed first-order extension was also proven to describe better the global balances of momentum and heat as compared to the zeroth-order base model.

A special device was designed for measuring the total drag force on the wire when being passed through an enameling die under real production conditions. In the view of the very limited access of standard flow measuring techniques to the considered flow configuration these measurements provided at least some experimental validation data for this certainly only global, but still important, output quantity. The comparison of the measured total drag forces against the results obtained from the zeroth-order model for a real die geometry and real shear-thinning enamels showed very good agreement.

The computed, and experimentally validated, levels of drag force were, even for the very viscous enamels with high solid content, always much lower than the yield strength of copper, so that they could lead at most to some plastic deformation of the wire due to effect of force accumulation along the die set, but certainly not to the observed wire breakage. Since wire breakage never occurred in the test runs with diamond dies, geometrical deviations from the perfect target shape, which are inherently larger for the hard metal dies due to the manufacturing process, could be identified as most probable alternative reason for wire breakage. Using the present analytical model the detrimental effect of some typical geometrical imperfections could be demonstrated. The predicted faulty, in particular non-uniform circumferential deposition of enamel may further accumulate in the successive die passes leading finally to solid contact between the fast moving wire surface and the die contour.

The analytical predictions of the flow field inside real dies provide also a valuable insight into the local generation of drag force, which allows identifying the most critical regions of drag force production, as a useful starting point for the development of flow optimized die shapes. Possible improvements of the die design were proposed and computationally analyzed using the present analytical model. The proposed modifications yielded a reduction in total drag force up to about 25%. More significant reductions could be achieved assuming generic cosine-type die

shapes with a very steep axial contraction close to the exit. The technical realization of these geometries is however limited due to the specific properties of the applied materials and requirements of the manufacturing process.

Enameling dies producing lowest possible total drag force on the wire remain desirable in the view of ongoing and future trends in the magnet wire production. Low flow induced drag forces give room for increasing the production velocity of the wire, resulting in an increased productivity of the machine. They further allow for the application of enamels with high polymer content, reducing the costs of the expensive solvent, as well as for solid content constituted by longer polymer molecules, reducing the polymer stack loss during the drying and curing process. Finally a modified die design associated with smaller dimensions or simpler geometries can translate into lower production costs as well. The comprehensive and reliable description of the flow and temperature fields provided by the presently developed analytical model delivers important input to reach these goals.

BIBLIOGRAPHY

ANSYS, 2011. ANSYS Fluent user guide, release 14.0

H. A. Barnes, J. F. Hutton, K. Walters, 1989. An Introduction to Rheology, Rheology Series, Vol. 3, Elsevier, Amsterdam

H. A. Barnes, 2000, Handbook of Elementary Rheology, Institute of non-Newtonian fluid mechanics, University of Wales

R. B. Bird, R. C. Armstrong, O. Hassager, 1987. Dynamics of polymeric liquids, Wiley-Interscience, New York

R. B. Bird, P. J. Carreau, 1968. Chem. Eng. Sci., vol. 23, 427

S. Bruin, 1972. Temperature distribution in Couette flow with and without additional pressure gradient, International Journal of Heat and Mass transfer, Vol. 15, 341-349

J. F. Carley, T. Endo, W. B. Krantz, 1979. Realistic Analysis of Flow in Wire-Coating Dies, Polymer Engineering and Science, Vol. 19, 1178-1187

R. P. Chhabra, J. F. Richardson, 2008. Non-Newtonian Flow and Applied Rheology, 2nd edition, Butterworth-Heinemann, Oxford

Chhabra, R. P., 2010. Non-Newtonian Fluids: An Introduction, SERC School-cum-Symposium on Rheology of Complex Fluids, Indian Institute of Technology, Chennai, India

D. Collins, M.D. Savage, C.M. Taylor, 1986. The influence of fluid inertia on the stability of a plain journal bearing incorporating a complete oil film, Journal of Fluid Mechanics, vol. 168, 415-430

M. M. Cross, 1965. Rheology of non-Newtonian fluids: A new flow equation for pseudoplastic systems, Journal Colloid Sc., vol. 20, 417

K. Czaputa, 2009. Steigerung der Produktivitaet und Wirtschaftlichkeit von Maschinen zur Beschichtung von duennen Draehten, Ph.D Thesis, Graz University of Technology

J.F. Dijksman, E. P. W. Savenije, 1985. The flow of Newtonian and non-Newtonian liquids through annular converging regions, RheologicaActa 24, 105-118

M. P. Escudier, P. J. Oliveira, F. T. Pinho, S. Smith, 2002. Fully developed laminar flow of non-Newtonian liquids through annuli – comparison of numerical calculations with experiments, Experiments in Fluids, 101-111

A. D. Fitt, C. P. Please, 2000. Asymptotic analysis of the flow of shear-thinning foodstuffs in annular scraped heat exchangers, Journal of Engineering Mathematics 39, 345-366

Fluent 6.3, UDF manual, 2006., Fluent Inc., Lebanon NH

R. W. Flumerfelt, M.W. Pierick, S. L. Cooper, R. B. Bird, 1969. Generalized plane Couette flow of a non-Newtonian fluid, Ind. Eng. Chem. Fundam. 8(2), 354-357

H.Giesekus, 1994. Phaenomenologische Rheoligie: Eine Einfuehrung , Springer-Verlag, Berlin

Z. Haobo, F. Honghai, Z. Yinghu, P. Qi, 2014. A new utility calculation model for axial flow of non-Newtonian fluid in concentric annuli, The Canadian Journal of Chemical Engineering, Vol 92. 945-952

J.-H. He, 2004. Variational principle for non-Newtonian lubrication: Rabinowitsch fluid model, Applied Mathematics and Computation 157, 281-286

J. L. Hudson, S. G. Bankoff, 1965. Heat transfer to a steady Couette flow with pressure gradient, Chemical Engineering Science 20, 415-421

A. M. Hull, J. R. A. Pearson, 1984. On the converging flow of viscoelastic fluids through cones and wedges, Journal of Non-Newtonian Fluid Mechanics, Vol. 14, 219-247

J. A. Jimenez, M. Kostic, 1994. A novel computerized viscometer/rheometer, Review of Scientific Instruments, Vol. 65, 229-241

A. Kandasamy, K. P. Vishwanath, 2007. Rheodynamic lubrication of a squeeze film bearing under sinusoidal squeeze motion, Computational and Applied Mathematics, Vol. 26, No. 3, 381-396

S. Kumar, S. Kumar, 2009. A Mathematical Model for Newtonian and Non-Newtonian Flow through Tapered Tubes, Indian Journal of Biomechanics: Special Issue, 191-195

S. Matsuhisa, R. B. Bird, 1965. Analytical and numerical solutions for laminar flow of non-Newtonian Ellis fluid, A. I. Ch. E. Journal Vol. 11, 588-595

S. U. Li, J. Gainer, 1968. Diffusion in Polymer solutions, I & EC Fundamentals, vol. 7

S. H. Lin, C. C. Hsu, 1980. Generalized Couette flow of a non-Newtonian fluid in annuli, Ind.

Eng. Chem. Fundam. , 421-424

S. H. Lin, D.M. Hsieh, 1980. Heat transfer to generalized Couette flow on non-Newtonian fluid in annuli with moving inner cylinder, J. Heat Transfer, Trans. ASME 102, 789-790

S. H. Lin, 1979. Heat transfer to plane non-Newtonian Couette flow, Int. J. Heat Mass Transfer, Vol. 22, 1117-1123

S. H. Lin, 1992. Heat transfer to generalized Couette flow on non-Newtonian fluid in annuli with moving outer cylinder, Int. J. Heat Mass Transfer, Vol. 35, 3069-3075

K. W. Linert, 1995. Investigation of the Curing Reaction Mechanism of Polyester and Polyesterimide Wire Enamels, Proceedings: Electrical Manufacturing and Coil Winding Conference, Rosemont, Illinois, USA

K. W. Linert, 1999. Poly(ester-imide)s for industrial use, Advances in polymer science, Springer, Berlin

C. W. Macosko, 1994. Rheology: Principles, Measurements and Applications, VCH, New York

P. K. Mandal, 2005. An unsteady analysis of non-Newtonian blood flow through tapered arteries with a stenosis, International Journal of Non-Linear Mechanics, Vol. 40, 151-164

E. Mitsoulis, 1986. Fluid Flow and Heat Transfer in Wire Coating: A Review, Advances in Polymer Technology, Vol. 6, 497-487

A. Nessil, S. Larbi, H. Belhanche, M. Malki, 2013.: Journal Bearings Lubrication Aspect Analysis Using Non-Newtonian Fluids, Advances in Tribology, 1-9

S. Oka, 1973. Pressure development in a non-Newtonian flow through a tapered tube, Biorheology, Vol. 10, 207-212, Pergamon Press

S. Oka, 1973. Pressure development in a non-Newtonian flow through a tapered tube, Rheologica Acta, Vol. 12, 224-227

D. Quere, 1999. Fluid Coating on a Fiber, Annual Rev. Fluid Mechanics, vol. 31, 347-384

W. G. Sawyer, J. A. Tichy 1998. Non-Newtonian Lubrication With the Second-Order Fluid, Transactions of ASME Journal of Tribology, Vol. 120, 622-628

J. Sestak, F. Rieger 1969. Laminar heat transfer to steady Couette flow between parallel plates, International Journal of Heat and Mass Transfer Vol. 12, 71-80

R. A. Shah, S. Islam, A. M. Siddiqui, T. Haroon, 2013. Exact Solutions of a Power Law Fluid Model in Post treatment Analysis of Wire Coating with Linearly Varying Boundary Temperature, Applied Mathematics, Vol. 4, 330-337

D. Sheeja, B. S. Prabhu, 1992. Thermodynamic lubrication of non-Newtonian journal bearings: theory and experiments, J. Phys. D: Appl. Phys., Vol. 25, 1706-1712

Z. Tadmor, R. B. Bird, 1974. Rheological Analysis of Stabilizing Forces in Wire-Coating Dies, Polymer Engineering and Science, Vol. 14, No. 2, 124-136

B. Tavakol, D. P. Holmes, G. Froehlicher, H. A. Stone, 2014. Extended Lubrication Theory: Estimation of Fluid Flow in Channels with Variable Geometry, arXiv: 1403.2343v1 [physics.flu-dyn]

C. Tien, 1961. The extension of Couette flow solution to non-Newtonian fluids, Canadian Journal of Chemical Engineering 39, 45-46

N. Triantfillopulos, 1988. Measurement of Fluid Rheology and Interpretation of Rheograms, 2nd edition

N. J. Wagner, J. F. Brady, 2009. Shear thickening in colloidal dispersions, Physics today

J. R. Van Wazer, J. W. Lyons, K. Y. Kim, R. E. Colwell, 1963. Viscosity and Flow measurements, Interscience, New York

Z. W. Wicks, F. N. Jones, S. P. Pappas, D. A. Wicks, 2007. Organic Coatings Science and Technology, 3rd edition, Wiley and Sons, New Jersey

L. Yang, G. A. Chukwu, 1995. A Simplified Couette-Flow Solution of Non-Newtonian Power-Law Fluids in Eccentric Annuli, Can. J. Chem. Eng, Vol. 73, 241-247

H. Yong, R. Balendra, 2009. CFD Analysis on the Lubrication Behaviors of Journal Bearings with Dimples, Proceedings of the 2009 IEEE International Conference on Mechatronics and Automation

R. Zhang, X. K. Li, 2005. Non-Newtonian effects on lubricant thin film flows, Journal of Engineering Mathematics, Vol. 51, 1-13